THE UNIVERSITY OF HULL

Modelling of Semiconductor Nanostructures:
Electronic Properties and Simulated Optical Spectra

being a Thesis submitted for the Degree of

Doctor of Philosophy

in the University of Hull

by

Boon Hon Hong, MEng (Hull)

July 2011

To my parents, my wife, my brothers and the rest of my family

Acknowledgement

First of all, I would like to thank my supervisor, Dr Igor Itskevich, for providing directions and assistance through the course of my studies. His understanding and encouragements have given me strength to embark on this research. As for my second supervisor, Professor Stephanie Haywood, her advice and support in many aspects are also appreciated. Also, I would like to thank Dr Sergey Rybchenko for guiding me in the development of the model. To former group members, Dr Rita Gupta, Dr Khue Tian Lai and Dr Gik Hong Yeap, your various support and encouragements especially in the early stage of the course are not to be forgotten.

Next, I would like to thank the National Nanotechnology Laboratory for their kindness in providing equipment for helium temperature measurements, in particular Dr Romuald Intartaglia for his assistance in the experimental setup. Also, I would like to take this opportunity to thank Dr Achim Trampert and Dr Luna Esperanza for many useful discussions in the study of the InAs/GaSb interface. I would like to thank Professor Eric Tournié, Dr Chee Hing Tan, Mr Peter Vines and Dr Maxime Hugues for providing various samples and additional experimental data.

Last but not the least, I would like to dedicate this work to my family, especially my dear wife, for being tolerant and supportive all the time.

This study was made possible by the financial assistance of the Overseas Research Studentship Award Scheme.

Abstract

III-V semiconductor nanostructures are widely used in optoelectronic devices (e.g. lasers and detectors) in the visible (0.4-0.8 µm), near-infrared (0.8-3 µm), mid-infrared (3-5 µm) and far-infrared (> 8 µm) wavelength ranges, with great potential for high performance and high temperature operation. As well as simple designs, complex structures incorporating low dimensional components (e.g. quantum wells and quantum dots) are not unusual. Often, the optical and electronic characteristics of these structures are altered significantly as compared to bulk material. As a prerequisite to design for different applications, the study of their electronic and optical properties is essential.

With the increasing computational power of modern personal computers, computational modelling becomes viable and more efficient. Indeed, it has become routine to follow (or to precede) experimental studies with computational modelling of good interpretive and predictive power. Combined with experimental studies, this is a powerful tool to provide insight into new devices.

This research work is primarily based on calculations of the electronic band structure of various semiconductor nanostructures, followed by modelling of optical transitions and optical spectra. All numerical calculations use a cost effective computational method.

The applicability of the model to ultra-thin structures of short period InAs/GaSb superlattices is investigated. The work is then extended to study complex quantum-dot-in-well structures. Finally, the attempt to extract the structural parameters of quantum dots by a combination of modelling and optical spectroscopy is presented.

Contents

Introduction

In the late 1960s, the advance of crystal growth techniques, such as molecular beam epitaxial (MBE) [1,2] and metal-organic chemical-vapour deposition (MOCVD) [3,4], made it possible to fabricate high quality heterostructures with ultrathin layers. This has allowed the realisation of low dimensional semiconductor structures such as two-dimensional (2D) quantum wells (QWs), one-dimensional (1D) quantum wires (QWRs) and zero-dimensional (0D) quantum dots (QDs). This allows the study of quantum size effect arising from the confinement of charge carriers on the order of the de Broglie wavelength (typically a few tens of nanometres). [5] The use of low dimensional structures has significantly improved the performance of optoelectronic devices (such as giving lower threshold currents in lasers, lower detector dark currents, and higher operating temperatures). [6,7] Since then, III-V semiconductor nanostructures have attracted a great deal of attention in the development of optoelectronics, and become the subject of research by most of the semiconductor physics community. [7] Semiconductor lasers and detectors have many important applications in a variety of fields, including military, environmental protection, telecommunications, molecular spectroscopy, biomedical surgery and research. [7,8,9]

As a prerequisite to the design of these optoelectronic devices, the electronic properties of the quantum heterostructures that form the active regions have to be studied. This can be achieved by computational modelling. The primary aim of modelling is provide general explanations of the optical properties of a particular structure. As a complement to experimental results, it is used to predict the behaviour of electrons and to gain insight into properties of new structures. Hence, computational modelling is very useful in system design and optimisation.

With the rapid development of modern computers, the higher computational power allows more sophisticated modelling to be performed in a considerably shorter time. Furthermore, many of the numerical calculations can be done even using a mainstream personal computer, without the need of supercomputer or computer clusters. These make the studies by modelling approach feasible and cost efficient, and so often take place prior to or simultaneously with experimental studies.

In this work, optical and electronic properties of selected semiconductor structures are investigated by means of modelling and optical spectroscopy. In general, there are two approaches to modelling the electronic band structure, namely by the first principle calculations [10,11] and empirical methods [12,13,14]. First principle (i.e. *ab initio*) calculations start from the levels of established laws of physics and do not use empirical and/or fitting parameters. Some of the most commonly used *ab initio* calculations in physics are the density functional theory and the quantum Monte Carlo. [10,11] They have high accuracy and predictive ability, however at the expense of huge computational power and resources. Hence they limit the size of the system that can be studied as they require powerful supercomputers. For these reasons, the empirical methods are more often employed to study the electronic band structures of more realistic sized semiconductor heterostructures on a routine basis.

Three empirical models primarily used are the pseudopotential model, the tight-binding model, and the $\boldsymbol{k}\cdot\boldsymbol{p}$ method. [12,13,14] In general, the first two methods include a description of atomistic details, based on different assumptions and hence differ by the level of atomistic description. On the other hand, the $\boldsymbol{k}\cdot\boldsymbol{p}$ method is a continuum model which treats heterostructures as a confined bulk system. Among the empirical methods, the $\boldsymbol{k}\cdot\boldsymbol{p}$ method is a good choice for the study of large complicated systems due to its high computational efficiency and good accuracy, despite of the lack of atomistic details. This method is used for all the studies carried out throughout the research.

Due to the different lattice constants of materials used in the heterostructures in this work, taking into account the resulting strain is crucial to determining the optoelectronic properties. Hence, the impact of strain on the band structure is hence elucidated first. In line with the continuum approach to band structure calculation, the strain distribution is also computed based on a continuum elasticity model. In addition, the shear-strain induced piezoelectric potential is also presented due to its qualitative effect on the wave functions in the QDs. In order to determine the electronic band structure, both the computationally efficient one-band model and the more realistic multi-band models are employed. The optical transitions are then obtained. Coulomb interaction is taken into account for interband transitions. Optical spectra are simulated by superimposing broadening on the calculated transitions.

All numerical calculations are performed using the Finite Element Method (FEM). This is a good choice for continuum models because both assume continuity of material distribution and describe the structure's behaviour by continuous functions. The commercial FEM package COMSOL Multiphysics is employed for this task, mainly due to its advantage of being able to couple multiple physical problems into a single model.

As for experimental studies, non-destructive optical spectroscopy (mostly photoluminescence (PL)) is used for comparison with calculations. In particular, Fourier Transform Infrared (FTIR) spectroscopy is employed. The destructive structural characterisation method, transmission electron spectroscopy (TEM), is also used to study samples. The structural parameters thus obtained are either used as input for modelling or for reference purposes only.

The beginning of this research coincided with the participation of the Optoelectronics Group (Department of Engineering, University of Hull) in a European Commission funded project (under the FP6 work programme) called Antimonide Quantum-Dots for Mid-Infrared Nanophotonic Devices (also known as DOMINO), which was half way through its progress. This project involved collaboration with another five institutions; they are Université Montpellier 2 (France), Paul-Drude-Institute (Germany), National Nanotechnology Laboratory (Italy), Ioffe Physico-Technical Institute (Russia), and Alcatel-Thales III-V Lab (France). The main objective of the project was to demonstrate the feasibility of antimonide (Sb)-based nano-photonic lasers operating continuous wave at room temperature in the 3-5 µm wavelength range. Sb-based heterostructures, grown on GaSb or InAs substrates, offer a number of unique possibilities among III-V compounds in terms of band structure engineering. In particular, it is the only III-V material system exhibiting interband transitions in the mid-IR.

As the project developed, both Sb-based quantum dot and GaSb/InAs short-period superlattices (SPSLs) were used as active zones. These SPSLs provide a very versatile system that can cover a wide wavelength range from mid-IR to far-IR due to its type-II band alignment. Most commonly, the modelling for such semiconductor heterostructures is based on the $\boldsymbol{k} \cdot \boldsymbol{p}$ method. However, this method had so far failed to predict correctly the band structure of InAs/GaSb SPSLs. [15] Instead, it had systematically overestimated the energy gap between the electron and heavy-hole minibands which led to the suggestion that the $\boldsymbol{k} \cdot \boldsymbol{p}$ method is inadequate for these heterostructures. This became the subject of interest and an investigation into this controversy was carried out.

Our results show that the physical origin of the discrepancy between modelling and experimental results may be the lack of a realistic model for the structure of the interface, i.e. the *graded* and *asymmetric* InAs/GaSb interface profile has not previously been taken into account. Band-structure modelling was performed using a realistic interface profile based on experimental observations. The calculations show good agreement with experimental data available, both from our own measurements and from the published literature.

The study of these thin-layered 2D structures laid the foundation for the study of heterostructures of lower dimensions such as quantum dots in 2D quantum wells. Recently, much effort has been committed to the development of intraband-based quantum dot infrared photodetectors owing to their potential for normal-incidence absorption and low dark current, which are superior to the bulk- and quantum-well-based predecessors. For this purpose, the quantum-dot-in-well (DWELL) structures offer additional advantages, such as better wavelength tunability and improved carrier collection. This system presents a challenge for modelling the electronic band structure, as it requires solution for a complex system with both discrete levels from the 0D QDs and the continuum energy spectrum from the 2D QWs. The Green's function method, mostly used for such problems, has high computational cost. [16,17]

Here, with aim for low computational cost, the electronic band structure of a DWELL structures is calculated within the effective mass approximation. By superimposing Gaussian broadening on the calculated transitions, the intraband absorption spectra are simulated. The effects of both QD shapes and composition on the optical spectra are investigated. The outcome of this work has provided explanations to the origins of complex spectra.

This was a collaborative work with the Optoelectronics group led by Dr. Chee Hing Tan from the University of Sheffield, by whom most of the experimental data were made available.

The modelling of optical spectra of quantum dots is typically initiated by using structural parameters (such as shape, size and composition) obtained from destructive structural characterisation (e.g. TEM) as inputs. This is in general an established routine for most computational studies of semiconductor heterostructures. The question asked here is whether this can work the other way round, i.e. can optical spectra be used, in combination with modelling, to extract the structural parameters of a QD. Although the idea is not new [18], it is not easy since there are plenty of variables for self-assembled quantum dots. The main ones are shape, height, lateral size and composition. The number of parameters leads to cumbersome and time consuming repetitive calculations which make it impractical.

For this purpose, it is very advantageous to have a system where at least one of the parameters is controllable. Typically, the structural parameters of quantum dots are controlled by growth conditions, such as temperature, growth rate, growth time etc. Recently, a new technique has been developed in an attempt to control in-situ the height of InAs/GaAs QDs known as In-flush technique. [19] After the formation of QDs, a layer of GaAs is deposited at low temperature, partially capping the QD. The growth is then interrupted with an annealing step at higher temperature to re-evaporate the top of QDs. Finally, the growth is resumed to cap the quantum dots with GaAs. In this case, the height of QDs can be determined. By assuming the typical shape of a truncated cone, the major parameters can then be further reduced to two, i.e. lateral size and composition.

By comparison to measurements from PL only, a number of empirical relationships between structural features and parameters such as absolute peak position, separation between peaks and temperature-dependent shift are established. Then, these empirical relationships are put together on a so called “phase diagram”, whose axes represent the structural parameters in question. The overlapping region of the curves gives the estimate for both structural parameters. TEM images are used to validate this approach and the results are promising. Our cost-efficient modelling approach has made this a fast and convenient way to obtain important structural parameters of QDs without resorting to time consuming structural characterisation techniques.

This study of structural parameters of In-flush grown QDs was a collaborative work with Dr Maxime Hugues (currently at CRHEA-CNRS, France), who was responsible for sample growth and characterisations.

The thesis is structured as follows. In Chapter 1, a brief review of semiconductor heterostructures is presented, with the focus on QDs. Also, a short introduction to empirical band structure calculations and modelling of strain distributions are given. In Chapter 2, detailed modelling approaches based on the $\boldsymbol{k}\cdot\boldsymbol{p}$ method are presented. Chapter 3 describes the experimental setup used for the FTIR spectroscopy. In Chapter 4, our approach to the long-standing controversy of modelling of the electronic spectra of InAs/GaSb short-period superlattices (SPSLs) by means of the $\boldsymbol{k}\cdot\boldsymbol{p}$ method is presented. The investigation of a quantum dot-in-well system using a 3D model is presented in Chapter 5. Finally, the determination of structural parameters of QDs grown by the In-flush technique from optical spectroscopy and modelling is presented in Chapter 6. At the end of the thesis, a summary of key results and future work directions are briefly discussed.

Chapter 1

Literature Review

1.1 Semiconductor Heterostructures

This chapter begins with an introduction to semiconductor physics. This includes the general features of the energy band structure for the III-V system studied and types of heterojunction when different materials are put together. From these, the evolution of heterostructures with different dimensionality is addressed. This topic is extended with more details to the zero-dimensional quantum dot, which is the most important heterostructure studied in this work. In addition, a brief review of the empirical methods for band structure calculations is presented, with justification for the method chosen for this work. The strain field calculation is also briefly explained.

1.1.1 Energy Band Structure

An energy band structure essentially visualises the behaviour of electrons of a particular system. From this, the optical and electronic properties of a device can be determined. Therefore, band structure calculation plays a very important part in the study of semiconductor heterostructures.

When isolated atoms are brought close to each other to form a solid, interaction between neighbouring atoms will occur. The attraction and repulsion forces between atoms will come to a balance at a proper inter-atomic spacing for the crystal. In this process, the change in the electron energy level configuration leads to formation of continuous bands of energies, which include the *conduction band* and *valence band*. At absolute zero temperature, the valence band is the highest energy level that is fully occupied by electrons, whereas the conduction band is empty. The separation between these bands is a region called the band gap, E_g. It designates the energies that cannot be possessed by electrons, thus also known as the forbidden gap. This is the most important parameter in semiconductor physics. In particular, it differentiates semiconductors from metals and insulators.

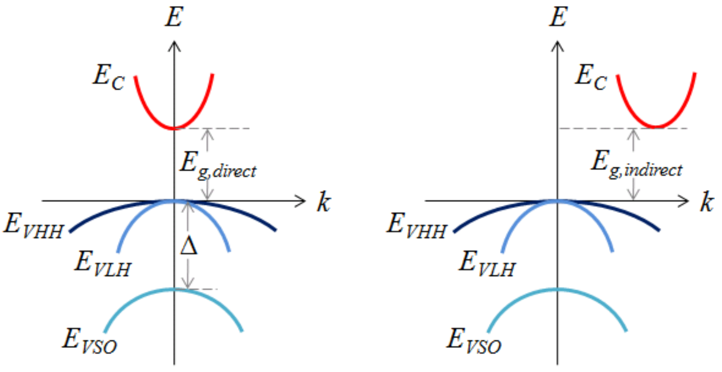

(a) Direct

(b) Indirect

Figure 1. *Direct and indirect semiconductors.*

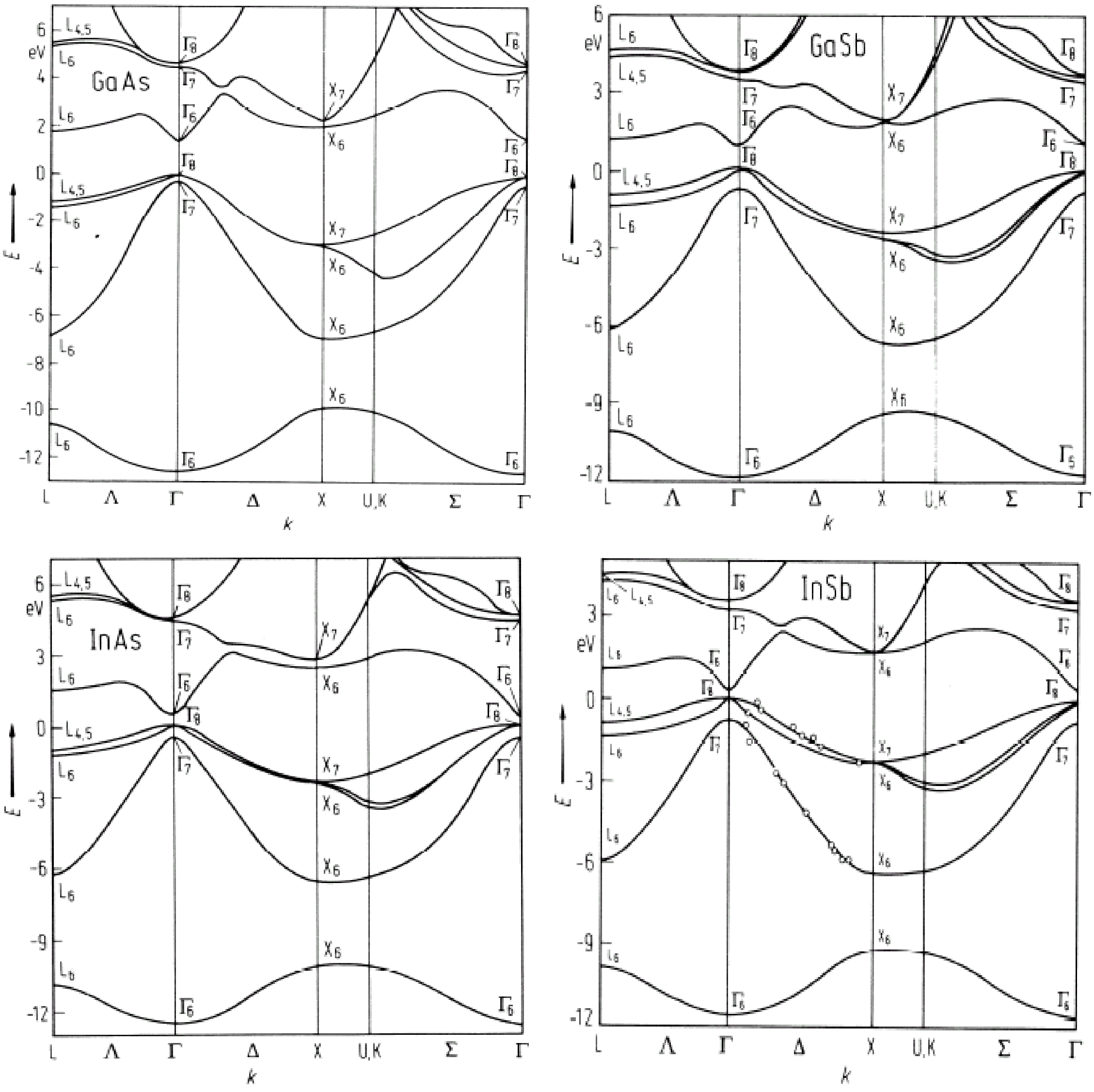

Figure 2. *Band structures of binary III-V compounds: GaAs, GaSb, InAs, and InSb. [20]*

Every solid has its own characteristic energy band structure. In typical calculation of band gaps, an electron is assumed to travel through a perfectly periodic lattice. However, the lattice spacing is different in different directions of the crystal lattice. Therefore, the minimum of the conduction band and the maximum of the valence band may not be in the same plane of the lattice in which the electron travels. This can be shown by plotting the energy-momentum (E,k) diagram as shown in Figure 1. [5]

Direct band gap semiconductors (e.g. GaAs) have a maximum in the valence band and a minimum in the conduction band for the same wave vector at the Γ band, i.e. the centre of the Brillouin zone. An electron can hence fall from the conduction band to an empty state in the valence band, giving off a photon with the energy difference E_g. For an indirect semiconductor, it must undergo a change in momentum and energy, generally giving up energy as heat to the lattice rather than emitting a photon. This is important for the selection of materials for semiconductor device applications. For light emitting optoelectronic devices such as LEDs and lasers, direct semiconductor materials are generally essential.

For the purpose of this project, only the GaAs, InAs, GaSb, and InSb compounds are discussed. The band structures of these direct band gap compounds are shown in Figure 2, plotted in the order of high symmetry lines in k-space ($\mathrm{L}-\Gamma-\mathrm{X}-\mathrm{K}-\Gamma$). The maximum of the valence bands is used as reference. The mixed crystals made of binary III-V compounds, including ternary compounds of (Al, Ga)As and (Ga, In)As, as well as quaternary compounds of (Ga, In)(As, Sb), have also semiconducting properties.

1.1.2 Heterojunctions

Depending on the alignment of the conduction and valence bands of the two materials, the charge carrier can be confined in different ways, which in turn changes the electronic band structure. [13] In general, there are two types of semiconductor hetero-interface structure in the III-V system, as visualised in Figure 3. The first one is the most common one, known as type I structure. In this configuration, both conduction and valence bands of the narrow band gap material are aligned within the band gap of the other material. In other words, both the electrons and holes are spatially confined within the narrow band gap material. Some of the III-V systems with this band alignment are InAs/GaAs and InSb/GaSb.

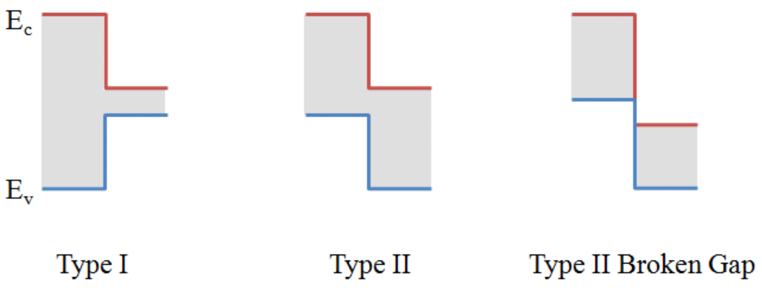

Figure 3. *Type I and type II structure configurations.*

For type II configuration, both conduction and valence bands of one material are below that of the other, respectively. In this case, the electrons and holes are confined spatially in two separate materials. This structure is exemplified by the GaSb/GaAs lattice, where the electrons are confined within GaAs while holes are trapped in the GaSb. There is an extreme case for type II alignment, where the conduction band of the small band gap material is below the valence band of the wide band gap material. This band alignment configuration is known as type II misaligned or broken gap. A typical system of this configuration is InAs/GaSb. Due to the smaller wave function overlap between the electrons and holes, the optical transition strength for the type II system is usually weaker than that of a type I system.

1.1.3 From 3D to 0D

By utilising multiple heterojunctions of different semiconductor materials, the motion of electrons can be restricted spatially to a distance of the order of the de Broglie wavelength. This results in quantisation of the energy levels, which changes the energy spectrum from continuous to discrete. This phenomenon is known as quantum confinement. [7,12]

In the simplest case of a two-dimensional (2D) QW, formed by a thin layer of narrow band gap material sandwiched between layers of wide band gap materials, the electrons are confined within the potential well in the growth direction. Figure 4 shows a typical energy band profile of a QW. As a consequence of the quantum confinement effect, the electron spectrum of a QW consists of a series of subbands with step-like density of states. These properties are much different from the macroscopic bulk materials. The position of the bottom of each of these energy subbands is determined by the conditions of the confinement, such as the width of the potential well (i.e. layer thickness) and the height of the potential barrier (i.e. material dependent).

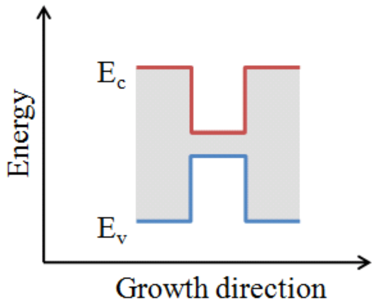

Figure 4. *Schematic of energy band profile of a typical QW structure. Red and blue bold lines represent the conduction band (E_c) and valence band (E_v), respectively.*

In order to improve the overall efficiency in the optical devices, multiple quantum well structures separated by barriers thick enough to make them impenetrable for electrons are often used. Due to similar structure (i.e. well width and barrier height), the electronic properties of individual QWs are identical, and from the point of view of the electronic properties, each of these wells is isolated. As the barrier gets thinner, carrier tunnelling from one well to another becomes possible; in other words, the wave functions of individual wells overlap and interact with each other. In this case, the discrete energy levels of isolated well broaden to form minibands. This structure is known as a superlattice (SL). [13,21,22]

In a similar manner, by introducing potential barriers to restrict the motion of electrons in more dimensions, one will get 1D quantum wires, and finally end up with the ultimate quantum confined structures – 0D quantum dots, with charge carrier confinement in all three dimensions. Similar to QWs, the energy levels can be tuned by altering the structural parameters (i.e. QD composition, size and shape) and potential barrier height (i.e. matrix composition). Due to the small size of QDs, their structural parameters have a more significant effect than their material composition; the resulting ability to tune the electronic properties with size is advantageous.

Due to the quantisation of energy levels from continuous to discrete in one or more directions, the density of states for low dimensional systems are very much different from the bulk, i.e. less continuous. Figure 5 shows the evolution of density of states as the dimensionality of a system is reduced from 3D bulk to 0D quantum dot.

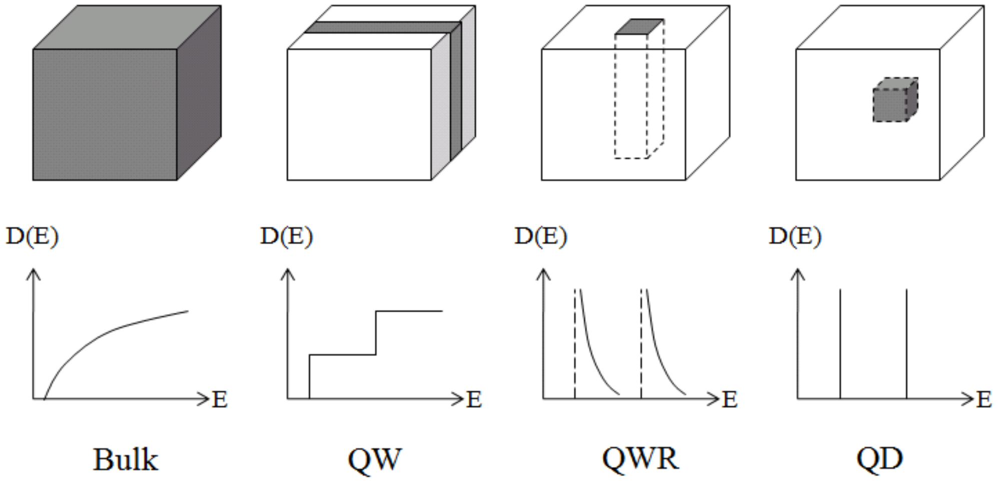

Figure 5. *Structure and density of states of bulk and low dimensional systems. [12]*

1.2 Quantum Dots

Quantum dots are zero-dimensional semiconductor nanostructures that confine electrons (and holes) in three dimensions. Due to their similarity of possessing discrete energy levels just like an atom, QDs are also termed as "artificial atoms". Depending on the epitaxial method and growth conditions, QDs have different sizes and shapes. Typical shapes found for self-assembled quantum dots are pyramidal (full or truncated), truncated cone, and lens shapes, whereas their size can range from several nanometres to tens of nanometres. [6,23,24,25,26]

1.2.1 Quantum Dot Based Optoelectronic Devices

The advantages of this zero-dimensional system as the active medium in optoelectronic devices have been predicted and recognised in the 80's. [27,28] However, the real development of its use in optoelectronic devices was only begun since 1993 when the self-assembled technique was mature enough to produce a narrow distribution of QD sizes [29,30,31].

Due to the size quantisation in all directions, the energy separation between the lower energy levels is typically greater than kT. In combination with the delta-like density of states, QDs have superior properties and advantages as compared to QWs and QWRs. For laser structures, it has been shown the characteristic low threshold current density, high temperature stability of the threshold current, and high differential gain. [32,33,34] Since the first demonstration of lasing in self-assembled quantum dots in 1994 [35], these devices have been subjected to intense study. It has been found that QDs can improve the properties of high performance optoelectronic devices as compared to those achieved with quantum wells. [6] Indeed, QD-based lasers have been realised to operate at room temperature with ultralow threshold current densities. [34]

On the other hand, QD-based photodetectors have also attracted a lot of interest due to their sensitivity to normal incidence radiation arising from the three dimensional carrier confinement. This unique characteristic makes it stand out from the technologically more matured QW-based photodetectors. On top of that, they have been shown to have lower dark current and higher photoelectric gain. [36,37] The QDIPs have been demonstrated to operate at temperatures above 250 K. [38] Also, the first two-colour QDIP camera has been demonstrated recently. [39]

There are many applications for QD-based devices including new generation of highly efficient solar cells, tunable infrared-ultraviolet lasers and LEDs, display luminophores, optical electro-modulation, switches, memory storage, and efficient sensors for explosives and toxic materials. Apart from applications in optoelectronics, QDs have also found applications in the field of Quantum Information Processing, including spin-transistors, nano-size magnets, quantum computing, and electron spin-based memories. [40]

1.2.2 Fabrication Techniques

As mentioned earlier in this chapter, advanced crystal growth techniques such as MBE and MOCVD have made it possible to precisely fabricate 2D layered semiconductors with atomic scale precision, including QWs and SLs. The further reduction of the semiconductor dimensionality in 1D QWRs and 0D QDs, however, was not straightforward. [41] Originally, the fabrication of QWRs [42,43] and QDs [44,45] was widely based on the lateral patterning of 2D heterostructures by a combination of lithography techniques and chemical etching. In addition to low density, the subsequent processing of lithography often produces contamination, formation of defects on the interfaces, and non-uniformity of size. [46]

A more promising approach is the direct synthesis of nanostructures during the growth process itself utilising self-organisation phenomena on the crystal surface. In fact, this QD fabrication technique was considered as a huge breakthrough in the field of optoelectronics. [32] This self-assembly technique is attractive mainly due to the resulting of high density and high quality defect-free structures. The fabrication of self-assembled quantum dots (SAQDs) will be emphasised here due to the interest in QDs and their internal strain distribution that results from the growth procedure.

For lattice-matched systems, the growth is determined solely by the relation between the substrate surface energy (γ_1), the epitaxial layer surface energy (γ_2), and the interface energy (γ_{12}). If ($\gamma_2+\gamma_{12}$)<γ_1, the depositing material wets the substrate by a 2D growth mode, known as Frank-van der Merwe (FvdM) growth mode. By changing ($\gamma_2+\gamma_{12}$) may result in transition from the 2D FvdM growth mode to a 3D growth mode known as Volmer-Weber (VW). For a strained lattice-mismatched system, the initial growth may occur layer by layer, i.e. 2D growth, to form the wetting layer. As it grows thicker, the elastic strain energy increases. At some point, the material organises itself and leads to the formation of three-dimensional strained islands, in which the strain is relaxed and correspondingly the elastic energy is reduced. This is known as Stranski-Krastanow (SK) growth mode. Since the strain relaxation is elastic, no defects are introduced in the quantum dot formation process. The islands are then covered with an epitaxial layer of substrate material to form capped quantum dots. [6,7] The three different growth modes are illustrated in Figure 6.

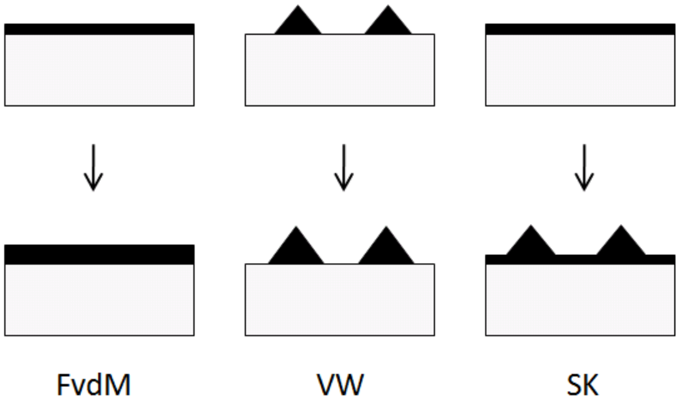

Figure 6. *Schematic of different growth modes. FvdM and VW modes are for lattice-matched systems, while the SK mode utilises strain to form QDs in lattice-mismatched system. [6]*

Generally, the SK grown self-assembled quantum dots are most popular due to their small size and high density. [47] They have great potential in optoelectronic device applications mainly due to the absence of internal defects, which leads to possibility of high optical efficiency. For device applications, self-assembled quantum dots are often grown in stacks to improve the efficiency. The growth of vertically stacked quantum dots is determined by the barrier thickness between two layers of quantum dots. For barrier thickness less than approximately 20 nm, the quantum dots of successive layers will tend to align due to the strain energy in the dot layer. [48] Hence, a stack of vertically aligned quantum dots are formed in the growth direction.

1.3 Modelling of Semiconductor Heterostructures

Apart from some simple problems such as quantum wells, using analytical modelling it is mathematically difficult when dealing with arbitrary shapes, either compositionally (even in the case of quantum wells) or geometrically, in lower dimensional structures. Often, approximations are inadequate to describe accurately the real structures of complex designs. Therefore, numerical calculations are necessary to cope with the increasing complexity of some structures. With the advance of modern computers, numerical modelling has become more practical and cost efficient. Not only can this provide better understanding of the underlying principles of the device behaviour, it has also proved to be efficient in the process of design and optimisation. The selection of the modelling method involves trade-off between accuracy and computational cost. Depending on the size of the nanostructures, one particular method suits better than others.

1.3.1 Electronic Band Structure

All band structure computation techniques involve approximations which tend to emphasize some aspects of the electronic properties in semiconductors while simultaneously simplifying the others. As mentioned earlier, the first principle or *ab initio* calculations involve very few assumptions and often no adjustable parameters. They have been successfully applied to calculate many properties of solids. [13] However, it comes with a huge expense in computational cost and hence is limited by the size of the structure that can be modelled. To reduce the cost, some properties are simplified and expressed in terms of parameters, which are determined by fitting the experimental data. These types of calculations involving experimentally fitted parameters are known as empirical models.

In this section, three empirical models [13,14,21] primarily used to study semiconductor nanostructures are briefly introduced: the pseudopotential method [15,49,50,51], the tight-binding method [52,53], and the $\boldsymbol{k} \cdot \boldsymbol{p}$ method [54,55,56]. Generally, the pseudopotential method and the tight-binding method are atomistic models with different atomistic details included in the models, while the $\boldsymbol{k} \cdot \boldsymbol{p}$ method ignores any atomistic feature. In all cases, their required input parameters are usually determined by empirical fitting to a number of experiments. Nevertheless, these parameters can also be derived from first principle calculations, or sometimes a combination of atomistic calculations and empirical fitting.

Pseudopotential Method

The pseudopotential method approximates the true potential due to core and valence electrons with an effective potential (i.e. pseudopotential), such that the core states are ignored and the valence electrons are described by nodeless pseudo-wave functions. In other words, it assumes that electrons are nearly free and so their wave functions can be described by plane waves. The crystal potential is represented by a linear superposition of atomic potentials, which are modified to fit the experiments. With atomic potentials as the essential inputs, the electronic properties of the heterostructure can be determined. Due to the inclusion of atomistic details, the band structure is computed by large-scale numerical calculations using supercomputers. This method is still computationally very demanding and the size of the structure that can be modelled is still very limited. Typically, it is used to model structure in the scale of a few nanometres. [13,50]

Tight-binding Method

In contrast to the pseudopotential method, the tight-binding model was developed from a different extreme scenario by assuming that the electrons in solids are tightly bound to their nuclei as in the atoms. When the atoms are brought together to the lattice constants in solids, their wave functions will overlap. In this case, the electron wave functions can be approximated by linear combinations of the atomic wave functions. Therefore, this method is also known as linear combination of atomic orbitals (LCAO) method. [14]

Theoretically, the assumption of the tightly bound electrons limits the scope of the applicability of the tight-binding model to insulating materials and the valence bands of semiconductors. However, it has been shown that the tight-binding model can also successfully describe the electronic properties of the conduction bands of semiconductors by relaxing the range of interactions between the valence electrons. This is done by empirically adjusting the interaction matrix elements, and by expanding a basis set. Overall, the tight-binding model is computationally slightly less demanding than the pseudopotential model due to the smaller number of basis orbitals required. Typically, the system size for such modelling is about 10×10×10 nm, or 10^4 atoms. [23,57] This makes it suitable to study SAQDs embedded with a wetting layer. Nevertheless, it is still limited to smaller dots of up to 10 nm and requires parallel cluster machines. [58]

$\boldsymbol{k} \cdot \boldsymbol{p}$ Method

As opposed to the atomistic models discussed above, the $\boldsymbol{k} \cdot \boldsymbol{p}$ method is a continuum model which treats heterostructures, including quantum dots, as a confined bulk system. The $\boldsymbol{k} \cdot \boldsymbol{p}$ method is an economical band structure calculation method based on perturbation theory [13,14,59,60,61]. It uses a limited number of band states in the expansion to calculate the band structure of bulk and strained materials in the vicinity of some high symmetry points in the Brillouin zone. This renders the $\boldsymbol{k} \cdot \boldsymbol{p}$ model attractive for a realistic analysis of different semiconductor heterostructures with much larger system size in the order of tens of nanometres, while not necessarily requiring computer clusters.

There are some limitations of this method; largely due to its lack of atomistic features, it suffers some drawbacks when applied to small quantum structures. [24] These drawbacks are mostly related to the limited Bloch functions used for expanding the wave functions, and the assumption of the same Bloch functions throughout the entire structure regardless of variations of material and strain. In addition, this method is typically restricted to the centre of the Brillouin zone, where bulk band parameters are available.

Despite the limitations in very small quantum structures, it has been successfully applied to modelling a variety of different heterostructures, including quantum dots with arbitrary shape and material composition. [59] The most commonly used implementation of this method is the 8-band Hamiltonian, which takes into account intermixing effects between the lowest conduction band and the three highest valence bands, as well as the effect of the spin-orbit interaction. The spin-orbit interaction is crucial especially for narrow band gap materials such as InAs and InSb.

For the size of heterostructure considered in this research, such as capped QDs with a base size of 30 nm, the $\boldsymbol{k} \cdot \boldsymbol{p}$ method is the best candidate among the empirical methods discussed. Most importantly, the $\boldsymbol{k} \cdot \boldsymbol{p}$ method requires much less computational resources and a mainstream PC typically would be adequate for most calculations. A detailed description of the $\boldsymbol{k} \cdot \boldsymbol{p}$ method is discussed in the next chapter.

1.3.2 Strain Distribution

The difference in lattice constants between two materials is known as *lattice mismatch*. When two different semiconductor materials with small lattice mismatch grow on top of each other, the deposited material tends to adapt to the in-plane lattice constant of the bulk substrate. The change in lattice constant results in strain being induced in the deformed crystal. This deformation of the crystal in turn affects the energy levels of the electrons. In other words, the resulting strain has significant effects on the band structure as it changes the periodicity of the crystal lattice. Since the impact of strain on the confinement is often comparable to that of the band offsets at the heterojunctions, the wave functions and energies are sensitive to the underlying strain distribution. Therefore, the effect of strain needs to be included in the calculation of the band structure.

Although strain can sometimes be analysed analytically assuming homogeneous distributions, in real cases, the strain is inhomogeneous throughout the entire structure. In addition, shear strain is usually significant in quantum dot structures, or heterostructures grown on (111) substrates. [6] This can have a huge effect on band lineup and also results in a piezoelectric potential, both affecting the electronic band structure. Therefore, numerical analysis of strain is important, and more often than not, essential.

There are a number of models available for strain calculations, namely the valence force field model [62,63], the Tersoff-potential method [64,65], and the continuum elasticity model [66,67]. Apart from the continuum elasticity model, the other two are atomistic strain models. In general, the choice of the most appropriate strain model depends on the choice of the model for the electronic band structure calculations. In this work, the continuum approach of the $\boldsymbol{k} \cdot \boldsymbol{p}$ method is used. Since the full potential of an atomistic model cannot be used, the continuum elasticity model is hence the natural choice. [68] In addition, the difference as compared to the atomistic approach is minimal, and it is well suited for the size of the SAQDs considered here. [69,70]

Based on homogeneity and continuity assumptions, the material is assumed to be continuously distributed and its entire space is filled with no gaps. Subsequently, any microstructure of the material is disregarded. Then, the body can be continually sub-divided into infinitesimal elements which possess the properties of the bulk, i.e. the behaviour of the body (e.g. elastic strain) is described by continuous functions.

Chapter 2

Modelling Approaches

2.1 Introduction

This chapter begins with the modelling of the strain distribution in a heterostructure, based on the continuum-elasticity approximation. The effects of strain on the band profiles are briefly explained. Next, the calculations of the electronic band structure utilising the empirical $\boldsymbol{k} \cdot \boldsymbol{p}$ method is discussed in detail. The incorporation of the effects of strain and the shear-strain induced piezoelectricity in the calculation of the electronic band structure are discussed. The calculation of the exciton binding energy due to the Coulomb interaction is outlined. For spectra simulation, the calculation of the transition matrix elements is explained briefly. Finally, this chapter concludes with a short introduction to the Finite Element Method (FEM), which is used as a numerical tool for all the calculations. The strain field calculation is used as an example to show a typical approach of the FEM in solving 3D problems.

2.2 Strain Distribution

2.2.1 Numerical Strain Field Calculation

In this work, the strain in a pseudomorphically grown heterostructure is numerically calculated based on the continuum-elasticity approximation. The constitutive equation is given by Lagrange’s general equation of motion (without viscosity or friction), which follows the law of energy conservation, [71]

$$\frac{\partial}{\partial t}\frac{\partial(T-U)}{\partial \dot{q}}-\frac{\partial(T-U)}{\partial q}=Q \tag{1}$$

where T is the kinetic energy, U is the potential energy (i.e. strain energy), Q is a generalised force term, and q is the displacement field. Since this is a stationary problem, both the time derivative and the kinetic energy terms are omitted. Equation (1) thus becomes:

$$\frac{\partial U}{\partial q} = Q \tag{2}$$

In accordance with Hooke's law, the stress-strain relation is given by

$$\boldsymbol{\sigma} = \mathbf{Ee} \tag{3}$$

where $\boldsymbol{\sigma}$ is the stress tensors, $\mathbf{e}$ is the strain tensors and $\mathbf{E}$ is the elasticity matrix or stiffness matrix. For an anisotropic cubic system, there are only 3 elasticity moduli (c_{11}, c_{12}, c_{44}). These material parameters are readily available. [20,72,73] Explicitly, equation (3) in matrix-vector form gives

$$\begin{bmatrix} \sigma_{xx} \\ \sigma_{yy} \\ \sigma_{zz} \\ \tau_{xy} \\ \tau_{yz} \\ \tau_{xz} \end{bmatrix} = \begin{bmatrix} c_{11} & c_{12} & c_{12} & 0 & 0 & 0 \\ c_{12} & c_{11} & c_{12} & 0 & 0 & 0 \\ c_{12} & c_{12} & c_{11} & 0 & 0 & 0 \\ 0 & 0 & 0 & c_{44} & 0 & 0 \\ 0 & 0 & 0 & 0 & c_{44} & 0 \\ 0 & 0 & 0 & 0 & 0 & c_{44} \end{bmatrix} \begin{bmatrix} e_{xx} \\ e_{yy} \\ e_{zz} \\ \gamma_{xy} \\ \gamma_{yz} \\ \gamma_{xz} \end{bmatrix} \tag{4}$$

where σ_{ii} and τ_{ij} are normal and shear stress tensors, while e_{ii} and $\gamma_{ij}\ (\equiv 2e_{ij})$ are normal and shear strain tensors, respectively. The strain energy density can be derived as the inner product of stress and strain vector, in the general form of $\frac{1}{2}\boldsymbol{\sigma}\mathbf{e}$, giving

$$\begin{aligned} U = &\frac{1}{2}c_{11}\left(e_{xx}{}^2 + e_{yy}{}^2 + e_{zz}{}^2\right) + c_{12}\left(e_{xx}e_{yy} + e_{xx}e_{zz} + e_{yy}e_{zz}\right) \\ &+ 2c_{44}\left(e_{xy}{}^2 + e_{xz}{}^2 + e_{yz}{}^2\right) \end{aligned} \tag{5}$$

In strained semiconductor heterostructure, the lattice mismatch is the sole cause of induced strain throughout the system. It is therefore treated as the initial strain in the strain field calculation, given by:

$$e_0 = \frac{a_s - a_d}{a_d} \tag{6}$$

where e_0 is the initial strain or lattice mismatch, a_s is lattice constant of bulk/substrate, a_d is the lattice constant of the deposited material. The initial strain enters equation (2) as a force term described by $\mathbf{Ee_0}$, where $\mathbf{e_0} = [e_0 \quad e_0 \quad e_0 \quad 0 \quad 0 \quad 0]^{\mathrm{T}}$. In this case, the effect of thermal expansion is included by using the temperature-dependent lattice constant. Following equation (2), the displacement field can be obtained by minimising the strain energy of the entire structure. Providing that the strains are small, the infinitesimal strain tensors are given by the spatial derivative of the displacements,

$$e_{xx} = \frac{\partial u}{\partial x}, \qquad e_{yy} = \frac{\partial v}{\partial y}, \qquad e_{zz} = \frac{\partial w}{\partial z}$$
$$\gamma_{xy} = \frac{\partial u}{\partial y} + \frac{\partial v}{\partial x}, \qquad \gamma_{yz} = \frac{\partial v}{\partial z} + \frac{\partial w}{\partial y}, \qquad \gamma_{xz} = \frac{\partial u}{\partial z} + \frac{\partial w}{\partial x} \tag{7}$$

where u, v and w are displacement in x, y and z directions, respectively.

2.2.2 Strain-modified Confinement Profiles

The effect of strain on the band edges can be described based on the model solid theory and standard deformation potential theory. [74] In this work, only the Γ band is interesting, and is therefore discussed. Under uniform deformation, the direct effect of strain is the change of volume ($\delta V/V = e_{xx} + e_{yy} + e_{zz}$), known as hydrostatic strain e_h. It can be parameterised linearly to the change in band gap energy δE_g, given by

$$\delta E_g = a_g e_h \tag{8}$$

where a_g is the band gap deformation potential. Since the band gap of III-V materials increases in the presence of compressive strain (i.e. negative strain), a_g must be negative. Also, a_g is the sum of the conduction band and the valence band hydrostatic deformation potentials, i.e. $a_g = a_c + a_v$. Assuming that the conduction band shifts up and valence bands shift down, both a_c and a_v are negative values as well. These signs are chosen in accordance with the convention used in reference 72, which provides an extensive compilation of band parameters for III-V semiconductors and from which most inputs to calculations in this work are referred to.

For conduction bands at Γ, only the hydrostatic strain e_h contributes to the shift of the band edge. In the valence bands, however, the presence of shear strain introduces additional splitting and complicates the description of the strain effects in the valence bands. In the absence of strain and spin interaction, the three uppermost valence bands are degenerate. With spin-orbit interaction, the degenerate valence bands (Γ_{15}) split into a two-fold heavy-hole and light-hole valence bands (Γ_8), and a spin-orbit-split-off valence band (Γ_7). (See Figure 1a) The shear strain further breaks the symmetry and lifts the degeneracy of the Γ_8 band to form heavy-hole and light-hole valence bands. The shear-induced shift is given by [75]

$$\begin{aligned}\delta E_S = -b\left[\begin{pmatrix}-2 & 0 & 0\\ 0 & 1 & 0\\ 0 & 0 & 1\end{pmatrix}e_{xx} + \begin{pmatrix}1 & 0 & 0\\ 0 & -2 & 0\\ 0 & 0 & 1\end{pmatrix}e_{yy} + \begin{pmatrix}1 & 0 & 0\\ 0 & 1 & 0\\ 0 & 0 & -2\end{pmatrix}e_{zz}\right]\\ -\sqrt{3}d\left[\begin{pmatrix}0 & -1 & 0\\ -1 & 0 & 0\\ 0 & 0 & 0\end{pmatrix}e_{xy} + \begin{pmatrix}0 & 0 & 0\\ 0 & 0 & -1\\ 0 & -1 & 0\end{pmatrix}e_{yz} + \begin{pmatrix}0 & 0 & -1\\ 0 & 0 & 0\\ -1 & 0 & 0\end{pmatrix}e_{xz}\right]\end{aligned} \quad (9)$$

where b and d are shear deformation potentials. The strain interacts (by addition) with spin-orbit interaction, given by

$$H_{\mathrm{so}} = \frac{\Delta}{3}\begin{bmatrix} 0 & -i & 0 & 0 & 0 & 1\\ i & 0 & 0 & 0 & 0 & -i\\ 0 & 0 & 0 & -1 & i & 0\\ 0 & 0 & -1 & 0 & i & 0\\ 0 & 0 & -i & -i & 0 & 0\\ 1 & i & 0 & 0 & 0 & 0\end{bmatrix} \quad (10)$$

where $\frac{\hbar}{4m_0^2c^2}\langle X|[\nabla V_0 \times \boldsymbol{p}]_z|Y\rangle = {}^{i\Delta}/_{3}$ and Δ is spin-orbit splitting energy.

In the p-symmetry atomic orbital basis of $|X\uparrow\rangle$, $|Y\uparrow\rangle$, $|Z\uparrow\rangle$, $|X\downarrow\rangle$, $|Y\downarrow\rangle$, $|Z\downarrow\rangle$, the effect of strain is given by

$$\begin{bmatrix} a_v e_h + b_{xx} & d_{xy} - i\frac{\Delta}{3} & d_{xz} & 0 & 0 & \frac{\Delta}{3}\\ d_{xy} + i\frac{\Delta}{3} & a_v e_h + b_{yy} & d_{yz} & 0 & 0 & -i\frac{\Delta}{3}\\ d_{xz} & d_{yz} & a_v e_h + b_{zz} & -\frac{\Delta}{3} & i\frac{\Delta}{3} & 0\\ 0 & 0 & -\frac{\Delta}{3} & a_v e_h + b_{xx} & d_{xy} + i\frac{\Delta}{3} & d_{xz}\\ 0 & 0 & -i\frac{\Delta}{3} & d_{xy} - i\frac{\Delta}{3} & a_v e_h + b_{yy} & d_{yz}\\ \frac{\Delta}{3} & i\frac{\Delta}{3} & 0 & d_{xz} & d_{yz} & a_v e_h + b_{zz}\end{bmatrix} \quad (11)$$

where $b_{ii} = b\left(2e_{ii} - \left(e_{jj} + e_{kk}\right)\right)$ and $d_{ij} = \sqrt{3}de_{ij}$. By diagonalising this matrix, the final position for each valence band can be obtained.

Along the [001] direction, only the biaxial strain terms b_{ii} are non-zero. The strain-modified band profiles of the conduction band ($E_{C,S}$), heavy-hole valence band ($E_{VHH,S}$), light-hole band ($E_{VLH,S}$) and spin-orbit split-off band ($E_{VSO,S}$) are obtained as:

$$E_{C,S} = E_V + E_g + a_c e_h \quad (12)$$

$$E_{VHH,S} = E_V + a_v e_h - b e_{bi} \quad (13)$$

$$E_{VLH,S} = E_V + a_v e_h - \frac{\Delta}{2} + \frac{1}{2}b e_{bi} + \frac{1}{2}\sqrt{\Delta^2 + 2\Delta b e_{bi} + 9(b e_{bi})^2} \quad (14)$$

$$E_{VSO,S} = E_V + a_v e_h - \frac{\Delta}{2} + \frac{1}{2} b e_{bi} - \frac{1}{2}\sqrt{\Delta^2 + 2\Delta b e_{bi} + 9(b e_{bi})^2} \tag{15}$$

where the biaxial strain is given by $e_{bi} = e_{zz} - \frac{1}{2}(e_{xx} + e_{yy})$ and the unstrained valence band maximum $E_V = E_v^{av} + {}^{\Delta}/_{3}$. E_v^{av} is the weighted average over the three uppermost valence bands on an absolute energy scale and is used as a reference. Following these relationships, the qualitative change in conduction and valence bands can be predicted as shown in Figure 7. In overall, the band gap increases (decreases) under compressive (tensile) strain. The heavy-hole (light-hole) band is the highest valence band under compressive (tensile) strain.

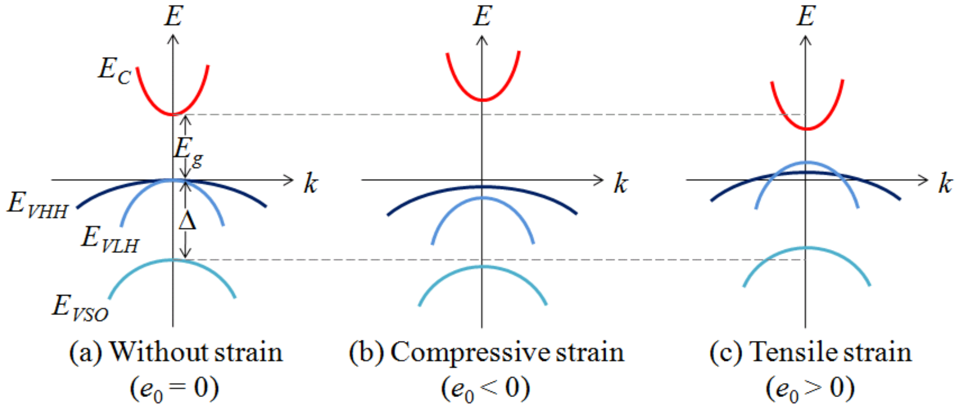

Figure 7. *Effect of strains on a typical III-V semiconductor band structures in the vicinity of the* Γ*-point.*

2.2.3 Piezoelectricity

Piezoelectricity is defined as the generation of electric polarisation by the application of stress to a crystal lacking a centre of symmetry. [68] The deformed lattice causes the formation of charge dipoles, which in turn create a potential field. The resulting piezoelectric potential will affect the overall potential profile of a structure, hence the electronic band structure. For zinc-blende structure, piezoelectricity is naturally present due to the lack of inversion symmetry. Because the polarisation is related to shear strain, the effects are expected to concentrate along the $\langle 111 \rangle$ directions of semiconductor heterostructures. [6] In particular for quantum dots, although the piezoelectric potential may not have significant effect on the energy, the quadrupole-like potential reduces the symmetry of a structural C_{4v} or $C_{\infty v}$ quantum dot to C_{2v}. [76] Hence it is necessary to include this effect in the study of QDs.

The shear strain leads to a piezoelectric polarisation $\mathrm{P}_i = \mathbf{e}_{ijk}e_{jk}$, where $\mathbf{e}_{ijk}$ is the piezoelectric tensor and e_{jk} is the strain tensor. For zinc-blende material, the only nonzero piezoelectric tensors are when $i \neq j \neq k$. Hence, the strength of resulting polarisation is described by one parameter alone, $\mathbf{e}_{123} = \mathbf{e}_{14}$, given by the expression

$$\mathbf{P} = 2\mathbf{e}_{14}(e_{yz} \quad e_{xz} \quad e_{xy})^{\mathrm{T}} \tag{16}$$

This piezoelectric tensor can be determined directly from experiments. The induced fixed piezoelectric charge, ρ_{p}, arising from the polarisation is given by

$$\rho_{\mathrm{p}} = -\nabla \cdot \mathbf{P} \tag{17}$$

The resulting piezoelectric potential, V_{p}, is then obtained by solving Poisson's equation, taking into account the material dependence of the static dielectric constant $\varepsilon_s(r)$,

$$\rho_{\mathrm{p}}(r) = \varepsilon_0 \nabla \cdot [\varepsilon_s(r) \nabla V_{\mathrm{P}}(r)] \tag{18}$$

2.3 The $\boldsymbol{k} \cdot \boldsymbol{p}$ Equation

Recall that the one-electron Schrödinger equation has the form of

$$\left(\frac{\boldsymbol{p}^2}{2m_0} + V(r)\right)\Psi(r) = \left(-\frac{\hbar^2}{2m_0}\nabla^2 + V(r)\right)\Psi(r) = E\Psi(r) \tag{19}$$

By using the Bloch theorem, the solution of the equation is $\Psi_{n\boldsymbol{k}}(r) = e^{i\boldsymbol{k}\cdot r}u_{n\boldsymbol{k}}(r)$, where n is the band index, $\boldsymbol{k}$ lies within the first Brillouin zone, and $u_{n\boldsymbol{k}}$ has the periodicity of the lattice. By substitution, it gives

$$\left(-\frac{\hbar^2}{2m_0}\nabla^2 + V(r)\right)\left(e^{i\boldsymbol{k}\cdot r}u_{n\boldsymbol{k}}(r)\right) = E_{n\boldsymbol{k}}\left(e^{i\boldsymbol{k}\cdot r}u_{n\boldsymbol{k}}(r)\right) \tag{20}$$

$$-\frac{\hbar^2}{2m_0}(-\boldsymbol{k}^2 + \nabla^2 + 2i\boldsymbol{k}\cdot\nabla)u_{n\boldsymbol{k}}(r) + V(r)u_{n\boldsymbol{k}}(r) = E_{n\boldsymbol{k}}u_{n\boldsymbol{k}}(r) \tag{21}$$

$$\left(\frac{\boldsymbol{p}^2}{2m_0} + V(r) + \frac{\hbar^2\boldsymbol{k}^2}{2m_0} + \frac{\hbar\boldsymbol{k}\cdot\boldsymbol{p}}{m_0}\right)u_{n\boldsymbol{k}}(r) = E_{n\boldsymbol{k}}u_{n\boldsymbol{k}}(r) \tag{22}$$

Apart from the original kinetic and potential terms, there are two additional terms introduced. The first one is simply an energy term and the second one consists of a $\boldsymbol{k}\cdot\boldsymbol{p}$ term. This equation is the so called $\boldsymbol{k}\cdot\boldsymbol{p}$ equation.

At the Γ point, where $\boldsymbol{k}$ = (0, 0, 0), the equation reduces to

$$\left(\frac{\boldsymbol{p}^2}{2m_0}+V\right)u_{n\boldsymbol{0}}=E_{n\boldsymbol{0}}u_{n\boldsymbol{0}} \tag{23}$$

Once the reduced equation at the Γ point is solved, the terms $(\hbar\boldsymbol{k}\cdot\boldsymbol{p})/m_0$ and $\hbar^2\boldsymbol{k}^2/(2m_0)$ are treated as perturbations using perturbation theory. This method for calculating the band dispersion is known as the $\boldsymbol{k}\cdot\boldsymbol{p}$ method. [13]

2.4 One-band Model

Due to the interaction between electrons and holes, the conduction band and valence band are coupled; the coupling strength depends on the materials used. In some cases, the coupling effect is weak. For simplicity, the conduction and valence bands can be considered as decoupled and the electronic structure of each band can be modelled individually using the simpler model of the one-band Schrödinger equation.

The general solutions for the electron states are $\Psi(r)=u(r)\phi(r)$, where u is the bulk band edge Bloch function and ϕ is an envelope function that satisfies the one-band Schrödinger equation,

$$\left[-\frac{\hbar^2}{2m^*}\nabla^2+V(r)\right]\phi(r)=E\phi(r)\ , \tag{24}$$

where m^* is the isotropic effective mass of the electron in the lowest bulk state and V is the 3D confining potential. By careful definition of m^*, the one-band approximation can be used as an efficient model with good accuracy.

Using non-degenerate perturbation theory, the correction to the energy can be expanded to second order in $\boldsymbol{k}$ are expressed in terms of unperturbed wavefunctions $u_{n\boldsymbol{0}}$ and energies $E_{n\boldsymbol{0}}$. [13,14]

$$E_{n\boldsymbol{k}}=E_{n\boldsymbol{0}}+\frac{\hbar^2\boldsymbol{k}^2}{2m_0}+\frac{\hbar^2}{m_0^2}\sum_{n\neq n}\frac{|\langle u_{n\boldsymbol{0}}|\boldsymbol{k}\cdot\boldsymbol{p}|u_{n\boldsymbol{0}}\rangle|^2}{E_{n\boldsymbol{0}}-E_{n\boldsymbol{0}}}\ . \tag{25}$$

By comparing with the conventional expression of energy $E_{n\boldsymbol{k}}$ for small values of $\boldsymbol{k}$,

$$E_{n\boldsymbol{k}}=E_{n\boldsymbol{0}}+\frac{\hbar^2\boldsymbol{k}^2}{2m^*} \tag{26}$$

the explicit form of the effective mass can be obtained:

$$\frac{1}{m^{*}}=\frac{1}{m}+\frac{2}{m^{2}\boldsymbol{k}^{2}}\sum_{n\neq n}\frac{|\langle u_{n\mathbf{0}}|\boldsymbol{k}\cdot\boldsymbol{p}|u_{n\mathbf{0}}\rangle|^{2}}{E_{n\mathbf{0}}-E_{n\mathbf{0}}}\ . \tag{27}$$

For the lowest conduction band, the effective mass coupled with light-hole and spin-orbit split-off valence bands and the others (i.e. remote bands) can be obtained as

$$\frac{1}{m_e^{*}}=\frac{1}{m_0}+\frac{2}{m_0^{2}}\left(m_0F+\frac{2m_0^{2}{P_0}^{2}}{3E_g\hbar^{2}}+\frac{m_0^{2}{P_0}^{2}}{3\left(E_g+\Delta\right)\hbar^{2}}\right) \tag{28}$$

$$\frac{m_0}{m_{\mathrm{e}}^{*}}=(1+2F)+\frac{E_p\left(E_g+2\Delta/3\right)}{E_g\left(E_g+\Delta\right)} \tag{29}$$

where the momentum matrix element between the s-like conduction band and the p-like valence bands is given by $\langle S|p_x|X\rangle=\langle S|p_y|Y\rangle=\langle S|p_z|Z\rangle=im_0P_0/\hbar$. $E_p=2m_0P_0^{2}/\hbar^{2}$ is the coupling term in unit of eV; $F=\frac{1}{m_0}\sum_r\frac{|\langle S|p_x|u_r\rangle|^{2}}{E_c-E_r}$ is the Kane parameter for remote band contributions to the conduction band, E_g is the band gap and Δ is the spin-orbit splitting energy. [72]

In this work, the single band effective mass approximation is employed when only the conduction band is of interest. In the presence of strain, the band gap E_g in (29) becomes $\left(E_g+a_ge_h\right)$ to include the change due to hydrostatic strain. Also, the strain-modified band profile as shown in equation (12) is used, with addition of shear strain-induced piezoelectric potential where applicable.

2.5 Multi-band Model

In order to obtain a more realistic and accurate band structure, a multi-band $\boldsymbol{k}\cdot\boldsymbol{p}$ model is necessary to account explicitly for the coupling between bands. In this work, an eight-band strain-dependent Hamiltonian [13,14,55,56,59] originating from the Kane model [55] is employed. It includes the lowest conduction (Γ_6), as well as heavy-hole, light-hole (Γ_8) and spin-orbit (Γ_7) valence bands.

2.5.1 Eight-band $\boldsymbol{k}\cdot\boldsymbol{p}$ Hamiltonian

In the absence of strain, the Hamiltonian, H_K, is defined by the $\boldsymbol{k}\cdot\boldsymbol{p}$ equation giving:

$$H_K=H_0+H_{\mathrm{k}}+H_{\mathrm{k\cdot p}}+H_{\mathrm{so}} \tag{30}$$

where

$$H_0 = \frac{\boldsymbol{p}^2}{2m_0} + V_0 \ , \tag{31}$$

$$H_{\mathrm{k}} = \frac{\hbar^2 \boldsymbol{k}^2}{2m_0} \ , \tag{32}$$

$$H_{\mathrm{k \cdot p}} = \frac{\hbar}{m_0} \boldsymbol{k} \cdot \boldsymbol{p} \ , \tag{33}$$

$$H_{\mathrm{so}} = \frac{\hbar}{4m_0^2 c^2} (\nabla V_0) \times \boldsymbol{p} \cdot \boldsymbol{\sigma} \ . \tag{34}$$

In addition to the terms derived earlier in equation (22), the spin-orbit interaction H_{so} term is also included, where $\boldsymbol{\sigma} = (\sigma_x, \sigma_y, \sigma_z)$ are the Pauli spin matrices given as

$$\sigma_x = \begin{bmatrix} 0 & 1 \\ 1 & 0 \end{bmatrix}, \ \sigma_y = \begin{bmatrix} 0 & -i \\ i & 0 \end{bmatrix}, \ \sigma_z = \begin{bmatrix} 1 & 0 \\ 0 & -1 \end{bmatrix} \tag{35}$$

There is also a $\boldsymbol{k}$-dependent spin-orbit interaction term, which has $\boldsymbol{k}$ instead of $\boldsymbol{p}$ as in H_{so}. However, due to the small size of $\hbar\boldsymbol{k}$ as compared to the matrix element of $\boldsymbol{p}$, it has much weaker interaction and hence is not included here.

Without Spin-Orbit Interaction

For zinc-blende semiconductors at Γ and in the absence of spin, the lowest conduction band has Γ_1 symmetry (s-symmetry wave function) and the three highest valence bands are of Γ_4 symmetry (p-symmetry wave function). Therefore, an atomic orbital Bloch basis set $|m\rangle$ is used, with $|S\rangle$ for the conduction band, and $|X\rangle$, $|Y\rangle$, $|Z\rangle$ for the valence bands. [14] Without spin-orbit interaction and spin degeneracy, the Kane Hamiltonian in the basis order $|S\rangle$, $|X\rangle$, $|Y\rangle$, $|Z\rangle$ for rows and columns is given by:

$$\begin{bmatrix} E_C + A'\boldsymbol{k}^2 & Bk_yk_z + iP_0k_x & Bk_xk_z + iP_0k_y & Bk_xk_y + iP_0k_z \\ Bk_yk_z - iP_0k_x & \begin{matrix} E_v^{av} + L'k_x^2 \\ +M(k_y^2 + k_z^2) \end{matrix} & N'k_xk_y & N'k_xk_z \\ Bk_xk_z - iP_0k_y & N'k_xk_y & \begin{matrix} E_v^{av} + L'k_y^2 \\ +M(k_x^2 + k_z^2) \end{matrix} & N'k_yk_z \\ Bk_xk_y - iP_0k_z & N'k_xk_z & N'k_yk_z & \begin{matrix} E_v^{av} + L'k_z^2 \\ +M(k_x^2 + k_y^2) \end{matrix} \end{bmatrix} \tag{36}$$

where E_C is the unstrained conduction band edge and E_v^{av} is the unstrained average valence band position in absolute energy scale as defined in the model solid theory. [74,77] The Kane parameters A', L', M, N' are constants defined by:

$$A' = \frac{\hbar^2}{2m_0}\left(\frac{1}{m_e} - \frac{E_p\left(E_g + 2\Delta/3\right)}{E_g\left(E_g + \Delta\right)}\right) \ , \tag{37}$$

$$L' = -\frac{\hbar^2}{2m_0}(1 + \gamma_1 + 4\gamma_2) \ , \tag{38}$$

$$M = -\frac{\hbar^2}{2m_0}(1 + \gamma_1 - 2\gamma_2) \ , \tag{39}$$

$$N' = -\frac{\hbar^2}{2m_0}(6\gamma_3) \ , \tag{40}$$

where γ_i's are modified Luttinger parameters defined using the ordinary Luttinger parameters, γ_i^L, (See Section 2.5.3 for more discussion)

$$\gamma_1 = \gamma_1^L - \frac{E_p}{3E_g + \Delta} \ ; \quad \gamma_2 = \gamma_2^L - \frac{1}{2}\frac{E_p}{3E_g + \Delta} \ ; \quad \gamma_3 = \gamma_3^L - \frac{1}{2}\frac{E_p}{3E_g + \Delta} \ . \tag{41}$$

B is an inversion symmetry parameter due to the lack of inversion symmetry in zinc-blende crystals. [55] Since the interaction between conduction and valence bands has already been taken into account in the linear-k terms, the quadratic-k terms which have much weaker effect are assumed negligible ($B = 0$). In part, this is also due to the lack of a reasonable estimate of their value. [24,56,59,70] In order to avoid getting negative effective mass for the conduction band which may lead to computational instability and spurious solutions, the large parenthesis in A' is modified to become unity, i.e. $A' = \frac{\hbar^2}{2m_0}$. [69] Consequently, this removes the contributions of remote bands to the conduction band and the resulting Hamiltonian becomes strictly within the lowest conduction band and the three highest valence bands. Nevertheless, this is still a good approximation since the remote bands are far away from these bands for the III-V semiconductor studied in this work, as shown in Figure 2.

$$\begin{bmatrix} E_C + \left(\frac{\hbar^2}{2m_0}\right)\boldsymbol{k}^2 & iP_0k_x & iP_0k_y & iP_0k_z \\ -iP_0k_x & \begin{matrix} E_v^{av} + L'k_x^2 \\ +M\left(k_y^2 + k_z^2\right) \end{matrix} & N'k_xk_y & N'k_xk_z \\ -iP_0k_y & N'k_xk_y & \begin{matrix} E_v^{av} + L'k_y^2 \\ +M(k_x^2 + k_z^2) \end{matrix} & N'k_yk_z \\ -iP_0k_z & N'k_xk_z & N'k_yk_z & \begin{matrix} E_v^{av} + L'k_z^2 \\ +M\left(k_x^2 + k_y^2\right) \end{matrix} \end{bmatrix} \tag{42}$$

Inclusion of Spin-Orbit Interaction

With the introduction of spin σ ($\uparrow$ for spin up and $\downarrow$ for spin down), a 8×8 Hamiltonian can be written as block-diagonal matrix of equation (42) with orbital Bloch basis in the order of $|S\uparrow\rangle$, $|X\uparrow\rangle$, $|Y\uparrow\rangle$, $|Z\uparrow\rangle$, $|S\downarrow\rangle$, $|X\downarrow\rangle$, $|Y\downarrow\rangle$, $|Z\downarrow\rangle$. The spin interaction term of the same basis $|m\sigma\rangle$ is not diagonal, given by

$$H_{\mathrm{so}}=\frac{\Delta}{3}\begin{bmatrix} 0 & 0 & 0 & 0 & 0 & 0 & 0 & 0 \\ 0 & 0 & -i & 0 & 0 & 0 & 0 & 1 \\ 0 & i & 0 & 0 & 0 & 0 & 0 & -i \\ 0 & 0 & 0 & 0 & 0 & -1 & i & 0 \\ 0 & 0 & 0 & 0 & 0 & 0 & 0 & 0 \\ 0 & 0 & 0 & -1 & 0 & 0 & i & 0 \\ 0 & 0 & 0 & -i & 0 & -i & 0 & 0 \\ 0 & 1 & i & 0 & 0 & 0 & 0 & 0 \end{bmatrix} \tag{43}$$

where $\frac{\hbar}{4m_0^2c^2}\langle X|[\nabla V_0\times\boldsymbol{p}]_z|Y\rangle = {}^{i\Delta}/_{3}$. It is however known that the H_{so} is diagonal in the angular momentum basis $|jm_j\rangle$. [14] The $|m\sigma\rangle$ basis can be transformed to angular momentum basis with a chosen direction of quantisation in [001], by $|jm_j\rangle=\sum_{m\sigma}U_{m\sigma jm_j}|m\sigma\rangle$, where the unitary transformation matrix $U_{m\sigma jm_j}$ is given by

$$U_{m\sigma jm_j}=\begin{bmatrix} 1 & 0 & 0 & 0 & 0 & 0 & 0 & 0 \\ 0 & \sqrt{1/2} & 0 & \sqrt{1/6} & 0 & 0 & 0 & -i\sqrt{1/3} \\ 0 & i\sqrt{1/2} & 0 & -i\sqrt{1/6} & 0 & 0 & 0 & -\sqrt{1/3} \\ 0 & 0 & -i\sqrt{2/3} & 0 & 0 & 0 & \sqrt{1/3} & 0 \\ 0 & 0 & 0 & 0 & 1 & 0 & 0 & 0 \\ 0 & 0 & i\sqrt{1/6} & 0 & 0 & i\sqrt{1/2} & \sqrt{1/3} & 0 \\ 0 & 0 & -\sqrt{1/6} & 0 & 0 & \sqrt{1/2} & i\sqrt{1/3} & 0 \\ 0 & 0 & 0 & \sqrt{2/3} & 0 & 0 & 0 & \sqrt{1/3} \end{bmatrix} \tag{44}$$

in which the new basis functions are in the order of $\left|\frac{1}{2}\frac{1}{2}\right\rangle_c$, $\left|\frac{1}{2}\frac{\bar{1}}{2}\right\rangle_c$, $\left|\frac{3}{2}\frac{\bar{1}}{2}\right\rangle_v$, $\left|\frac{3}{2}\frac{\bar{3}}{2}\right\rangle_v$, $\left|\frac{3}{2}\frac{3}{2}\right\rangle_v$, $\left|\frac{3}{2}\frac{1}{2}\right\rangle_v$, $\left|\frac{1}{2}\frac{1}{2}\right\rangle_v$, $\left|\frac{1}{2}\frac{\bar{1}}{2}\right\rangle_v$. The spin-orbit interaction term becomes

$$H_{\mathrm{so}}=\frac{\Delta}{3}\begin{bmatrix} 0 & 0 & 0 & 0 & 0 & 0 & 0 & 0 \\ 0 & 0 & 0 & 0 & 0 & 0 & 0 & 0 \\ 0 & 0 & 1 & 0 & 0 & 0 & 0 & 0 \\ 0 & 0 & 0 & 1 & 0 & 0 & 0 & 0 \\ 0 & 0 & 0 & 0 & 1 & 0 & 0 & 0 \\ 0 & 0 & 0 & 0 & 0 & 1 & 0 & 0 \\ 0 & 0 & 0 & 0 & 0 & 0 & -2 & 0 \\ 0 & 0 & 0 & 0 & 0 & 0 & 0 & -2 \end{bmatrix} \tag{45}$$

With inclusion of spin, the $(\Gamma_1 \rightarrow \Gamma_6)$ conduction band becomes 2-degenerate bands, and the $(\Gamma_4 \rightarrow \Gamma_{15})$ valence bands split into a 4-degenerate Γ_8 valence bands $(j = {}^{3}\!/_{2})$ and a 2-degenerate Γ_7 spin-orbit-split-off valence bands $(j = {}^{1}\!/_{2})$ separated by spin-orbit splitting energy Δ. Explicitly, the basis $\left|\frac{3}{2}\frac{\bar{3}}{2}\right\rangle_v$ and $\left|\frac{3}{2}\frac{3}{2}\right\rangle_v$ are heavy-hole valence bands, while that of $\left|\frac{3}{2}\frac{\bar{1}}{2}\right\rangle_v$ and $\left|\frac{3}{2}\frac{1}{2}\right\rangle_v$ correspond to light-hole valence bands.

By applying the same unitary transformation to the eight-band Hamiltonian with the $|m\sigma\rangle$ basis, the spin-orbit interaction matrix is then included by addition to give the final form of the unstrained eight-band H_K Hamiltonian. [59] The main diagonal terms describe the kinetic energy of particle and potential profile of corresponding bands, while the sub-diagonal terms describes the interaction and coupling between the bands.

$$H_K = \begin{pmatrix} A & 0 & V^* & 0 & \sqrt{3}V & -\sqrt{2}U & -U & \sqrt{2}V^* \\ 0 & A & -\sqrt{2}U & -\sqrt{3}V^* & 0 & -V & \sqrt{2}V & U \\ V & -\sqrt{2}U & -P+Q & -S^* & R & 0 & \sqrt{\frac{3}{2}}S & -\sqrt{2}Q \\ 0 & -\sqrt{3}V & -S & -P-Q & 0 & R & -\sqrt{2}R & \frac{1}{\sqrt{2}}S \\ \sqrt{3}V^* & 0 & R^* & 0 & -P-Q & S^* & \frac{1}{\sqrt{2}}S^* & \sqrt{2}R^* \\ -\sqrt{2}U & -V^* & 0 & R^* & S & -P+Q & \sqrt{2}Q & \sqrt{\frac{3}{2}}S^* \\ -U & \sqrt{2}V^* & \sqrt{\frac{3}{2}}S^* & -\sqrt{2}R^* & \frac{1}{\sqrt{2}}S & \sqrt{2}Q & -P-\mathit{\Delta} & 0 \\ \sqrt{2}V & U & -\sqrt{2}Q & \frac{1}{\sqrt{2}}S^* & \sqrt{2}R & \sqrt{\frac{3}{2}}S & 0 & -P-\mathit{\Delta} \end{pmatrix} \tag{46}$$

where

$$A = E_C + \frac{\hbar^2}{2m_0}\left(k_x^2 + k_y^2 + k_z^2\right) \tag{47}$$

$$P = -E_V + \gamma_1 \frac{\hbar^2}{2m_0}\left(k_x^2 + k_y^2 + k_z^2\right) \tag{48}$$

$$Q = \gamma_2 \frac{\hbar^2}{2m_0}\left(k_x^2 + k_y^2 - 2k_z^2\right) \tag{49}$$

$$R = -\sqrt{3}\frac{\hbar^2}{2m_0}\left[\gamma_2\left(k_x^2 - k_y^2\right) - 2i\gamma_3 k_x k_y\right] \tag{50}$$

$$S = 2\sqrt{3}\gamma_3 \frac{\hbar^2}{2m_0} k_z\left(k_x - ik_y\right) \tag{51}$$

$$U = \frac{1}{\sqrt{3}} P_0 k_z \tag{52}$$

$$V = \frac{1}{\sqrt{6}} P_0\left(k_x - ik_y\right) \tag{53}$$

where E_C and $E_V = E_v^{av} + \Delta/3$ are unstrained conduction and valence band edge energies, respectively.

2.5.2 Strain Hamiltonian for Eight-band Model

The strain is incorporated into the eight-band Hamiltonian H_K with the addition of a strain Hamiltonian, derived by means of perturbation theory. [55,56] Under an arbitrary uniform strain, the crystal has new periodicity with the potential $V(\boldsymbol{r}; \overleftrightarrow{\mathbf{e}})$ in place of $V_0(\boldsymbol{r})$. In this case, the $\boldsymbol{k} \cdot \boldsymbol{p}$ equation $Hu_{n\boldsymbol{k}}(\boldsymbol{r}) = E_n(\boldsymbol{k})u_{n\boldsymbol{k}}(\boldsymbol{r})$ can be transformed to the deformed coordinate system $\boldsymbol{r}_j'$ using the transformation

$$\boldsymbol{r}_i = \sum_j \left(\delta_{ij} + e_{ij}\right)\boldsymbol{r}_j'. \tag{54}$$

A perturbation expansion in the deformed coordinate is performed, and then transformed back to the original coordinates. For small strains, the potential of the deformed crystal can be expanded to first order in the strain as:

$$V(\boldsymbol{r}; \overleftrightarrow{\mathbf{e}}) = V_0(\boldsymbol{r}') + \sum_{ij} V_{ij}(\boldsymbol{r}')e_{ij}, \tag{55}$$

where $V_{ij}(\boldsymbol{r}') = \left[\partial V(\boldsymbol{r}' + \overleftrightarrow{\mathbf{e}} \cdot \mathbf{r}'; \overleftrightarrow{\mathbf{e}})/\partial e_{ij}\right]_{e_{ij}=0}$. The eigenvalue problem in the deformed coordinate system, given in linear strain terms, is expressed as:

$$(H' + D)\tilde{u}_{n\boldsymbol{k}}(\boldsymbol{r}') = E_n(\boldsymbol{k})\tilde{u}_{n\boldsymbol{k}}(\boldsymbol{r}') \tag{56}$$

where $\tilde{u}_{n\boldsymbol{k}}(\boldsymbol{r}') = u_{n\boldsymbol{k}}(\boldsymbol{r})$. The Hamiltonian H' is the same as H, but $\boldsymbol{r}$ and $\boldsymbol{p}$ are replaced by $\boldsymbol{r}'$ and $\boldsymbol{p}'$. The terms linear in strain are given by (as functions of the operators $\boldsymbol{r}'$ and $\boldsymbol{p}'$),

$$D = D_0 + D_{\mathrm{k\cdot p}} + D_{\mathrm{so}} \tag{57}$$

where

$$D_0 = \sum_{ij} \left[-\frac{1}{m_0} p_i p_j + V_{ij}(\boldsymbol{r}) \right] e_{ij} \ , \tag{58}$$

$$D_{\mathrm{k \cdot p}} = -\frac{\hbar}{m_0} \boldsymbol{k} \cdot \overleftrightarrow{\mathbf{e}} \cdot \boldsymbol{p} \ , \tag{59}$$

$$D_{\mathrm{so}} = \frac{\hbar}{4 m_0^2 c^2} \left\{ \sum_{\boldsymbol{ij}} e_{ij} \left(\nabla V_{ij}(\boldsymbol{r}) \right) \times \boldsymbol{p} \cdot \boldsymbol{\sigma} - (\nabla V_0(\boldsymbol{r}) \cdot \overleftrightarrow{\mathbf{e}}) \times \boldsymbol{p} \cdot \boldsymbol{\sigma} - \nabla V_0(\boldsymbol{r}) \times (\overleftrightarrow{\mathbf{e}} \cdot \boldsymbol{p}) \cdot \boldsymbol{\sigma} \right\} \tag{60}$$

Considering only the first order perturbation terms, and neglecting the small spin-dependent strain interaction D_{so}, the strain Hamiltonian $D_0 + D_{\mathrm{k \cdot p}}$ can be written in the $|m\rangle$ basis order of $|S\rangle$, $|X\rangle$, $|Y\rangle$, $|Z\rangle$ as

$$\begin{bmatrix} a'(e_{xx} + e_{yy} + e_{zz}) & b' e_{yz} - i P_0 \sum_j e_{xj} k_j & b' e_{xz} - i P_0 \sum_j e_{yj} k_j & b' e_{xy} - i P_0 \sum_j e_{zj} k_j \\ b' e_{yz} + i P_0 \sum_j e_{xj} k_j & l e_{xx} + m(e_{yy} + e_{zz}) & n e_{xy} & n e_{xz} \\ b' e_{xz} + i P_0 \sum_j e_{yj} k_j & n e_{xy} & l e_{yy} + m(e_{xx} + e_{zz}) & n e_{yz} \\ b' e_{xy} + i P_0 \sum_j e_{zj} k_j & n e_{xz} & n e_{yz} & l e_{zz} + m(e_{xx} + e_{yy}) \end{bmatrix} \tag{61}$$

where e_{ij} is the strain tensor, $l = \langle x | D_{xx} | x \rangle$, $m = \langle y | D_{xx} | y \rangle$ and $n = 2\langle x | D_{xz} | z \rangle$ are strain interactions between valence bands, $a' = \langle s | D_{xx} | s \rangle$ is the conduction band hydrostatic deformation potential and $b' = 2\langle s | D_{xy} | z \rangle$ is a small conduction band shear deformation potential (also an inversion symmetry parameter and is neglected for the same reasons as B).

The eight-band strain Hamiltonian can be written as block diagonal matrix of equation (61) (with $b' = 0$), with orbital Bloch basis in the order of $|S \uparrow\rangle$, $|X \uparrow\rangle$, $|Y \uparrow\rangle$, $|Z \uparrow\rangle$, $|S \downarrow\rangle$, $|X \downarrow\rangle$, $|Y \downarrow\rangle$, and $|Z \downarrow\rangle$ for rows and columns. In order to couple this strain Hamiltonian to the kinetic part of the eight-band Hamiltonian H_K in equation (46), the same unitary transformation described in equation (44) has to be applied to obtain the final form of H_S in the total angular momentum basis. This is given as [59]

$$H_S = \begin{pmatrix} a_c e_a & 0 & -v^* & 0 & -\sqrt{3}v & \sqrt{2}u & u & -\sqrt{2}v^* \\ 0 & a_c e_a & \sqrt{2}u & \sqrt{3}v^* & 0 & v & -\sqrt{2}v & -u \\ -v & \sqrt{2}u & -p+q & -s^* & r & 0 & \sqrt{\frac{3}{2}}s & -\sqrt{2}q \\ 0 & \sqrt{3}v & -s & -p-q & 0 & r & -\sqrt{2}r & \frac{1}{\sqrt{2}}s \\ -\sqrt{3}v^* & 0 & r^* & 0 & -p-q & s^* & \frac{1}{\sqrt{2}}s^* & \sqrt{2}r^* \\ \sqrt{2}u & v^* & 0 & r^* & s & -p+q & \sqrt{2}q & \sqrt{\frac{3}{2}}s^* \\ u & -\sqrt{2}v^* & \sqrt{\frac{3}{2}}s^* & -\sqrt{2}r^* & \frac{1}{\sqrt{2}}s & \sqrt{2}q & -p & 0 \\ -\sqrt{2}v & -u & -\sqrt{2}q & \frac{1}{\sqrt{2}}s^* & \sqrt{2}r & \sqrt{\frac{3}{2}}s & 0 & -p \end{pmatrix} \tag{62}$$

where

$$e_h = e_{xx} + e_{yy} + e_{zz} \tag{63}$$

$$p = a_v e_h \tag{64}$$

$$q = b\left[e_{zz} - \frac{1}{2}\left(e_{xx} + e_{yy}\right)\right] \tag{65}$$

$$r = \frac{\sqrt{3}}{2} b\left(e_{xx} - e_{yy}\right) - ide_{xy} \tag{66}$$

$$s = -d(e_{zz} - ie_{zz}) \tag{67}$$

$$u = \frac{1}{\sqrt{3}} P_0 \sum_j e_{zj} k_j \tag{68}$$

$$v = \frac{1}{\sqrt{3}} P_0 \sum_j \left(e_{xj} - e_{yj}\right) k_j \ . \tag{69}$$

Here a_c is the conduction band hydrostatic deformation potential; a_v is the valence band hydrostatic deformation potential; and b and d are the valence band shear deformation potentials. These deformation potentials are related to the a', l, m, n terms by:

$$a_c = a' \quad , \quad a_v = \tfrac{1}{3}(l + 2m) \quad , \quad b = \tfrac{1}{3}(l - m) \quad , \quad d = \tfrac{1}{\sqrt{3}} n \ . \tag{70}$$

This strain Hamiltonian H_S is then coupled to the kinetic part of the Hamiltonian H_K, as shown in equation (46), to form the complete strain-dependent eight-band Hamiltonian:

$$H_T = H_K + H_S\,. \tag{71}$$

2.5.3 Six- and Four-band Model for Valence Bands

Although the eight-band Hamiltonian has been employed in this work for multi-band modelling, it is worth mentioning that this Hamiltonian can be easily reduced to a simpler model to suit particular situations. In the case where the band gap is large, the conduction band can be considered as decoupled from the valence bands. The eight-band Hamiltonian H_T can then be decomposed into two diagonal block matrices: upper-left 2×2 matrix for the conduction band and lower-right 6×6 matrix for the valence bands, ignoring the off diagonal block matrix. The 2×2 matrix for the conduction band is the same as the one-band model. The 6×6 matrix for valence band is known as the Luttinger-Kohn (LK) Hamiltonian. [14,78,79] Furthermore, if the Γ_7 spin-orbit split-off band is far from the Γ_8 valence bands, the modelling of valence band can be simplified to the centre 4×4 matrix of H_T.

Note that the LK model was developed to calculate only the valence bands prior to the eight-band model. Within the LK model, the interaction between the conduction band and the valence bands is incorporated in the Luttinger parameters γ_i^L, whereas this interaction is explicitly accounted for in the eight-band model. This is why these parameters are modified in the eight-band model to remove the similar effect, given by equation (41) in Section 2.5.1. Hence, the ordinary Luttinger parameters γ_i^L are used instead of γ_i in the reduced model.

2.6 Coulomb Interaction

Confined charge carriers interact via the Coulomb interaction. For two particles of different charge, i.e. electron and hole, the energy of the system is lowered due to attraction and an exciton is formed. In a bulk crystal, an exciton can dissociate into a pair of free carriers in the conduction and valence bands. In a quantum dot, an exciton is formed automatically when the ground states of electrons and holes are populated. [6] A pair of particles with charge q at position $\boldsymbol{r}$ contributes the Coulomb interaction energy to the system, as expressed by:

$$\mathrm{W_{ij}}(\boldsymbol{r}_\mathrm{i},\boldsymbol{r}_\mathrm{j}) = \frac{1}{4\pi\varepsilon_0\varepsilon_\mathrm{r}}\frac{\mathrm{q_i q_j}}{|\boldsymbol{r}_\mathrm{i}-\boldsymbol{r}_\mathrm{j}|}, \tag{72}$$

where ε_0 is the vacuum dielectric constant and ε_r is the relative dielectric constant.

For typical III-V compounds, the bulk exciton radius is > 10 nm and is determined by the dielectric constant and carrier effective mass. This results in the strong carrier confinement for quantum dots of similar dimension in which the kinetic energy due to size quantisation is the dominant energy contribution. In this case, the Coulomb interaction energy is small as compared to the separation of ground and excited states for both electrons and holes. The exciton binding energy and the difference of eigenenergies of a Hamiltonian with and without Coulomb interaction can be calculated using perturbation theory. To first order, it is

$$E_X = \langle 00|\mathrm{W_{eh}}|00\rangle = \iint \Psi_0(\boldsymbol{r}_\mathrm{e})\Psi_0(\boldsymbol{r}_\mathrm{h})\,\mathrm{W_{eh}}(\boldsymbol{r}_\mathrm{e},\boldsymbol{r}_\mathrm{h})\Psi_0(\boldsymbol{r}_\mathrm{e})\Psi_0(\boldsymbol{r}_\mathrm{e})\mathrm{d}^3\boldsymbol{r}_\mathrm{e}\mathrm{d}^3\boldsymbol{r}_\mathrm{h} \tag{73}$$

In this case, for instance, the lowest interband transition becomes

$$\mathrm{T1} = E_\mathrm{e0} - E_\mathrm{h0} - E_X \tag{74}$$

where E_e0 and E_h0 are the ground state energy of the electron and hole, respectively.

2.7 Electron-photon Interaction

After obtaining the band structure and the wave functions, the interaction between the electron and the photon (the electromagnetic wave) has to be evaluated in order to determine the optical transitions and to simulate the spectra. A (e.g. upward) transition occurs because the oscillating field of the photon alters the oscillating phase of an electron wave function (of a lower energy state) to become similar to that of another electron wave function (of a higher energy state), resulting in strong coupling between the two electron states. [77] In most cases, a set of density of states is coupled to the initial electron wave function.

The light's interaction with the electron enters into Schrodinger equation through the vector potential $\boldsymbol{A}(\boldsymbol{r},t) = \hat{\mathbf{e}}\,\mathrm{Re}\{A(\boldsymbol{r})e^{i\omega t}\} = \hat{\mathbf{e}}\frac{1}{2}\{A(\boldsymbol{r})e^{i\omega t} + A^*(\boldsymbol{r})e^{-i\omega t}\}$.

The Hamiltonian is given by:

$$H = \frac{(\boldsymbol{p} + q\boldsymbol{A})^2}{2m_0} + V(\boldsymbol{r}) \approx \frac{\boldsymbol{p}^2 + 2q\boldsymbol{A}\cdot\boldsymbol{p}}{2m_0} + V(\boldsymbol{r}) = H_0 + H'(\boldsymbol{r})[e^{i\omega t} + e^{-i\omega t}] \tag{75}$$

$$H'(\boldsymbol{r}) = \frac{qA(\boldsymbol{r})}{2m_0}\hat{\mathbf{e}}\cdot\boldsymbol{p} \tag{76}$$

where q is the magnitude of the electron charge, H_0 is the original Hamiltonian and H' is the perturbation term. The quantum mechanical transition rate is governed by *Fermi's Golden Rule* and is expressed per unit volume of active material (in units of s^{-1}cm^{-3}) as

$$R = \frac{2\pi}{\hbar}|H'_{21}|^2\rho_f(E_{21})\big|_{E_{21}=\hbar\omega} \tag{77}$$

where

$$H'_{21} \equiv \langle\Psi_2|H'(\boldsymbol{r})|\Psi_1\rangle\,. \tag{78}$$

Both the optical matrix element $|H'_{21}|^2$ and the density of final states $\rho_f(E_{21})$ are evaluated at $E_{21} = \hbar\omega$.

The optical matrix element, which determines the strength of interaction between two states, depends on their wavefunctions. Since the spatial variation of $A(\boldsymbol{r})$ is typically much slower than that of the envelope/Bloch function, $A(\boldsymbol{r})$ is treated as a constant A_0. [77] With the product of the momentum operators given by $\boldsymbol{p}\mathrm{AB} = \mathrm{B}\boldsymbol{p}\mathrm{A} + \mathrm{A}\boldsymbol{p}\mathrm{B}$, equation (78) can be expanded in terms of the envelope (ϕ) / Bloch (u) function formalism as:

$$H'_{21} = \sum_{i,j}\left\langle \phi_{2,\mathrm{j}}u_{2,\mathrm{j}}\left|\frac{qA(\boldsymbol{r})}{2m_0}\hat{\mathbf{e}}\cdot\boldsymbol{p}\right|\phi_{1,\mathrm{i}}u_{1,\mathrm{i}}\right\rangle \tag{79}$$

$$H'_{21} = \frac{qA_0}{2m_0}\sum_{i,j}\left[\langle\phi_{2,\mathrm{j}}|\phi_{1,\mathrm{i}}\rangle\langle u_{2,\mathrm{j}}|\hat{\mathbf{e}}\cdot\boldsymbol{p}|u_{1,\mathrm{i}}\rangle + \langle u_{2,\mathrm{j}}|u_{1,\mathrm{i}}\rangle\langle\phi_{2,\mathrm{j}}|\hat{\mathbf{e}}\cdot\boldsymbol{p}|\phi_{1,\mathrm{i}}\rangle\right]. \tag{80}$$

The optical matrix element $|H'_{21}|^2$ can then be rewritten as

$$|H'_{21}|^2 = \left(\frac{qA_0}{2m_0}\right)^2|M_T|^2\,, \tag{81}$$

$$|M_T|^2 = \left|\sum_{i,j}\left[\langle\phi_{2,\mathrm{j}}|\phi_{1,\mathrm{i}}\rangle\langle u_{2,\mathrm{j}}|\hat{\mathbf{e}}\cdot\boldsymbol{p}|u_{1,\mathrm{i}}\rangle + \langle u_{2,\mathrm{j}}|u_{1,\mathrm{i}}\rangle\langle\phi_{2,\mathrm{j}}|\hat{\mathbf{e}}\cdot\boldsymbol{p}|\phi_{1,\mathrm{i}}\rangle\right]\right|^2\,, \tag{82}$$

where $|M_T|^2$ is the transition matrix element. The first term in the bracket gives the interband optical transition strength, while the second term gives the intraband optical transition strength. These can be determined based on the orthogonality of the Bloch functions.

For an interband transition (i.e. $i \neq j$), the second term disappears because $\langle u_{\mathrm{j}} | u_{\mathrm{i}} \rangle = 0$. Therefore, the transition strength is essentially determined by the symmetry properties and spatial overlap of the electron and hole states. There is no a strict selection rule for interband transitions in quantum dots. Typically one looks for those transitions in which the electron and hole wave functions are significantly overlapped. [68] Explicit calculations of the interband transition matrix element are not considered in this study.

As for intraband transitions (i.e. $i = j$), due to the fact that $\langle u_{\mathrm{i}} | \boldsymbol{p} | u_{\mathrm{i}} \rangle = 0$, the first term of equation (82) is neglected and only the second term is considered. Since $\langle u_{\mathrm{i}} | u_{\mathrm{i}} \rangle = 1$, the transition strength is then governed by the dipole moment of the two wave functions. In addition, intraband transitions follow strict selection rules. For instance, in the conduction band, for two electron states of $|a\rangle = |ijk\rangle$ and $|b\rangle = |i'j'k'\rangle$ it is necessary to have an odd number for at least one of the expressions $(i - i')$, $(j - j')$ or $(k - k')$. Otherwise, the transition would be forbidden.

2.8 Numerical Technique - Finite Element Method

The finite element method (FEM) is a popular numerical technique used to approximate the solution of a partial differential equation (PDE). It was first developed for macroscopic structural analysis, then being expanded to work in virtually any application that could be expressed in terms of partial differential equations. [80,81,82] Since the modelling approaches for band structure and strain field are both continuum models, the FEM, being developed for the continuum problem, is a suitable candidate as a computing platform. Indeed, the employment of FEM in the field of semiconductors is not uncommon. Successful calculations of strain and electronic band structure based on the FEM approach have been reported for different quantum heterostructures. [67,83,84,85,86]

2.8.1 General FEM Approach

In general, the employment of FEM can be summarised in a few basic steps as follows:

(1) *Element definition*: It divides the continuous domain into discrete sub-regions called elements. These elements are usually, however not restricted to, simple geometrical

forms such as triangles and tetrahedrons. The elements are connected together by connecting points called *nodes*, which appear on the boundaries of the elements.

(2) *Element interpolation*: The behaviour of each element is then described in a simple way, such that the *field quantity* (e.g. displacement in strain analysis) at an arbitrary point within an element is interpolated from the values of the field quantity at the nodes. The components of the field quantity at each node are the degrees of freedom (DOF).

(3) *Energy formulation*: Typically, some characteristic functions (e.g. strain energy in strain analysis) of each element are formulated.

(4) *Assembly*: By connecting the elements together, the field quantity becomes interpolated over the entire structure in piecewise fashion, by as many polynomial expressions as there are elements.

(5) *Minimisation and solution*: The "best" solution is found by the minimisation of the functions (e.g. total energy). This results in a set of simultaneous algebraic equations for values of the field quantity at nodes. In matrix form, this is represented by:

$$\mathbf{K}\mathbf{D} = \mathbf{F}, \tag{83}$$

where $\mathbf{D}$ is a vector of the unknown field quantity, $\mathbf{F}$ is a vector of known loads, and $\mathbf{K}$ is a matrix of known constants. This unknown vector is then solved by means of either direct or iterative methods. Direct solvers are more efficient although they consume more memory resources. In contrast, iterative solvers are more flexible in terms of memory resource but may take much longer time and are potentially unstable. [See reference 81 for details]

FEM is typically integrated with a geometric modelling technique used in computer aided designs. The graphic user interface allows the FEM software to handle complicated domains (geometries) and constraints (boundary conditions) with relative ease. One of the major advantages of FEM is the flexibility to vary the desired precision over the entire domain by controlling the quality of the mesh (i.e. element size). This means that higher accuracy prediction can be obtained at regions of interest (e.g. at and around interfaces of different materials), and/or lower computational cost can be achieved by reducing the precision in regions where an insignificant change in the solution is expected (e.g. substrate).

In addition to open source codes, there are quite a number of commercial FEM software (e.g. COMSOL Multiphysics, ANSYS, ABAQUS, etc) available for researchers from different fields to employ FEM without the need to write a code from scratch. Some software specialises in particular problems (such as structural mechanical, fluid dynamic, heat transfer) and some offer implementation for virtually any partial differential equation based problems. In this work, COMSOL Multiphysics is used, not only for its explicit equation based platform which allows solving for virtually any PDE based problems, but also for its capability to couple different physical problems into one single model. This feature is important as it is a requirement of this work to use solutions of solved problems as inputs for the next calculation. For example, the solutions of the strain field calculations (structural mechanical problem) and piezoelectric calculations (Poisson equation with the solution of the strain field calculation) are inputs to solve the band structure (eigenvalue problem). In addition, there is the option to write custom codes for modelling algorithms and sequences, which is useful for a self-consistent model where automated iterations between two different settings can be performed. On top of that, it is also compatible with the more commonly used modelling package, MATLAB, which is handy for further analysis. In this work, the calculations of the exciton binding energy, transition matrix elements and the spectra simulation have made use of this software.

For reference purposes, all calculations were performed using a mainstream PC with a 3GHz quad-core (four threads) processor and 8GB of DDR2 dual-channel random access memory (RAM), running on a Microsoft Windows XP 64-bit operating system. The average computational time for a run is about 0.5-2 hours depending on the Hamiltonian (single- or multi-band) and the number of solutions required in the band structure calculation. In this work, the model is built and meshed with the intention to fully utilise the memory capacity (more elements to improve accuracy), while not exceeding the limit (to reduce computational time by avoiding using virtual memory on a mechanical hard drive).

2.8.2 Modelling Procedures for Quantum Dots

Most of the work here concerns quantum dot based structures in a 3D model, hence this is used as an example to present the calculation procedures. In general, the calculations can be separated into two sections as shown in Figure 8: calculations of the electronic band structure using COMSOL Multiphysics and to post-process of these results (i.e. energy levels and wave functions) for optical properties in the MATLAB environment. In this subsection, the procedure for such a routine modelling from initial geometrical setup to obtaining solutions of band structure calculations will be discussed. Some underlying operations of the FEM program will be explained in details. [81,87] Further analysis of the calculated results are addressed in Appendix A since this involves mainly running programming codes based on the corresponding mathematic formulation described in Section 2.6 and 2.7.

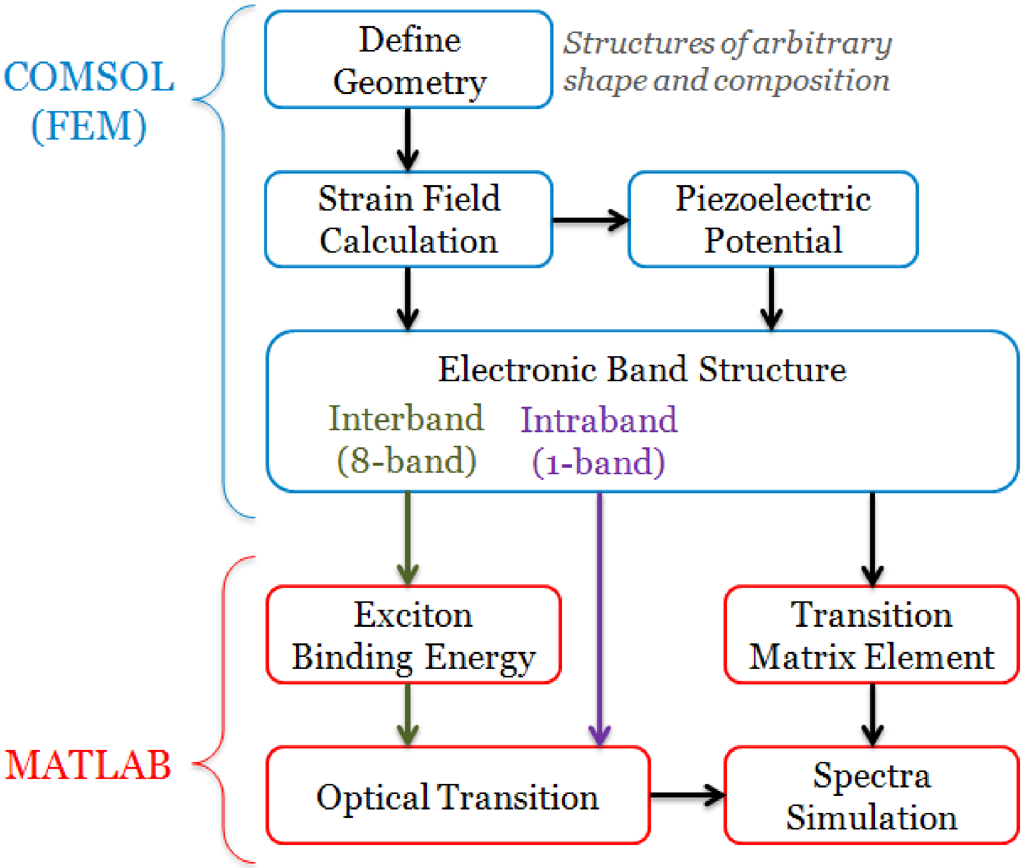

Figure 8. *Flowchart of computational procedures.*

Initial Model Setup

Step 1: Application Modes

After opting for a 3D model in COMSOL, modules of particular physical problems are added to the model depending on the application. Essentially, each module comes with different default equations where their coefficients are modified to suit the problem under study. In the order of calculation, the three problems/modules and their corresponding settings used for all quantum dot models are listed in Table 1. The variable(s) for the electronic band structure calculation depend on the Hamiltonian to be employed, either one-band or eight-band.

Calculation	Physics Model	Variables
Strain Field	[Structural Mechanics] > [Solid, Strain Stress] > [Static Analysis]	u,v,w,p
Piezoelectric Potential	[PDE Mode] > [PDE, Coefficient Form] > [Stationary Analysis]	Vp
Band Structure	[PDE Mode] > [PDE, Coefficient Form] > [Eigenvalue Analysis]	u1-u8 for 8-band, or u9 for 1-band.

Table 1. *Multiphysics models and types of element used.*

Step 2: Define geometry

Next, the geometry of the structure under study is plotted. In this case, it is a truncated conical QD (blue region) on a wetting layer (red region) in a substrate matrix, as shown in Figure 9. The geometrical parameters are chosen to suit all three calculations. A cylindrical geometry is presented here, for which the particle-in-a-box type of boundary condition will be employed, to improve the computational efficiency while retaining a 3D model. For implementation of periodic boundary conditions, a rectangular geometry for WL/matrix is used instead.

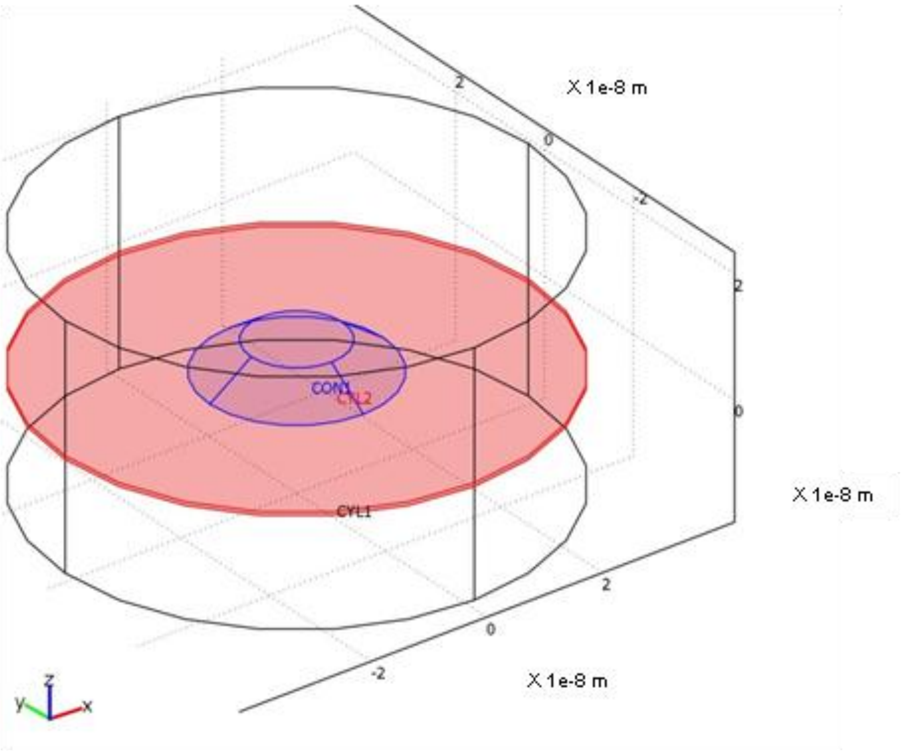

Figure 9. *Geometry of a typical truncated conical QD used. Blue and red regions are dot and wetting layer, respectively, and the rest of the structure is substrate material.*

Step 3: Mesh geometry

The structure is then subdivided into grid/mesh by elements as described earlier. By default, COMSOL Multiphysics uses Lagrange quadratic tetrahedrons as 3D elements. Although the 10-node quadratic tetrahedron elements (Figure 10a) are normally used in this work, for simplicity, the 4-node linear tetrahedron element (Figure 10b) is used here for explanation instead. As shown in Figure 10c, the mesh quality is set to be relatively high at the interface and in the quantum dot, where the studied physical properties such as strain and wave function are expected to fluctuate more as compared to other regions. In other words, the element size is smaller and hence density is higher at the aforementioned regions. Once the geometry is properly meshed, it is ready for strain calculation.

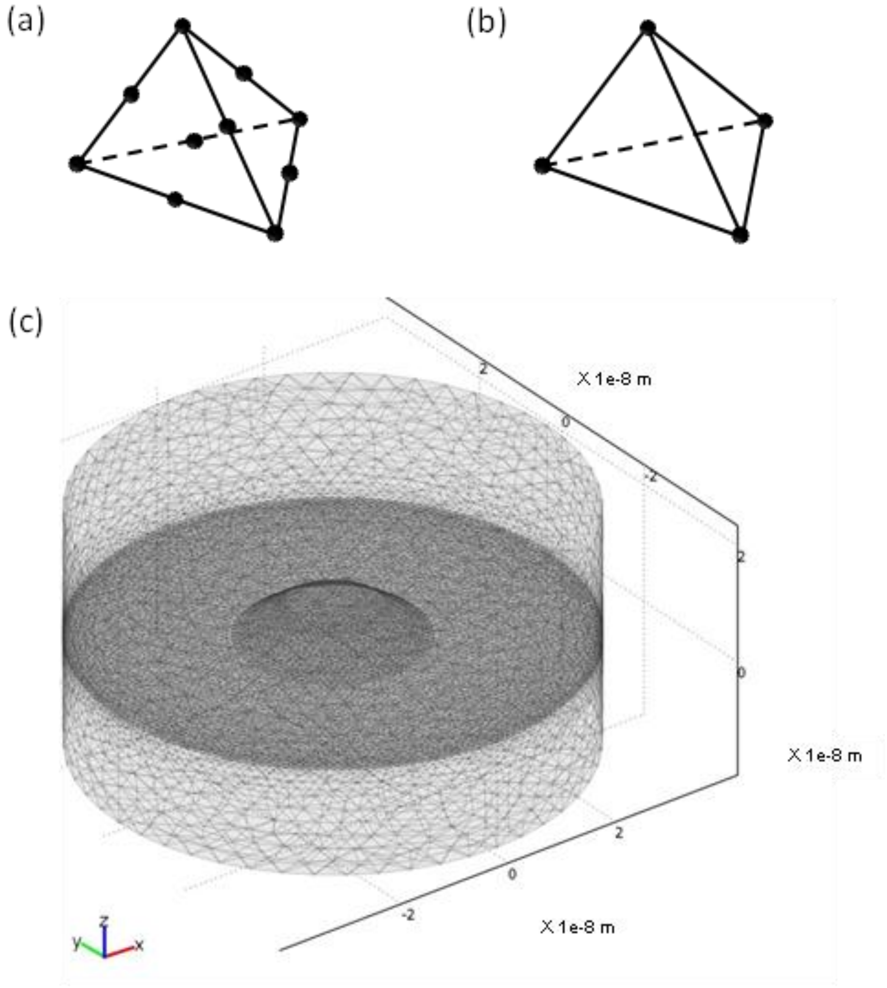

Figure 10. *(a) Quadratic, and (b) linear tetrahedron elements. (c) Meshed structure.*

Strain Field Calculation

Step 4a: Set physical properties

In this step, the physical properties of each subdomain are set, i.e. the governing equations and material properties. For strain analysis, the displacements are the unknowns, while anisotropic elastic stiffness matrix and lattice constants are piecewise-inputs to the calculations. Each node i in each element displaces in $x,\ y,\ z$ directions (labelled as $u_i,\ v_i,\ w_i$). The element nodal displacement vector is given by:

$$\mathbf{d^e} = [u_1 \quad v_1 \quad w_1 \quad u_2 \quad v_2 \quad w_2 \quad u_3 \quad v_3 \quad w_3 \quad u_4 \quad v_4 \quad w_4]^{\mathrm{T}} \tag{84}$$

The element type defines the interpolation scheme within an element. Assuming linear interpolation within an element for 4-node tetrahedron, the displacements are

$$u = \alpha_1 + \alpha_2 x + \alpha_3 y + \alpha_4 z,\ \ v = \alpha_5 + \alpha_6 x + \alpha_7 y + \alpha_8 z,\ w = \alpha_9 + \alpha_{10} x + \alpha_{11} y + \alpha_{12} z \tag{85}$$

where α_i are constants determined by equating $u_i,\ v_i$, and w_i to their corresponding nodal values $x_i,\ y_i$, and z_i, respectively. After substituting the resulting coefficients (in terms of $u,\ v,\ w,\ x,\ y,\ z$) back into equation (85), a rearrangement of the terms gives the displacement within an element in the form of $\mathbf{u} = \mathbf{N^e d^e}$,

$$\begin{bmatrix} u \\ v \\ w \end{bmatrix} = \begin{bmatrix} N_1 & 0 & 0 & N_2 & 0 & 0 & N_3 & 0 & 0 & N_4 & 0 & 0 \\ 0 & N_1 & 0 & 0 & N_2 & 0 & 0 & N_3 & 0 & 0 & N_4 & 0 \\ 0 & 0 & N_1 & 0 & 0 & N_2 & 0 & 0 & N_3 & 0 & 0 & N_4 \end{bmatrix} \begin{bmatrix} u_1 \\ v_1 \\ w_1 \\ \vdots \\ u_4 \\ v_4 \\ w_4 \end{bmatrix} \tag{86}$$

where the shape functions $N_i = \frac{1}{6V}(a_i + b_i x + c_i y + d_i z)$. The volume of the tetrahedron, V, and the geometrical constants $a_i,\ b_i,\ c_i$ and d_i are given by:

$$a_i = det \begin{vmatrix} x_2 & y_2 & z_2 \\ x_3 & y_3 & z_3 \\ x_4 & y_4 & z_4 \end{vmatrix},\ \ b_i = -det \begin{vmatrix} 1 & y_2 & z_2 \\ 1 & y_3 & z_3 \\ 1 & y_4 & z_4 \end{vmatrix},\ \ c_i = -det \begin{vmatrix} x_2 & 1 & z_2 \\ x_3 & 1 & z_3 \\ x_4 & 1 & z_4 \end{vmatrix}$$

$$d_i = -det \begin{vmatrix} x_2 & y_2 & 1 \\ x_3 & y_3 & 1 \\ x_4 & y_4 & 1 \end{vmatrix},\ \ 6V = det \begin{vmatrix} 1 & x_1 & y_1 & z_1 \\ 1 & x_2 & y_2 & z_2 \\ 1 & x_3 & y_3 & z_3 \\ 1 & x_4 & y_4 & z_4 \end{vmatrix} \tag{87}$$

Recall that the infinitesimal strain tensors are given by the spatial derivative of the displacements as shown in equation (7). Following the description of displacement (i.e. $\mathbf{u} = \mathbf{N^e d^e}$) derived above, the strain tensors can be expressed as $\mathbf{e} = \mathbf{B^e d^e}$, where $\mathbf{B^e}$ is the derivative of the shape function matrix. The displacement field can then be solved by minimising the total energy of the system shown by the following expression

$$\frac{\partial U}{\partial q_j} = Q_j \,, \tag{88}$$

where U is the strain energy, q_j is the generalised displacement and Q_j is the generalised force. According to Hooke's law, the stress-strain relation is given by $\boldsymbol{\sigma} = \mathbf{Ee}$, where $\boldsymbol{\sigma}$ is the stress tensor and $\mathbf{E}$ is the elasticity matrix or stiffness matrix. The strain energy density, in the general form of $\frac{1}{2}\boldsymbol{\sigma}\mathbf{e}$, gives

$$U = \frac{1}{2}(\mathbf{Ee})^{\mathrm{T}}\mathbf{e} = \frac{1}{2}\mathbf{d}^{\mathbf{e}\mathrm{T}}\left(\mathbf{B}^{\mathbf{e}\mathrm{T}}\mathbf{E}\mathbf{B}^{\mathbf{e}}\right)\mathbf{d}^{\mathbf{e}} \,. \tag{89}$$

The strain energy of an element can be obtained by integrating the strain energy density over its volume. Hence the strain energy of an element is

$$U^{\mathbf{e}} = \frac{1}{2}\mathbf{d}^{\mathbf{e}\mathrm{T}}\mathbf{k}^{\mathbf{e}}\mathbf{d}^{\mathbf{e}} \,, \tag{90}$$

where the element stiffness matrix is $\mathbf{k}^{\mathbf{e}} = \int_{\mathrm{V}} \left(\mathbf{B}^{\mathbf{e}\mathrm{T}}\mathbf{E}\mathbf{B}^{\mathbf{e}}\right)\mathrm{dV}$. Assuming the entire structure has adapted to the lattice constant of the substrate, the QD/WL is subjected to initial strain $\mathbf{e_0}$ equal to the lattice mismatch. By using the stress-strain relation $\boldsymbol{\sigma} = \mathbf{E}(\mathbf{e} - \mathbf{e_0})$, the total energy of the element has the form:

$$\chi^{\mathrm{e}} = \frac{1}{2}\mathbf{d}^{\mathbf{e}\mathrm{T}}\mathbf{k}^{\mathbf{e}}\mathbf{d}^{\mathbf{e}} - \mathbf{d}^{\mathbf{e}\mathrm{T}}\mathbf{f}^{\mathbf{e}} \,, \tag{91}$$

where $\mathbf{f}^{\mathbf{e}} = \int_{\mathrm{V}} \left(\mathbf{B}^{\mathbf{e}\mathrm{T}}\mathbf{E}\mathbf{e_0}\right)\mathrm{dV}$ is a vector of the element nodal load caused by the initial strain.

Step 4b: Set boundary conditions

Next, the boundary condition for each interface is set. For the strain field calculation, the in-plane positions (i.e. *x* and *y*) are fixed for all interfaces to reflect the lattice matching with the substrate. In addition, the bottom of the substrate is constrained in the *z* direction, as shown in Figure 11.

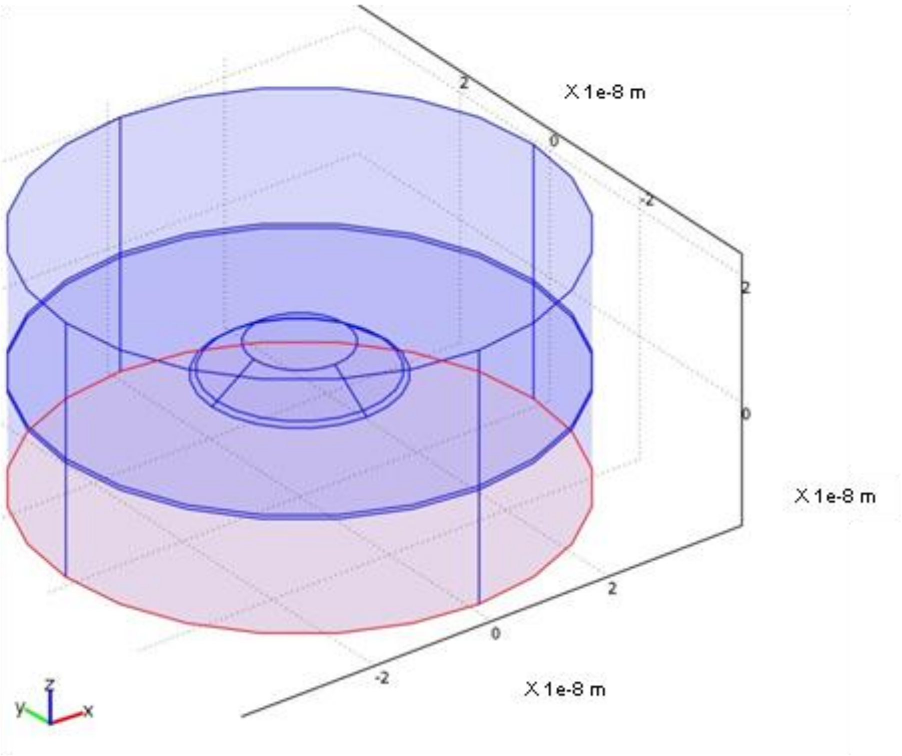

Figure 11. *Boundary conditions: blue interface = constrained in x and y direction; red interface = constrained in all directions.*

Step 4c: Set solver parameters and solve problem

For strain field calculations, a stationary direct solver is used since it is a stationary problem. All initial values are set to obtain initial expressions/inputs and the program is set to solve for only variables associated with the strain field, as listed in Table 1. Now, we are ready to perform the strain field calculation.

Solver	Stationary, Direct
Initial Value	Initial value expression
Values of variables not solved for and linearization point	Use setting from Initial value frame
Solve for variables	u, v, w

Table 2. *Solver and initial value settings for strain field calculation.*

During the execution of the calculations, the equations as in (91) for each element are assembled to form matrices of the entire (global) system. Each element has 4 nodes with 3 DOFs at each node. Therefore, a system of m elements has a total DOF of $n = 12m$. The total energy of the system is therefore given as

$$\boldsymbol{\chi} = \sum_{\mathrm{e}=1}^{m} \chi^{\mathrm{e}} = \frac{1}{2}\mathbf{D}^{\mathrm{T}}\mathbf{K}\mathbf{D} - \mathbf{D}^{\mathrm{T}}\mathbf{F}\,. \tag{92}$$

In order to solve for the displacement $\mathbf{D}$, the total energy of the system $\boldsymbol{\chi}$ has to be minimised such that the partial derivative of $\boldsymbol{\chi}$ is zero for unconstrained DOFs. This implies

$$\mathbf{d}\boldsymbol{\chi} = \mathbf{KD} - \mathbf{F} \tag{93}$$

where $\mathbf{d}\boldsymbol{\chi} = \begin{bmatrix} \frac{\partial\boldsymbol{\chi}}{\partial\mathbf{D}_1} & \frac{\partial\boldsymbol{\chi}}{\partial\mathbf{D}_2} & \cdots & \frac{\partial\boldsymbol{\chi}}{\partial\mathbf{D}_n} \end{bmatrix}^{\mathrm{T}}$. The constrained DOFs (where boundary conditions are applied) are excluded from the equation set because the "unknowns" are defined. Therefore, for a system with r constrained DOFs, the n equations can be reduced to $(n-r)$ equations. The general equation becomes $\mathbf{KD} = \mathbf{F}$ in which the displacements are then solved by either direct method or iterative method. [81] Finally, the strain fields are then obtained by using the strain-displacement relation as derived in equation (7). The outputs of the strain field calculation are then stored manually for use in other physical models. For example, Figure 12 shows the strain tensor e_{zz} solved for a InAs/GaAs QD.

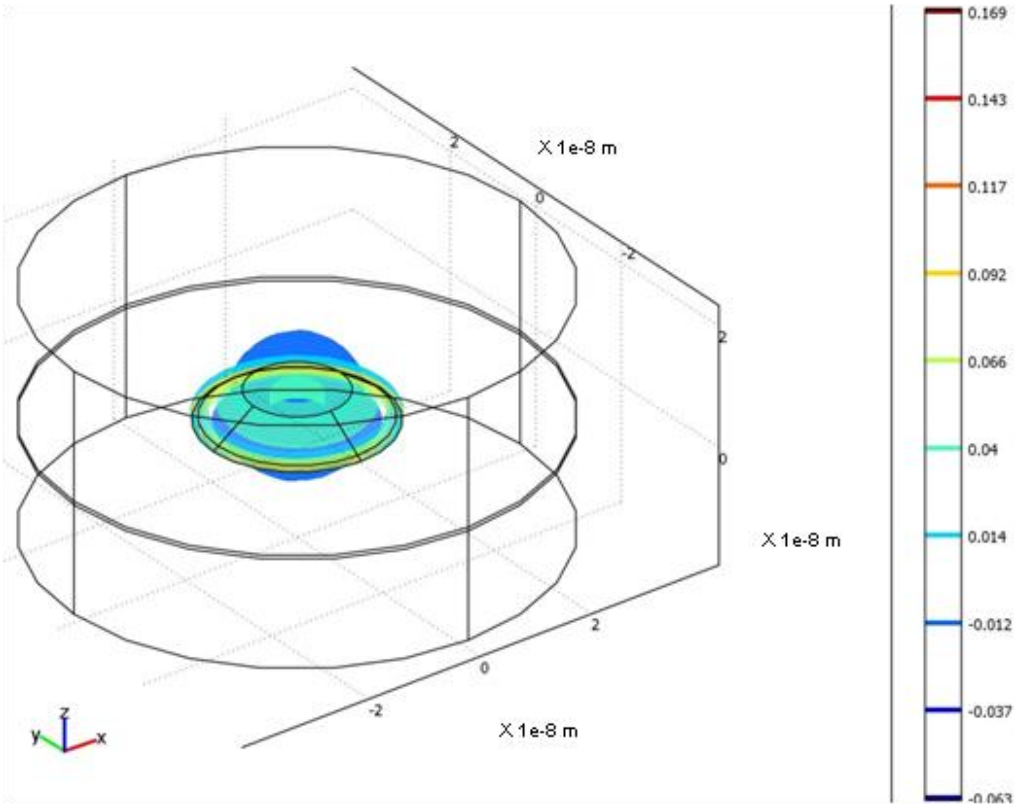

Figure 12. *Example of strain tensor e_{zz} solved for a InAs/GaAs QD.*

Piezoelectric Potential Calculation

Step 5a: Set physical properties

By using the model navigator, the in-use physics model is switched to PDE coefficient form corresponds to the piezoelectric potential calculation. In this case, the COMSOL default PDE equation is given in the form of:

$$\nabla \cdot (-\mathrm{c}\nabla \mathrm{Vp} - \alpha \mathrm{Vp} + \gamma) + \mathrm{aVp} + \beta \cdot \nabla \mathrm{Vp} = d_a \lambda \mathrm{Vp} - e_a \lambda^2 \mathrm{Vp}\,. \tag{94}$$

By comparing to the corresponding Poisson's equation for the piezoelectric potential, Vp, (equation (18) of Section 2.2.3) the coefficients are set to match as shown in Table 3:

c	$-\varepsilon_s \varepsilon_0$
a	0
d_a	1
e_a	0
α	$(0 \quad 0 \quad 0)$
β	$(0 \quad 0 \quad 0)$
γ	$2\mathbf{e}_{14}(e_{yz} \quad e_{xz} \quad e_{xy})$

Table 3. *Coefficients for Poisson equation in the piezoelectric potential calculation.*

Step 5b: Set boundary conditions

The boundaries are set to Dirichlet (i.e. variable Vp = 0) for all interfaces, except for internal boundaries. Here they are set to Neumann boundary conditions instead such that the terms in the bracket of equation (94) are the same on both sides of the interface.

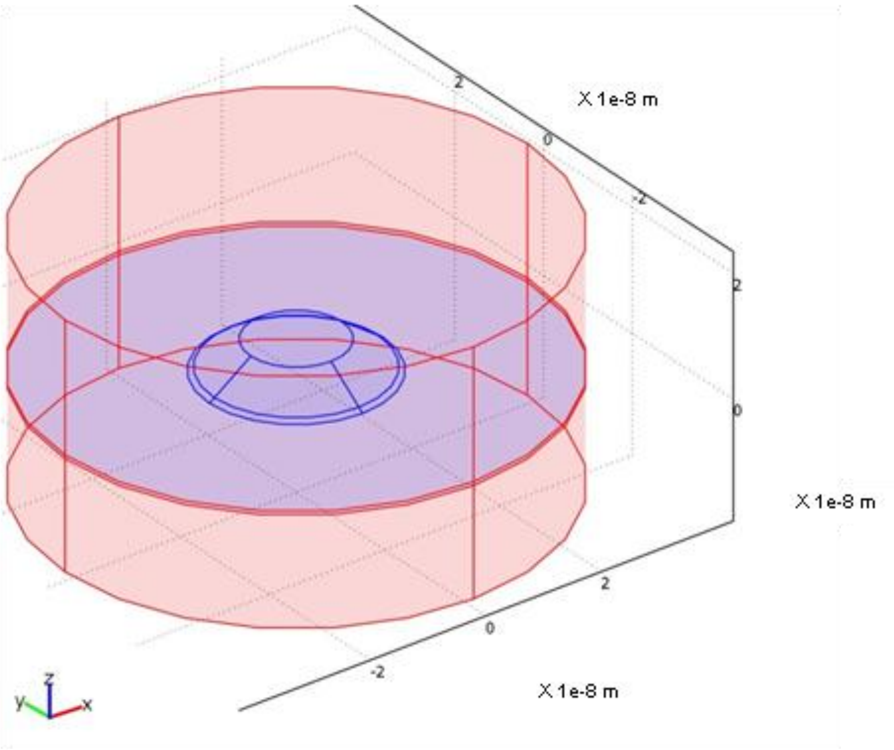

Figure 13. *Boundary conditions: Dirichlet (variable is forced to be zero) for red interface, and Neumann (continuous derivative of variable) for blue interface.*

Step 5c: Set solver parameters and solve problem

Again, the piezoelectric potential calculation is a stationary problem. Therefore a stationary direct solver is used. Since the stored solutions from previous strain field calculations are the inputs to this model, the settings for variables have to be changed accordingly as shown in Table 4 before each calculation is performed.

Solver	Stationary, Direct
Initial Value	Initial value expression evaluated using stored solution
Values of variables not solved for and linearization point	Stored solution
Solve for variables	Vp

Table 4. *Solver and initial value settings for the piezoelectric potential calculation.*

In contrast to the strain field calculation, each node only has one DOF, and hence the global DOF is 3 times smaller. Once the calculation is completed, the solution is then stored again for band structure calculations. Figure 14 shows an example of piezoelectric potential obtained for a QD.

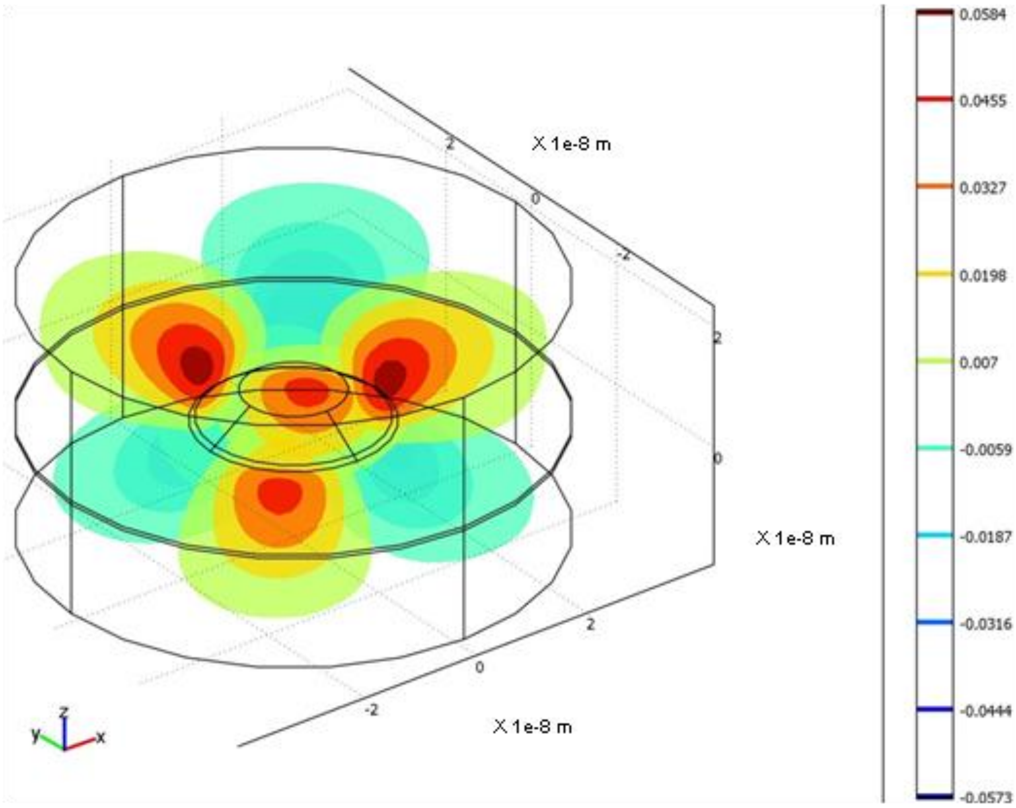

Figure 14. *Example of piezoelectric potential obtained for a InAs/GaAs QD.*

Band Structure Calculation

Step 6a: Set physical properties

Now, the physical model in-use is switched to another model with PDE corresponding to the band structure calculation. The COMSOL default PDE equation is the same as that for the piezoelectric potential calculation, as in equation (94). Depending on the Hamiltonian, the governing equation is either the one-band model (see Section 2.3) or a 8×8 matrix for the eight-band model (See Section 2.5). Again, the coefficients are set such that the PDE matches the Schrödinger equation.

Step 6b: Set boundary conditions

In this example, Dirichlet boundary conditions are employed for the particle-in-a-box situation. As for the geometry's internal boundaries, they are set to Neumann condition such that the terms in the bracket of equation (94) are continuous across an interface. These settings can also be visualised as shown in Figure 13.

Step 6c: Set solver parameters and solve problem

The band structure calculation is an eigenvalue problem; hence an eigenvalue solver is used. This calculation will require solutions from the previous two calculations as inputs. Hence, the settings for variables have to be changed accordingly, as shown in Table 5, before the calculation is performed.

Solver	Eigenvalue, Direct
Desired number of eigenvalues	Typically 30 for 8-band, and up to 1000 for one band
Search for eigenvalues around	Typically value around the center of band gap for 8-band, and at band edge for one band model.
Initial Value	Initial value expression evaluated using stored solution
Values of variables not solved for and linearization point	Stored solution
Solve for variables	Either u1-u8 (for 8-band), or u9 (for 1-band)

Table 5. *Solver and initial value settings for the band structure calculation.*

For the one-band model, there will be as many equations as the number of nodes to solve for upon assembling the entire system, i.e. the global matrix. For the eight-band Hamiltonian, there will be eight equations corresponding to each node. Therefore, the basis size is also 8 times larger.

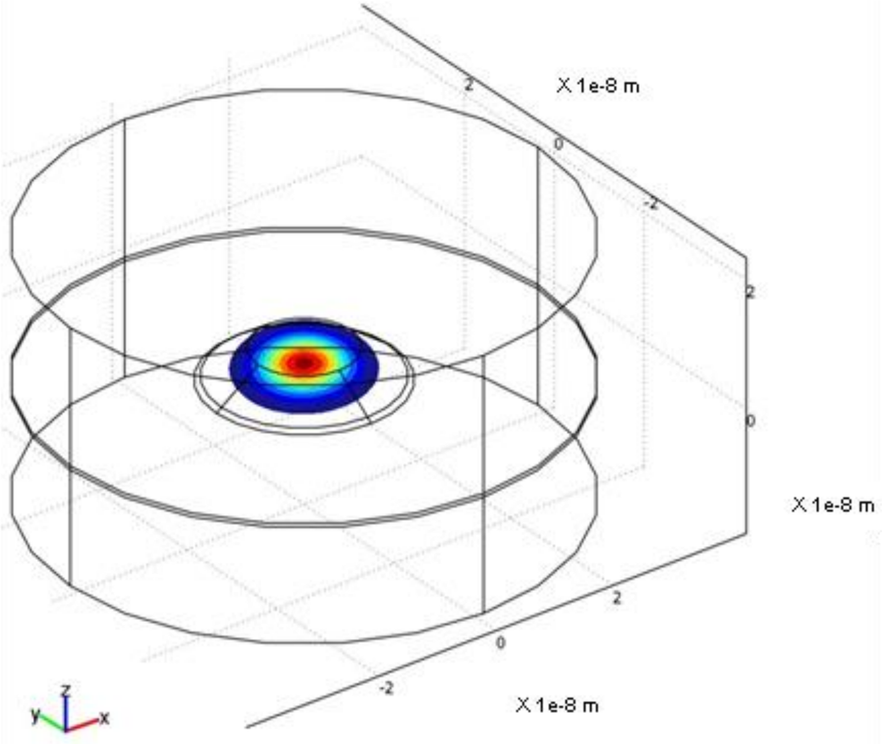

Figure 15. *Example of electron ground state wave function for a InAs/GaAs QD.*

Chapter 3

Experimental Study

3.1 Introduction

In order to verify the modelling results, a direct comparison with the experimental data is necessary. For this purpose, optical spectroscopy is used to reveal the electronic properties of the samples under study, by means of emission and absorption. Fourier Transform Infrared Spectroscopy has been employed for the optical study and the underlying principle of its operation is briefly addressed.

3.2 Photoluminescence Spectroscopy

Luminescence is an optical process which involves radiative emission from the sample by electron excitation, either electrically (i.e. electroluminescence) or optically (i.e. photoluminescence). [13] Photoluminescence (PL) is one of the most commonly used technique to obtain useful information about the energy band structure of a sample. [14] It gives information about the energy, intensity and line width of optical transition. It is a non-contact, non-destructive technique and it does not require any sample preparation. In PL, a light source (typically laser) emitting photons of higher energy than that of the band gap of the sample is required. When the light is directed onto the semiconductor device, the electrons are excited via absorption of photons. This process is known as photoexcitation. The excited electrons return to lower states and recombine with holes, after some energy loss or relaxation, by means of optical radiation or photon emission. This luminescence process, which involves photoexcitation, is called photoluminescence.

3.3 Fourier Transform Infrared Spectroscopy

Fourier Transform Infrared (FTIR) Spectroscopy [88] is a powerful and versatile analysis technique widely used in research and industry in a variety of fields. In this work, FTIR is used to produce infrared spectra from solid semiconductor samples, from which their electronic properties (e.g. transition wavelengths) are studied.

FTIR spectrometer consists of three major components: an light source, an interferometer and a detector. The interferometer is usually of the Michelson type, which consists of a fixed mirror, a movable mirror and a beam splitter (a semi-transparent mirror that ideally transmits half of the incident light and reflect the other half). A typical layout of a Michelson interferometer is shown in Figure 16. In general, the optical path in a FTIR can be described in the following:

a) The light source is collimated to the beam splitter.
b) At the beam splitter, the beam is split into two coherent beams A and B: A is reflected off towards the fixed mirror, and B is transmitted through towards the movable mirror.
c) The two beams (A and B) are reflected from the mirrors and recombined constructively or destructively (i.e. interference) at the beam splitter.
d) Finally, the light is refocused and collected by the detector.

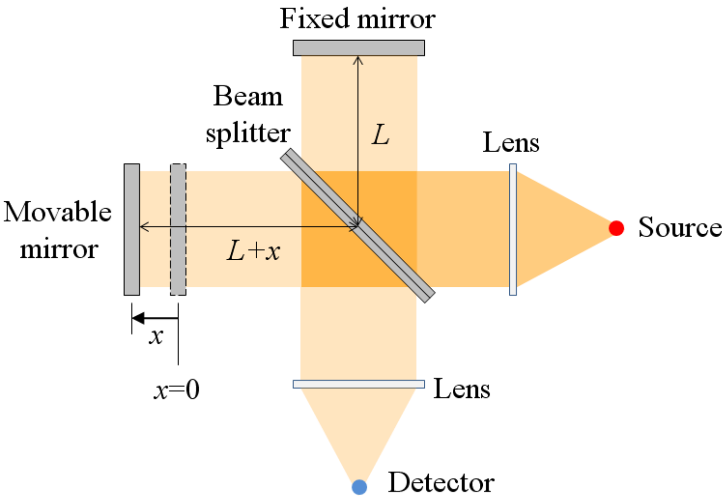

Figure 16. *Simplified layout of a typical Michelson interferometer. [88]*

For absorption measurement, the light source is a broadband infrared source and the sample is placed between the interferometer and detector. For photocurrent measurement, it is similar to absorption measurement except that the sample is the detector. In this case, it is the study of the sample's current production as a function of bias voltage. For emission (i.e. PL) measurement, a high-energy (typically red or near-infrared) laser is directed on the sample. The emitted light from the sample is then directed into the interferometer and finally being collected by the detector. (To be discussed in Section 3.4)

Principle of FTIR Operation

The heart of a FTIR operation lies in the interferometer. If both fixed and moveable mirrors are of the same distance L from the beam splitter, beams A and B would have travelled the same distance $2L$ before they recombine again at the beam splitter. In this case, they have zero path difference (ZPD). If the moveable mirror is displaced by a distance x, the two beams then have an optical path difference δ of $2x$. In this case, a phase shift (time delay) is introduced on beam B relative to beam A.

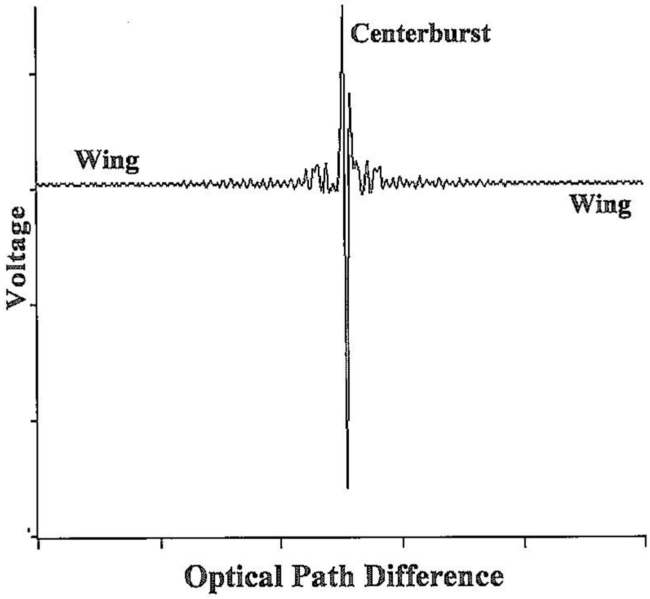

Figure 17. *Typical inteferogram of a broadband source. [88]*

When the two beams recombine at the beam splitter, interference occurs, in which the interference pattern depends on the optical path difference. By varying the position of the moveable mirror, the collected signal at the detector produces a plot of intensity as a function of the optical path difference, known as *interferogram*. The maximum peak of an interferogram (Figure 17) obtained from a broadband infrared source (known as the *centreburst*) corresponds to the position of the ZPD, where all wavelengths of light interfere constructively. For large δ, some wavelengths interfere constructively while others interfere destructively, giving rise to the smaller out wings in the interferogram.

By moving the mirror at a constant velocity v, the optical path difference can be expressed as $\delta = 2vt$. For a monochromatic source, the interferogram has the form of sinusoidal function, given by [88]

$$I(\delta) = B(\upsilon)\cos(2\pi\upsilon\delta) \tag{95}$$

$$I(t) = B(\upsilon)\cos(2\pi\upsilon 2vt) \tag{96}$$

where I is the intensity of beam, $B(\upsilon)$ is intensity of the source at wavenumber υ (where $\upsilon = {}^{1}/_{\lambda}$) as modified by the instrumental characteristics. In a FTIR spectrometer, a broadband (polychromatic) infrared source emitting light of continuous wavelengths is normally used. The interferogram is thus the superposition of all sinusoidal functions corresponding to each wavenumber υ, i.e.

$$I(t) = \int_{-\infty}^{\infty} B(\upsilon)\cos(2\pi\upsilon 2vt)\,d\upsilon\,. \tag{97}$$

This is analogous to the mathematical Fourier function expressed as a sum of sinusoidal waves. Consequently, by performing Fourier transform on the interferogram, the light spectrum can be recovered as

$$B(\upsilon) = \int_{-\infty}^{\infty} I(t)\cos(2\pi\upsilon 2vt)\,dt \tag{98}$$

In real experiments, the generation of an interferogram is digitised. In other words, the light intensity is not recorded as a function of continuous values of δ, but with discrete increments. Therefore, a discrete Fourier transform is performed by computer to recover the spectrum.

Advantages of FTIR

Before the invention of FTIR, the dispersive spectroscopy of a monochromator was commonly used to obtain infrared spectra. A monochromator spatially separate light into a spectrum by means of either diffraction (using grating) or dispersion (using prism). A narrow region of light components is selected to pass through a slit and hit the detector.

The infrared spectrum is then obtained by sequentially rotating the grating or prism for light of different wavenumber to be recorded by the detector.

The FTIR spectroscopy has two main advantages over the conventional dispersive spectroscopy: the higher signal-to-noise ratio (SNR) and shorter measurement times. The contributing factors to these advantages are summarised as below:

(1) In a dispersive spectrometer, narrow slits are required to control resolution. The FTIR spectrometer however has a large circular aperture to allow significantly higher light throughput, known as Jacquinot's advantage. This increases the light intensity reaching the detector and results in higher SNR.

(2) The FTIR spectrometer detects light of all wavenumbers at once (i.e. multiplex, also known as Fellgett's advantage), whereas the dispersive spectrometer measures only a small wavenumber range at a time. This significantly reduces the measurement time. Making use of this advantage, N multiple scans can be obtained for the same period of time and added together, known as *coadding*. In this way, the random noise can be reduced and hence the SNR is improved (proportional to $\sqrt{N}$).

In addition, the FTIR spectrometer has an internal wavelength calibration system, using a helium-neon (HeNe) laser as reference at 632.8 nm. It controls very precisely the velocity of the moveable mirror and also acts as a trigger mechanism for the sampling of signal at the detector. This permits high precision wavenumber of typically 0.01 cm^{-1}. This feature is known as Connes advantage.

Operation Modes: Rapid Scan and Step Scan

Conventionally, the moveable mirror in the interferometer moves at constant speed while the detector is triggered to register the light intensity for every small δ. This operation mode is the so called *rapid scan*, and a spectrum can be obtained within a small fraction of a second. In the *step scan* mode, however, the moveable mirror displaces to a certain position, and held there for some time. During this time, the detector records a set of signals at a fixed time interval (e.g. at 10 μs, 20 μs, and so on). Then, it moves on to a different position and repeats the data acquisition process again. Eventually, the time-resolved spectra can be obtained. If time-resolved spectra is not required (as in this work), the equi-time spaced signals at each position can then be coadded and averaged before being stored onto a PC. Consequently, the random noise can be reduced and hence the SNR is improved.

3.4 Experimental Setup

The PL experimental setup used in this work is illustrated in Figure 18, in which a FTIR spectrometer (Bruker IFS 66/s) in step-scan mode is utilised. In general, this setup requires a laser source, a cryostat, a FTIR spectrometer, an InSb detector, a PC and a lock-in-amplifier. Of course, there is more equipment needed to prepare the cryostat for low temperature measurements, including a temperature controller and a high vacuum pumping system.

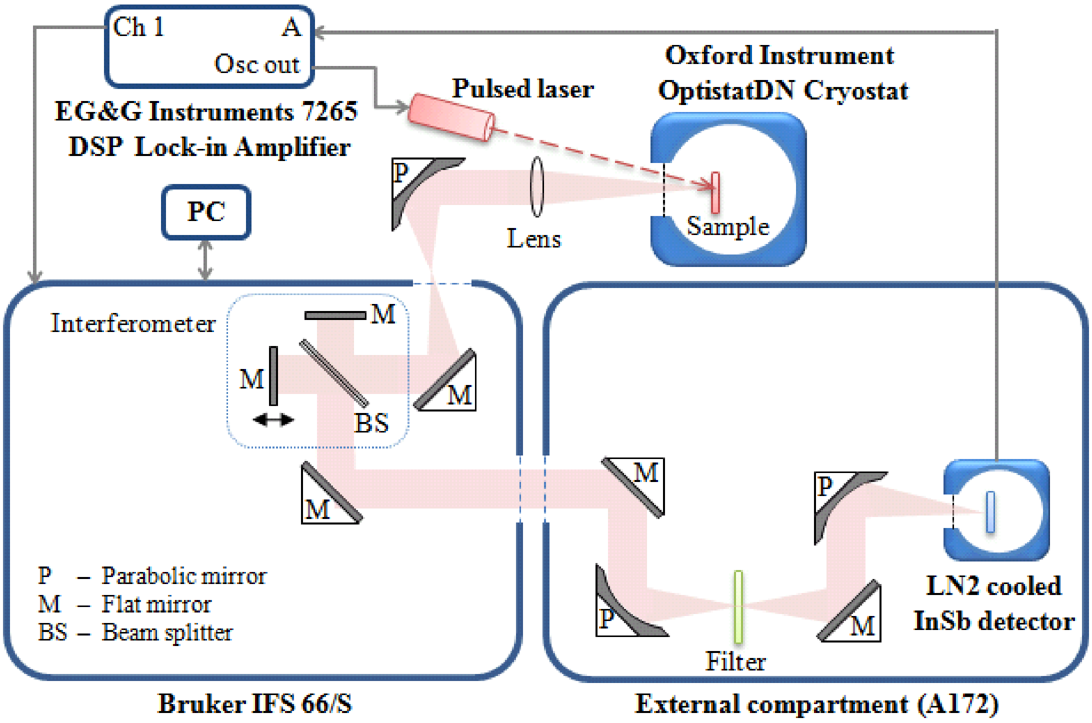

Figure 18. *Schematic of the photoluminescence experiment setup in our laboratory.*

The prepared sample is first mounted in the cryostat's sample chamber. A modulated 785nm laser is directed to the sample. The luminescence is then being collected and directed into the interferometer in the FTIR spectrometer, which comprises a KBr beam splitter. The light is then detected by a liquid-nitrogen (LN2) cooled InSb mid-infrared detector, housed in an external compartment (A172). A semi-insulating GaAs substrate is used as a filter to cut out high energy light (which is not of interest in the study) from the detector, which otherwise would saturate. The lock-in amplifier is an amplifier that can be used to measure a very small signal at a reference frequency. Essentially, it allows one to remove most of the noise from the source signal, by first modulating the source and then demodulating the detected signal at the same frequency. This technique is known as synchronous detection. In this case, the frequency at which the lock-in amplifier modulates the laser is used as reference. The interferogram is then sent to the PC. A dedicated software package, OPUS, is used not only to control all the operation of the Bruker FTIR spectrometer, but also to perform Fourier transform automatically on the interferogram to yield the spectrum. In addition, it offers extensive spectral processing functions such as the spectrum calculator (e.g. integration and subtraction), absorbance-transmission conversion, automatic baseline correction, etc.

For low temperature measurements, the cryostat has to be evacuated to create a high vacuum condition (in the order of 10^{-6} Torr) using a combination of rotary and turbo pumps. Helium gas is then injected into the sample chamber as heat exchange medium. LN2 from the integrated reservoir flows through capillary tubes surrounding the sample chamber, and cools the sample by conduction through heat exchange helium gas in the chamber. Temperature control is achieved by a combination of manual nitrogen flow control at the exhaust line of LN2 reservoir and power dissipated in an integrated electrical heater, regulated using an ITC temperature controller. This allows temperature-dependent measurement between 77 K (boiling point of LN2) to 300 K (room temperature).

Chapter 4

InAs/GaSb Short-period Superlattices

4.1 Introduction

InAs/GaSb superlattices (SL) have a type-II “broken gap” band alignment, where the conduction band minimum in InAs is below the valence band maximum in GaSb. (See Figure 3c in Section 1.1.2) This type of heterostructure is particularly important due to the expected suppression of non-radiative Auger recombination in such designs. [89] By tailoring the superlattice period, this antimonide-based system provides great potential for optical devices in a wide wavelength range, including the technologically useful 3-5 μm mid-infrared atmospheric window. InAs/GaSb short-period superlattices (SPSLs) with a period of 4-12 monolayers (MLs) have recently attracted a lot of interest because they have optical transitions in this wavelength region. Indeed, promising results have been reported for InAs/GaSb SPSLs operating within the 3-5 μm range. [90,91,92]

The use of these SL structure for lasers and photodetectors depends not only on the successful growth of the periodic structures but also on the accurate design of their band gaps. The $\boldsymbol{k}\cdot\boldsymbol{p}$ method within the envelope-function approximation has been widely used in calculations of the electronic spectra for semiconductor nanostructures. Its simple input requirements (such as dimension, orientation and basic parameters from bulk materials) have made it so popular that it is termed as the “standard method”. [49,93] It has been successfully used in modelling of quantum wells and superlattices, especially of the electronic states close to the Γ-point of the Brillouin zone.

However, this method has not been successful for InAs/GaSb SPSLs. [15,94] Instead, it was found to overestimate the fundamental energy gap between the electron and heavy-hole minibands by as much as 60 meV. [49,51] Apart from fundamental limitations of the $\boldsymbol{k}\cdot\boldsymbol{p}$ method (such as assumption of equal Bloch functions in InAs and GaSb), many authors have suggested that this is due to the lack of a common atom at the interfaces between the two materials. [15,94] Indeed, the two interfaces (GaSb-on-InAs and InAs-on-GaSb) have chemically distinct bonds: the former has Ga-Sb and In-Sb bonds, while the latter has In-As and Ga-As bonds.

Since the standard $\boldsymbol{k} \cdot \boldsymbol{p}$ method did not provide accurate results, the atomistic calculations such as the pseudopotential method, were suggested as the only viable alternative. [15,94] However, the amount of calculation involved is massive and the size of the structure is limited. Simultaneously, some modifications to the $\boldsymbol{k} \cdot \boldsymbol{p}$ method were proposed. In some publications, a delta-like potential at the interface was suggested, to account for the effect of the extra In-Sb and Ga-As chemical bonding. [95] The results were in better agreement with experimental data, even within a single-band model. [91,95] However, it was achieved at the cost of using an additional fitting parameter which does not have a real physical meaning.

4.2 The InAs/GaSb Interface

Other than the lack of a common atom, another important issue for the physical structure of InAs/GaSb interfaces is the effect of segregation, in particular that of antimony. Previous studies [94] have demonstrated that these SLs are known to have interfaces that are not always abrupt, but show some tendency of both the anion and cation to intermix. Interface roughness and layer composition profiles are difficult to control due to the exchange reaction between As and Sb during growth. [96,97] Segregation of Sb largely contributes to degradation of the interfacial abruptness and to formation of asymmetrical interfaces. [15,94,96] For large period superlattices, the effect of the interface disorder may be relatively small. Indeed, the overestimation of the energy gap by the $\boldsymbol{k} \cdot \boldsymbol{p}$ method reduces with increasing the number of periods. [49] However, for short-period superlattices, modifications of the band profile around the interfaces can have a deleterious effect on the band structure. This leads to a suggestion that the overestimate may be due to modification of the interface band profile caused by segregation.

The interface composition profile is strongly affected by the growth conditions, which are different between samples even for two nominally identical structures. Therefore, to take segregation into account, it is necessary to identify the profile parameters which are common for real heterostructures grown under typical conditions. Experimental studies of the interface profile in the InAs/GaSb superlattices have been performed using scanning tunnelling microscopy (STM) [94,98] and transmission electron microscopy (TEM). [96,97] They have revealed that the interface disorder has two major components, the interface roughness (uneven surface due to formation of steps) and the interfacial diffusiveness (intermixing due to stochastic processes and exchange reactions). [96,97]

From these reports, it follows that there is an identifiable common parameter, which is the *graded interface* with a thickness of 2-6 MLs.

Next, the dominant interface-disorder mechanisms for the two interfaces (GaSb-on-InAs and InAs-on-GaSb) are different, resulting in the different physical structure. Antimonides have a lower binding energy than arsenides [96], so Sb atoms are more diffusive. Because of this, exchange reactions tend to occur more for arsenides (in this case, InAs) grown on antimonides (GaSb), reducing the surface energy during growth. In particular, strong segregation of Sb has been observed in the case of InAs grown on GaSb, e.g. by as much as 25% Sb and for up to 6 MLs into the InAs layer. [94,96,98] Moreover, about 5% of Sb has been reported even beyond 6 MLs into InAs. [94,98] For GaSb grown on InAs, although minor exchange still occurs, the graded interface is mainly due to interface roughness, with an average interface region thickness of up to 2 MLs dependent on growth conditions. This leads to *physical asymmetry* in the composition profiles between the two interfaces. Such asymmetry has been observed using both STM and TEM techniques, and is supported by modelling. [94,98] Figure 19 shows a STM-measured composition profile for a InAs/GaSb SPSL, where the asymmetry interface was clearly visible. [94]

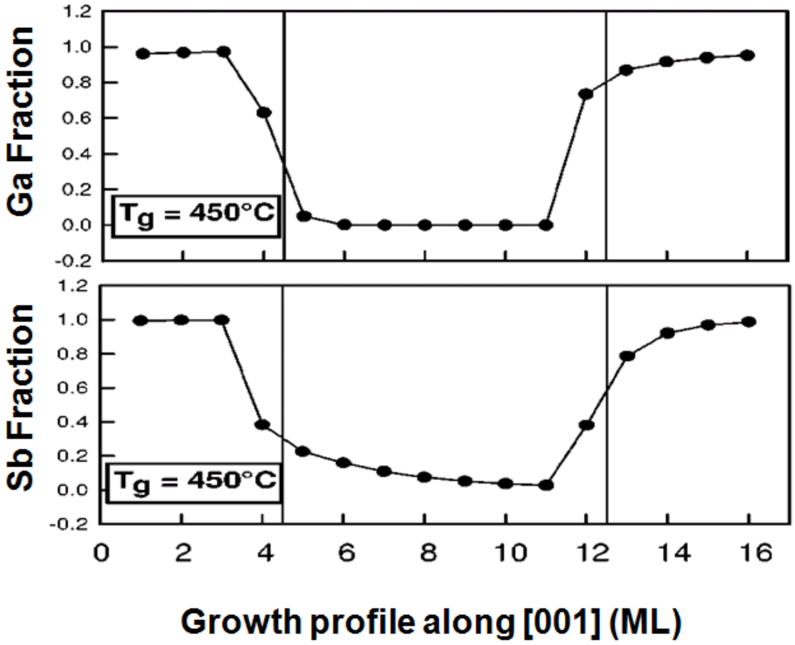

Figure 19. *Sb- and Ga-fraction measured by STM for a symmetric InAs/GaSb SPSL grown at 450 ℃, nominally 8 MLs in each layer. [Taken from reference 94]*

4.3 Simplified Interface Profile for Modelling

Based on the properties of the InAs/GaSb interface, as discussed in Section 4.2, a simplified segregated composition profile was constructed. This is illustrated in Figure 20. This corresponds to the profile of SPSLs studied by STM and reported in reference 94 for a growth temperature of 450 °C, as shown in Figure 19. The interface layer comprises 2 MLs of material with graded composition, with one monolayer taken from the InAs and the other from GaSb. Strictly speaking, this material is a quaternary $Ga_xIn_{1-x}As_ySb_{1-y}$, in which x and y may be independent. However, for simplicity the GaSb-lattice-matched alloy compound of $(InAs_{0.91}Sb_{0.09})_x(GaSb)_{1-x}$ is used instead, for which the band parameters are well known. [72] Also, for a very short superlattice period with a nominal thickness of the InAs layer up to 5 MLs, the ternary compound $InAs_{0.91}Sb_{0.09}$ is used in place of pure InAs. This simulates the effect of strong Sb segregation into the InAs layer. As illustrated in Figure 20, the Sb fraction is always non-zero in this case.

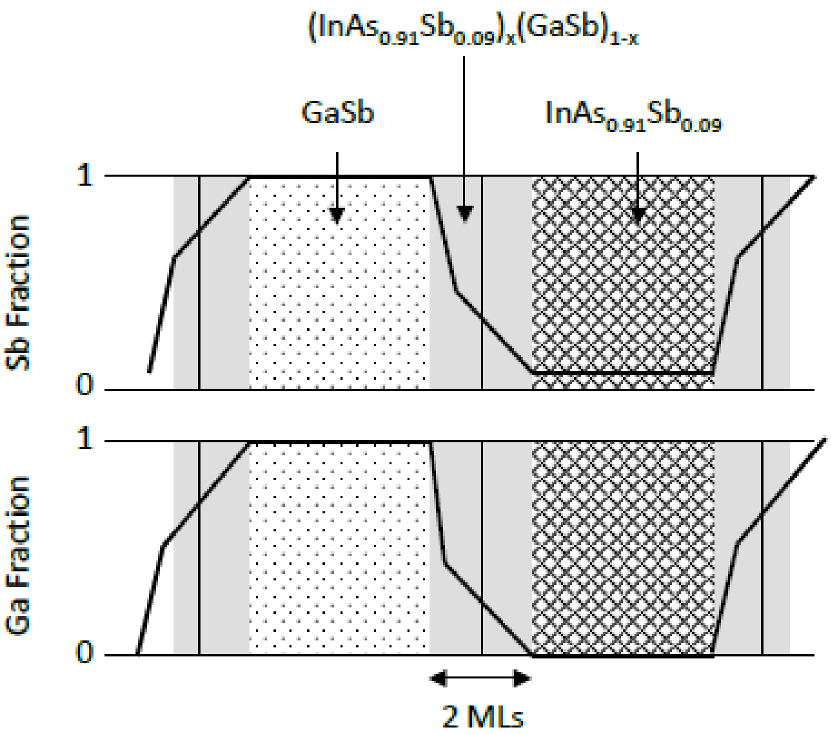

Figure 20. *Schematic of segregated composition profile for the GaSb/InAs interface employed in the model. A ternary* $InAs_{0.91}Sb_{0.09}$ *compound is used instead of the nominal InAs layer.*

4.4 Methods

For all the calculations, the Finite Element Method (FEM) was employed, using a COMSOL Multiphysics commercial package. [18,99] First, the strain tensors were calculated within the continuum-elasticity approximation using elastic constants from reference 73. Next, the electronic structure was modelled using the standard eight-band strain-dependent $\boldsymbol{k} \cdot \boldsymbol{p}$ Hamiltonian (see Section 2.5). All band parameters are taken from reference 72.

The effect of dominant interface bonding type is not included in our model, because for a graded interface, it is much less relevant than it would be for an abrupt interface. Nor is the exciton binding energy taken into account in the calculations because it is small. This is justified by the report in reference 100, where an exciton binding energy of 0.9 meV was estimated for a 3.0/5.0 nm InAs/GaSb superlattice.

Photoluminescence (PL) spectra were recorded at 10 K using Fourier-Transform Infrared Spectroscopy in the step scan mode. The spectra were excited at 800 nm using a continuous-wave Ti:Sapphire laser and collected by a liquid-nitrogen-cooled InSb photodetector. The excitation power density was about 5 W/cm^2. The experiments were performed by Dr Romuald Intartaglia at the National Nanotechnology Laboratory in Lecce, Italy.

In this work, only the short-period superlattices with layer thicknesses within the range of 4-8 MLs were studied. This is because the effect of the graded interface on the band energies is much more significant for short-period than for long-period structures. Two samples of asymmetric InAs/GaSb SPSLs were grown by molecular-beam epitaxy at a temperature of 420 °C on a GaSb substrate. The nominal thickness of the InAs/GaSb layers was 1.0/1.7 nm (sample A) and 0.9/2.0 nm (sample B), respectively. These samples were supplied by Professor Eric Tournié (Université Montpellier 2, France).

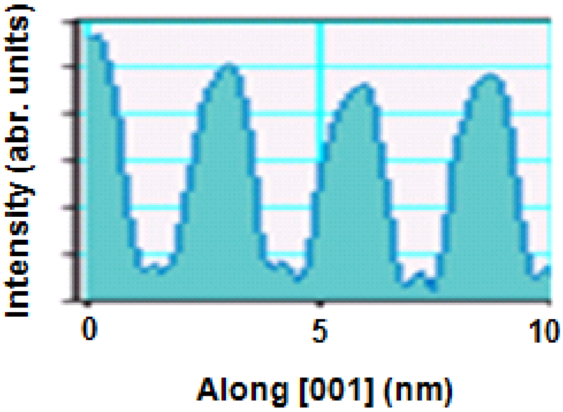

Figure 21. *Contrast profile obtained from TEM image of sample B showing an asymmetric profile similar to that reported in the literature [94,98] (e.g. Figure 19).*

A study of the contrast variation from a TEM image for sample B, performed by Dr Luna Esperanza (from Paul-Drude-Institute, Germany) is shown in Figure 21, in which the intensity corresponds roughly to the compositional change along growth direction. Although it is not straightforward to extract the composition profile by studying the contrast of a TEM image, the contrast profile shows similar graded and asymmetric interface profile as described in the earlier section.

4.5 Results

The electronic structure of the InAs/GaSb SPSLs was modelled using the segregated composition profile described in Section 4.3. An example of such profile used in the modelling is shown in Figure 22. Calculations were performed for both asymmetric and symmetric SPSLs. Results for asymmetric structures were compared to our experimental spectra. For symmetric structures, the results were compared to the experimental data in the literature. [91,92,101,102] For comparison purposes, calculations assuming perfectly abrupt interfaces were also performed.

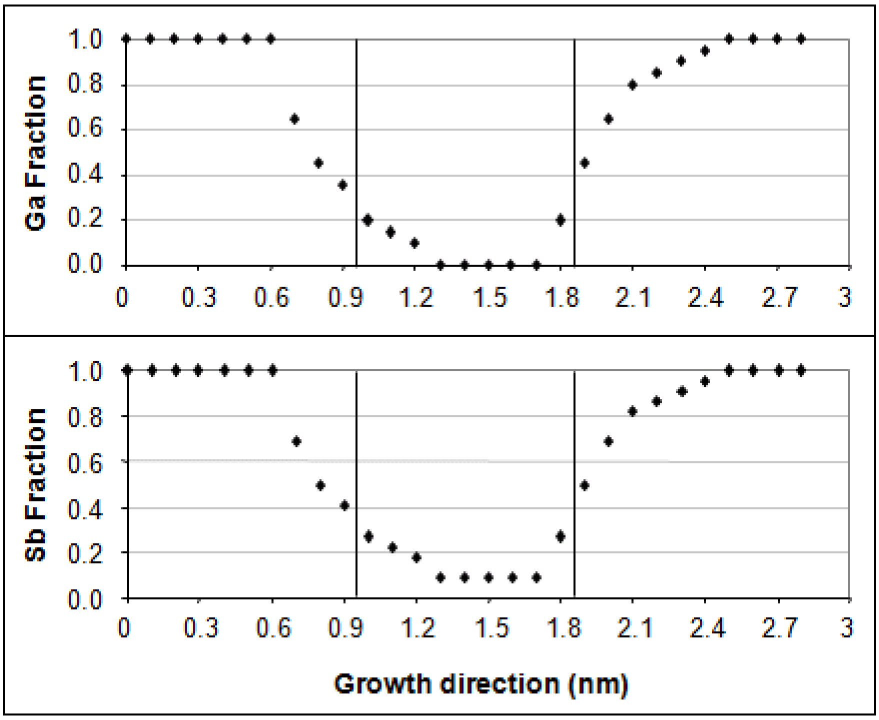

Figure 22. *Compositional profile for sample B used in the model.*

4.5.1 Asymmetric SPSLs

Figure 23 shows normalized PL spectra obtained from the studied samples. The spectra show the peaks due to transitions between the electron and hole minibands at 0.415 eV and 0.440 eV for the two samples. Dashed arrows show calculated energy gaps assuming perfectly abrupt interfaces. One can see that in this case, the transition energies are hugely overestimated, by 50-60 meV. Agreement between the modelling results and experimental data is significantly improved if segregation is taken into account. The modelled transition energies in this case are shown by solid lines. The calculated energy gap is reduced by 30-35 meV, with the discrepancy decreasing almost threefold. Still, some overestimate remains, probably because the real composition profile of the samples deviates from the one used for calculations. Also, the effect of Stokes shift (due to carrier thermalisation), which causes a red-shift in the emission peak as oppose to the absorption peak, may contribute to the discrepancy. However, there is no obvious change in shape on the high energy slope, suggesting that the effect may be insignificant. [103]

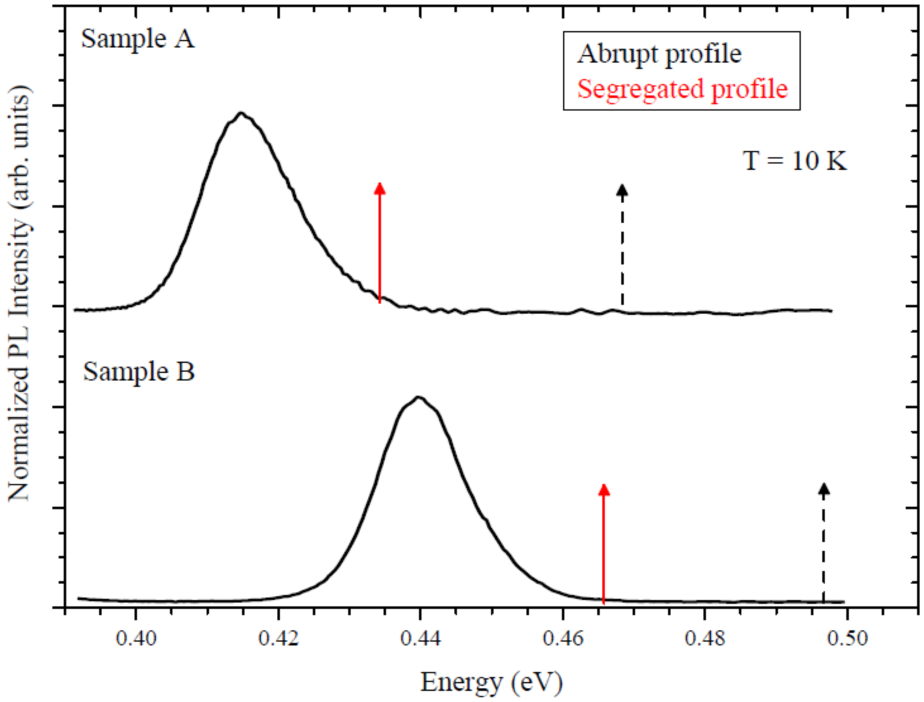

Figure 23. *PL spectra from asymmetric InAs/GaSb SPSLs. Samples A and B have InAs/GaSb layer thicknesses of 1.0/1.7 nm and 0.9/2.0 nm, respectively. The spectra are offset for clarity. Arrows indicate the calculated energy gap values: black dashed lines for abrupt interfaces and red solid lines for graded interfaces.*

4.5.2 Symmetric SPSLs

Data for symmetric structures are shown in Figure 24. The symbols show the experimental data from the literature. [91,92,101,102] One can see that there is a scatter for samples even with the same nominal structure, which is due to different growth conditions and resulting interface parameters. The calculations were performed using band parameters at 80 K, for better comparison with the experimental data. Note that experimental data measured at 4 K is also included in comparison because the difference between 4 K and 80 K is not too significant (band gap changes by ~ 10 meV for both materials) as compared to the difference between two sample sets of identical structures. Modelling results using graded interfaces are shown by the solid line; the dashed line shows results for the abrupt interface. For the standard method (with abrupt interface), the transition energies are overestimated by 20-60 meV. With the segregated composition profile, the modelled transition energies decrease by 20-70 meV; the decrease is greater for shorter superlattice periods since the effect of interface condition is more significant for thinner structure. With effect of interfacial segregation taken into account, our modelling demonstrates excellent agreement with the experimental data.

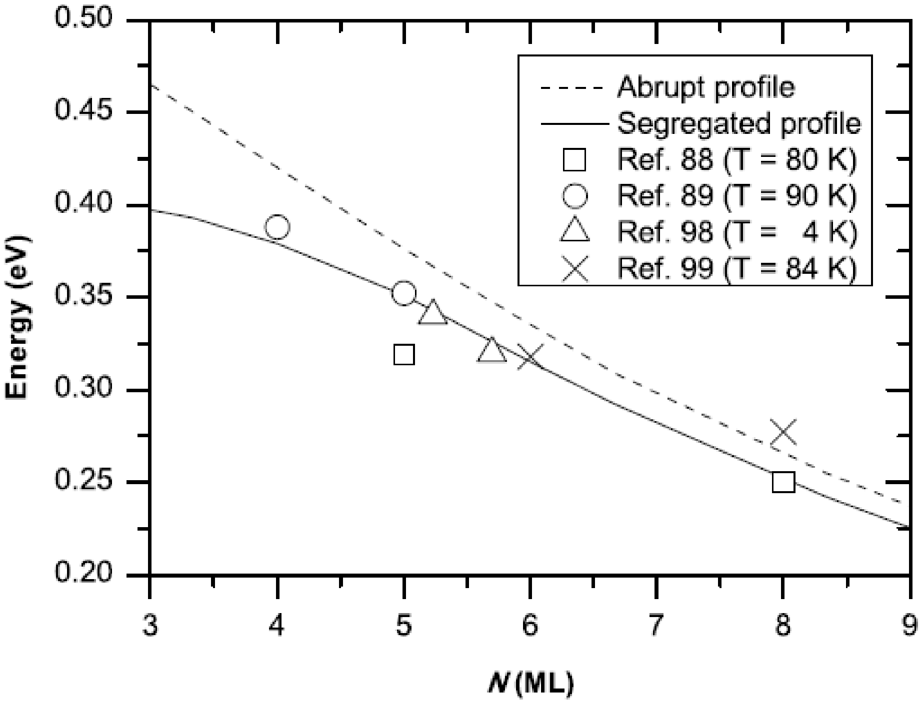

Figure 24. *Fundamental energy gap for symmetric* $(InAs)_N/(GaSb)_N$ *SPSLs. Lines show the calculation results; symbols represent the experimental data from the literature; N is the number of monolayers in the SPSL samples.*

4.6 Discussion

To reveal the physical mechanism by which the graded composition profile affects the optical transition energy, its effect on the band profile needs to be considered. Figure 25 shows the band profile of the conduction band and the heavy-hole and light-hole valence bands for abrupt and segregated interfaces.

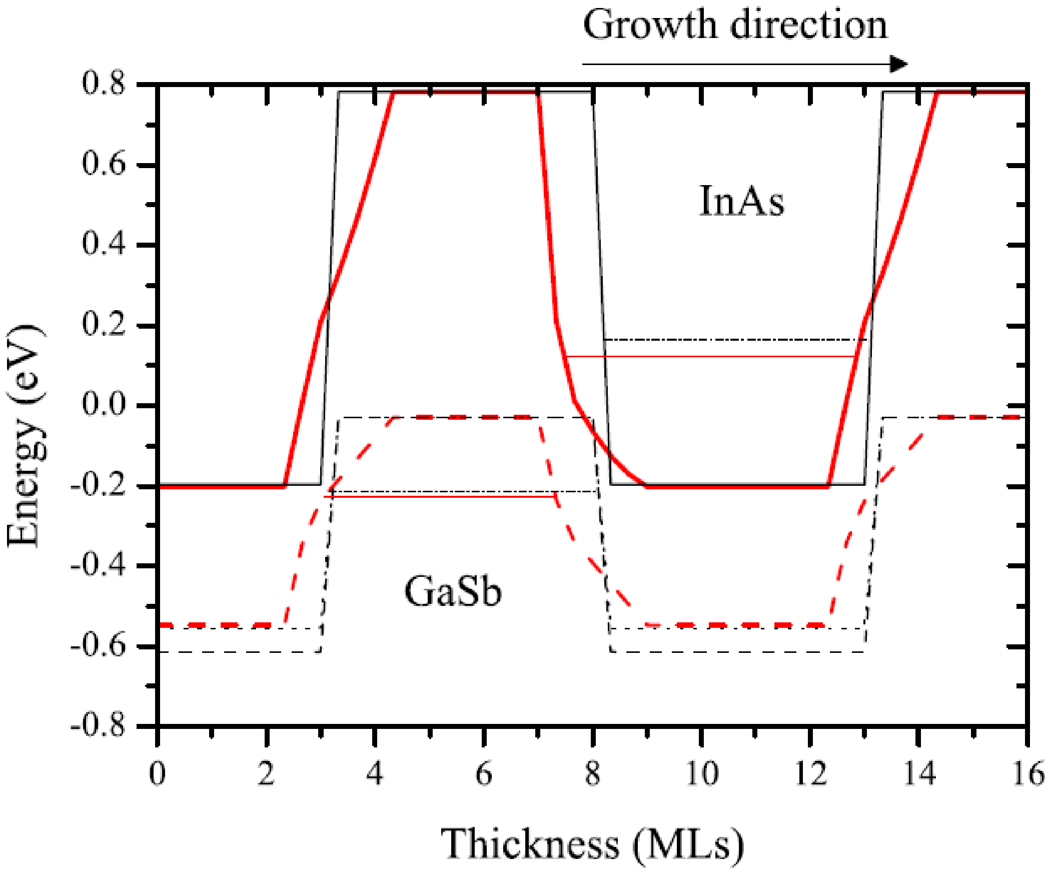

Figure 25. *Band profiles for abrupt and segregated interfaces (black fine and red bold lines, respectively). Conduction band, light-hole and heavy-hole valence bands are represented by the solid, dashed and dotted lines, respectively. The ground electron and heavy-hole energy levels are shown for both segregated and abrupt profiles using solid (red) and dash-dotted (black) lines, respectively.*

One can see that for the graded interface, the quantum well profile for electrons is wider than for abrupt interfaces. This is a direct consequence of the *physical asymmetry* in the composition profile at the interfaces due to different dominating interface-disorder mechanisms for GaSb-on-InAs and InAs-on-GaSb (as discussed in Section 4.2). This results in a decrease in the size-quantization energy for the electron miniband by up to 70 meV.

Similarly, the quantum well profile for holes in the graded structure is narrower. However, the increase in size-quantization energy, which might be expected in this case, is counteracted by a reduction in the height of the barrier formed by the InAs layer. The calculations show that the overall effect of segregation on the heavy-hole miniband is minor (less than 10 meV).

As a result of these combined effects from the electron and hole confinement in the graded and asymmetric quantum wells, the optical transition energy is reduced by as much as 60 meV, resulting in much better agreement with the experimental data.

4.7 Summary

In this work, the physical origin of the failure of the standard $\boldsymbol{k} \cdot \boldsymbol{p}$ method to model the electronic structure for InAs/GaSb short-period superlattices has been investigated. The calculations have shown that the *asymmetric* interfacial segregation results in a significant reduction in the size-quantization energy for the electron miniband, leading to a reduction in the fundamental energy gap. Using a simplified segregated composition profile, which is based on *experimental evidence*, results in much better agreement with the experimental data were obtained. It has been demonstrated that the $\boldsymbol{k} \cdot \boldsymbol{p}$ method can be used for InAs/GaSb SPSLs with a good predictive ability, as long as the real physical structure of the interface is correctly taken into account.

Chapter 5

Quantum Dot-in-Well Structures

5.1 Introduction

Quantum dot infrared photodetectors (QDIPs) have attracted much interest in recent years [37,104,105,106] in an attempt to overcome the limitations of low band gap (i.e. HgCdTe) and quantum well (QW) detectors. Due to three-dimensional (3D) carrier confinement in the quantum dot (QD), both sensitivity to normal-incidence radiation and low dark current are expected. Quantum-dot-in-well (DWELL) structures offer additional advantages, such as better control over operation spectral range and gain. Indeed, while the photodetector absorption range is quite limited for InGaAs/GaAs QD system, the use of DWELL structures allows coverage of the 3-12 μm spectral region. [106] The DWELL devices typically rely on transitions between the bound states in the dots and subbands in the surrounding QWs.

DWELL systems present a challenge for modelling of the electronic structure as they combine discrete levels in zero-dimensional QDs and continuous energy spectra in two-dimensional (2D) QWs. The Green's function method, which is often used for such problems [16,17], has very high computational cost. Here, a simplified approach is used, by simulating the quasi-continuum 2D band structure in a QW with discrete levels in a large 3D 'quantum box'. For that purpose, the Finite Elements Method (FEM) within the effective-mass approximation has been employed. The comparison with experimental data from a DWELL structure has confirmed the trustworthiness of our approach. Moreover, composition of the InGaAs/GaAs was determined, which is not readily available from other methods, such as transmission electron microscopy (TEM) [107,108], or cross-section scanning tunnelling microscopy (X-STM) [109,110]. Finally, the low computational cost of our approach allows the investigation of the modifications in the intraband absorption spectra for a wide range of compositions and shapes of InGaAs/GaAs QDs. Furthermore, the proposed approach allows routine modelling and provides an effective predictive tool for advanced design of multispectral DWELL photodetectors, and other possible DWELL-based devices.

5.2 Methods

Depending on growth and capping conditions, quantum dots can have various shapes, which may or may not possess axial symmetry (e.g. a cone or a pyramid, respectively). [25,26] In order to maintain a consistent approach for all possible dot shapes, we performed all calculations using 3D geometry. In this case, the FEM allows straightforward simulation for virtually any realistic 3D geometry of a quantum dot. In addition, it provides a good platform for including further effects like composition variations induced by cation interdiffusion or/and indium segregation processes. [107,108,109,110]

The QW was approximated with a large flat quantum box, in which a QD is placed. The strain tensors were calculated in the continuum-elasticity approximation. (See Section 2.2.1) From that, the strain-modified band profile was determined using the standard deformation potential theory. (See Section 2.2.2) The piezoelectric effect was included to first order approximation. The electron energy spectrum and wave functions were computed by solving directly the 3D single-band effective mass problem (see Section 2.4) using the Dirichlet boundary conditions (i.e. Ψ=0) at the edge of the geometry. From this, the optical transitions between the ground and the excited states in the DWELL structure were modelled. (Note that we assumed that only the ground state is occupied. [106,111]) For a quantum dot ensemble, there is a variation in the dot parameters, such as size and composition. By taking into account of this inhomogeneous broadening of dot parameters, the intraband absorption spectra of a QD ensemble can be simulated by superimposing Gaussian broadening on the calculated transitions.

In addition to the intraband transitions, modelling of the interband transitions was also needed. Even if QDs are grown by deposition of the binary InAs compound, they are usually composed of a ternary InGaAs alloy due to interdiffusion and segregation processes. [107,108,109,110] The alloying cannot be neglected since it significantly modifies the band profile and hence the electronic spectrum of the DWELL device. Therefore, the dot composition needs to be estimated prior to modelling the intraband spectra. For this, the interband optical transition energies for a range of QD compositions were calculated using the dot dimensions determined by conventional TEM measurement. For model simplicity, homogeneous composition and abrupt interfaces between the dot, the well and the barrier were assumed. The standard strain-dependent 8-band $\boldsymbol{k} \cdot \boldsymbol{p}$ Hamiltonian (see Section 2.5) was used, with exciton binding energy (see Section 2.6) taken into account. The modelling results were compared to the experimental photoluminescence (PL) spectra, from which the composition was obtained. All material parameters for modelling were taken from reference 72.

An InAs/GaAs/AlGaAs DWELL structure grown by MBE was investigated. It corresponds to the active layers of the infrared photodetector examined in reference 113. This sample was grown by our collaborator Dr Maxime Hugues from University of Sheffield (now at CRHEA-CNRS, France). Figure 26 shows the schematic diagram of the DWELL structure grown.

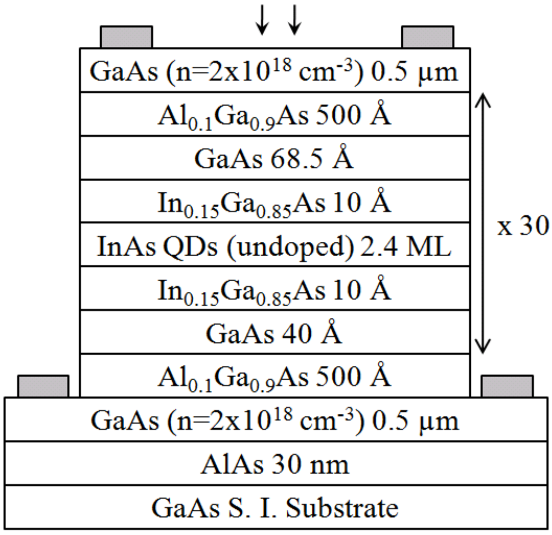

Figure 26. *Schematic diagram of the DWELL structure.*

The nominally undoped InAs QDs are embedded asymmetrically (spatially along growth direction) in a GaAs well, and surrounded by thick $Al_{0.1}Ga_{0.9}As$ barriers. A thin layer of $In_{0.15}Ga_{0.85}As$ is grown prior and after the QD growth, acting as strain-reducing layer (SRL). The latter allows repetitive growth of multiple QD active regions without defects. The n-doped GaAs contact layers provide ohmic contacts for photocurrent measurement. The conduction band profile of the active region in the growth direction through the centre of the QD under an applied electric field is shown in Figure 27.

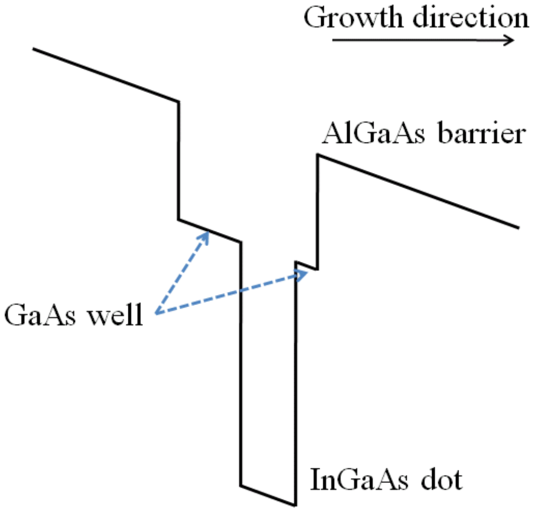

Figure 27. *Schematic diagram of the conduction band profile in the growth direction through the centre of the QD under an applied bias.*

The geometrical parameters of the QDs were determined from dark field TEM image (Figure 28, characterised by Dr Richard Beanland from Integrity Scientific Ltd.). The dots appear to have truncated geometry with average height of 7 nm, apex width of 20 nm and base width of 30 nm. The dot density is 2.5×10^{10} cm^{-2}, which corresponds to a lateral separation of roughly 65 nm between the dot centres. Therefore, interaction between the neighbouring dots is negligible, and modelling an isolated QD is a good approximation.

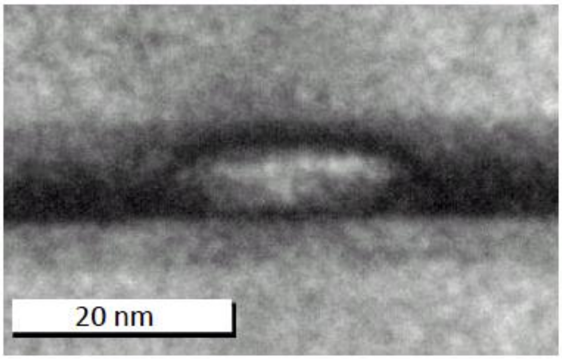

Figure 28. *Representative TEM image, from which the dot geometrical parameters were obtained.*

From the TEM image, definite conclusion cannot be made whether the QD has a truncated conical or truncated pyramidal shape; indeed, it may be anything between the two. Hence modelling was performed for both shapes. Figure 29 shows schematically the structure geometry used for the model. The QD base is positioned in the middle of the thin $In_{0.15}Ga_{0.85}As$ SRL. Since the wetting layer parameters are quite difficult to determine [114,115], and because it actually coincides with the SRL, it is not taken into account. The dot is positioned asymmetrically in the GaAs well, which is expected from the design and is clearly visible in the TEM image. There is no SRL capped directly over the QD, because it is very thin.

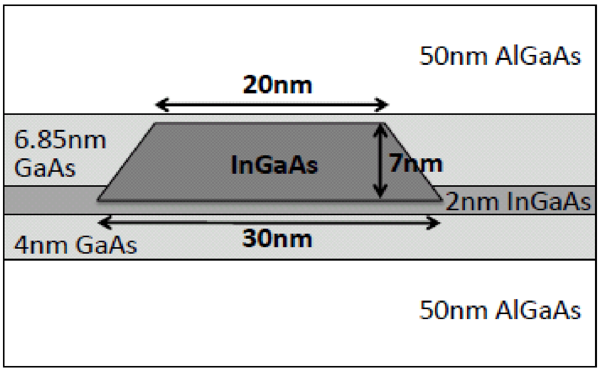

Figure 29. *Schematic of the structure geometry used, based on the TEM image.*

Performed by Mr Peter Vines from University of Sheffield, photocurrent was measured at 77 K using a Varian 7000 Fourier transform infrared (FTIR) spectrometer. The interferogram signal was amplified using a Stanford Research SR 570 low noise current preamplifier and then processed using a PC software package. Bias voltages were applied to the devices using the preamplifier voltage source and a Faraday-shielded biasing box consisting of commercial 9V cells.

Photoluminescence (PL) spectra were recorded at 77 K using Fourier-transform infrared spectroscopy in the step-scan mode. The spectra were excited using a 785 nm modulated diode laser, with the excitation power density up to 2 W/cm^2, and collected by a liquid-nitrogen-cooled InSb photodetector. (See Section 3.2) This experiment was performed by Dr S. I. Rybchenko in Hull.

5.3 Results and Discussions

5.3.1 Estimate of QD Composition

Figure 30 shows the experimental PL spectra from the sample at two excitation levels. The spectra show a distinct peak at 1.06 eV and a shoulder at ≈ 1.115 eV. The peak corresponds to a transition between the ground states of electrons and holes in the dot, while the shoulder corresponds to a transition between their first excited states.

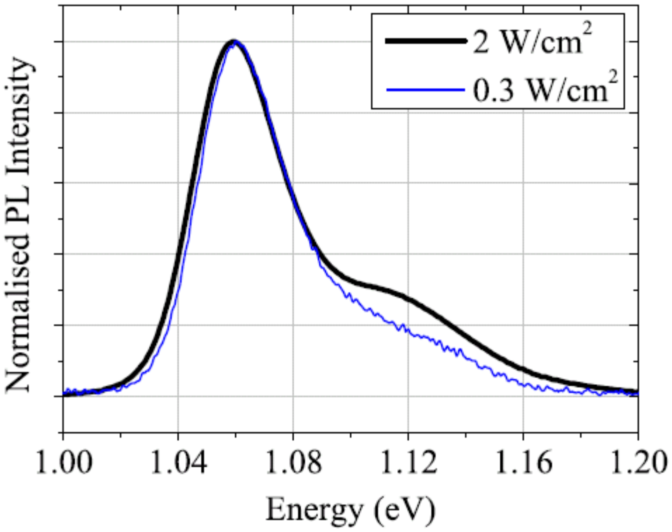

Figure 30. *Experimental PL spectra at 77 K for two excitation powers.*

In order to deduce the dot composition from the PL spectra, the optical interband transitions for the DWELL structures were modelled for a range of compositions. Figure 31 shows the calculated interband transition energies as a function of the composition for two QD shapes, a truncated cone (TC) and a truncated pyramid (TP). [110,116] The calculations show that the transition energy is dramatically affected by the composition, while the effect of the shape is relatively minor. The transition energies show that the dot composition is far from nominal pure InAs. Regardless of the shape, we can conclude that the average Ga content in the dot is 25-27 %. The simulated energy separation between the ground- and first-excited-state transitions (T1 and T2, respectively) agrees with the PL data (within the experimental and modelling errors) for both dot geometries, though the agreement is slightly better for the TC shape. The average Ga content determined is in the same range as the values deduced from complex structural characterisations reported in the literature. [110,116,117]

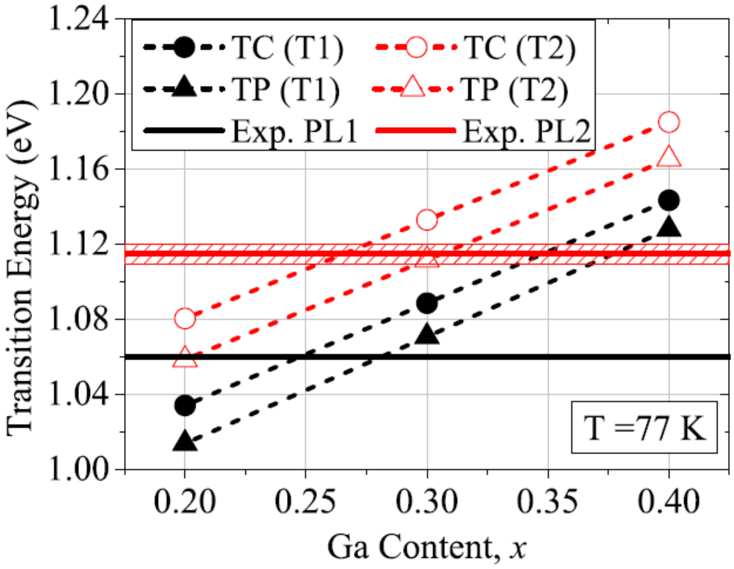

Figure 31. *Calculated transition energies for* $In_{1-x}Ga_xAs$ *QDs as a function of Ga content, x, at 77 K. Solid lines show the energies of the experimental PL transitions.*

5.3.2 Modelling of Intraband Transitions

Using the previously estimated QD geometry and composition, the DWELL intraband transitions were investigated. To begin with, the modelling results for $In_{0.75}Ga_{0.25}As$ QD of truncated conical shape were considered and analysed in details. Figure 32 shows the DWELL band diagram along the growth direction (bold solid line) with the calculated energy levels (thin horizontal lines). The ground state energy of the system is used as reference zero level. The bending of the conduction band is due to the effect of strain.

From the diagram, we can identify four energy ranges corresponding to different types of intraband transitions, all of which originate from the ground state. In the range below 0.20 eV, the transitions are to the excited states in the dot (QD → QD). The range of 0.20-0.26 eV corresponds to transitions to the 1st subband in the QW (QD → QW1). In the range of 0.26-0.31 eV, transitions both to the 1st and 2nd subbands in the QW overlap (QD → QW2). Transitions with energy above 0.31 eV correspond to transitions to the continuum above the QW barriers (QD → C). The effect of the ultra thin SRL on the energy structure is minor.

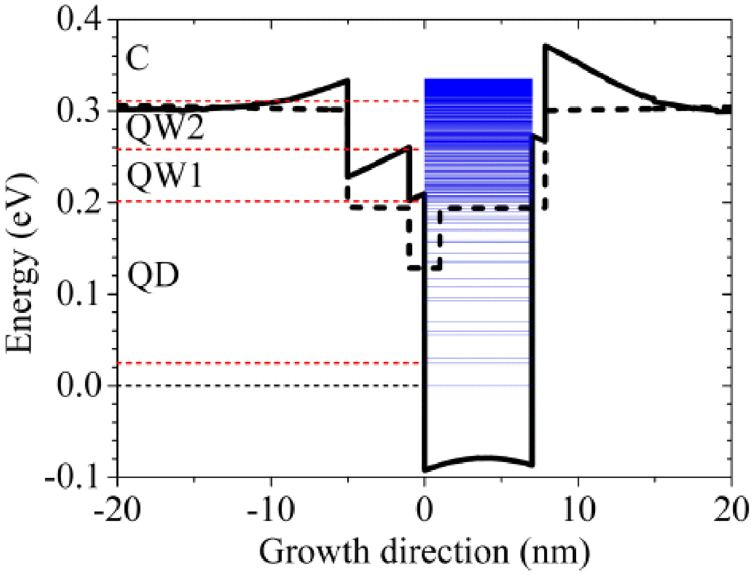

Figure 32. *Strained conduction band profile in the growth direction through the centre of a truncated conical* $In_{0.75}Ga_{0.25}As$ *QD (bold solid line; the bold dashed line shows the profile away from the QD). Thin horizontal lines show the calculated energy levels; the dotted lines on the left separate the four spectral regions corresponding to different types of transitions. The energy reference is the ground state of the DWELL structure.*

5.3.3 Simulation of Absorption Spectra

Using the energy level structure in Figure 32, the intraband transitions can be calculated. They are shown in Figure 33 as drop lines, positions and heights of which correspond to the energies and matrix elements of the transitions. The bold line represents simulated spectra with superimposed Gaussian broadening of 10 meV full width at half maximum (FWHM) to account for the effect of variations in dot parameters. The spectra are shown in logarithmic scale. The in-plane polarized spectra, Figure 33a, are dominated by low-energy peaks at about 0.03 eV, 0.10 eV and 0.18 eV, which correspond to the QD → QD transitions. In the QW2 energy range, absorption is larger than in the QW1 range because transitions to the two QW subbands are superimposed. Note that neither of these transitions would be observed in a QW structure because of the selection rules. The selection rules are broken in the DWELL structure due to carrier confinement in the QDs, leading to sensitivity to the normal-incidence radiation.

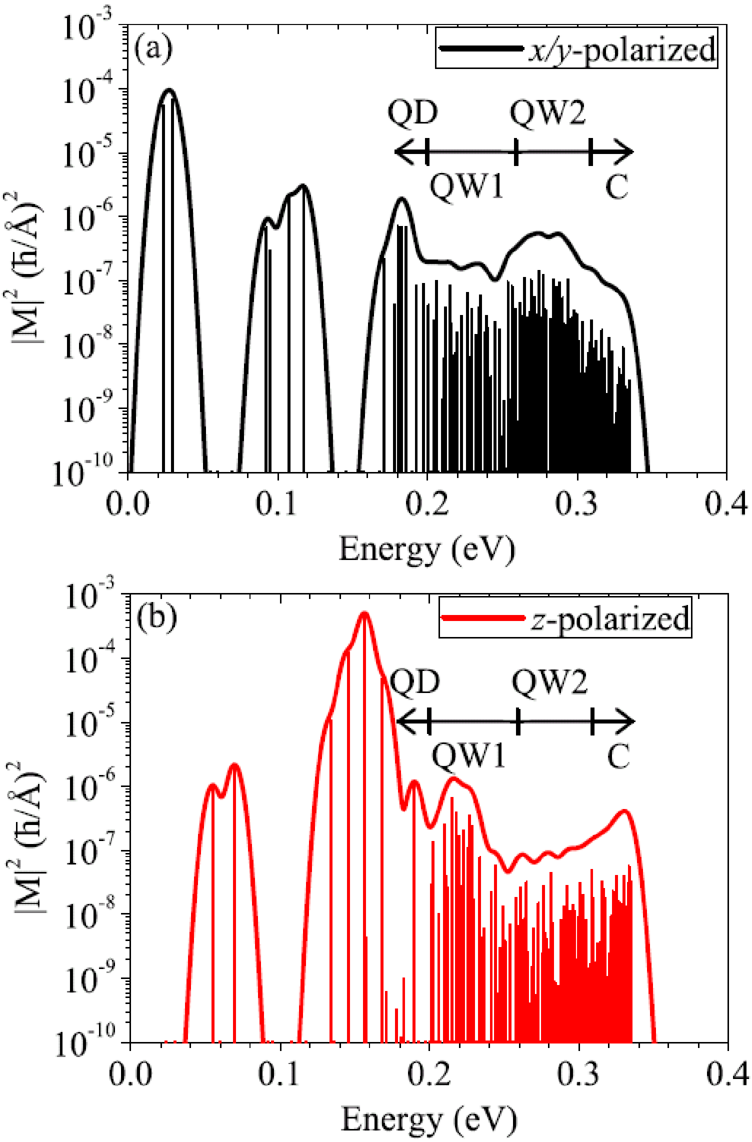

Figure 33. *Calculated zero-bias transitions at 77 K for TC In$_{0.75}$Ga$_{0.25}$As QDs, polarized (a) in-plane and (b) along growth direction, respectively. The drop lines show the energies of the transitions and their transition matrix elements. Bold lines show simulated spectra with superimposed Gaussian broadening of 10 meV FWHM.*

The *z*-polarized spectra (Figure 33b) show strong QD → QD transitions at 0.06 eV and 0.15 eV. QD → QW1 transitions are found to be stronger than QD → QW2 transitions by over an order of magnitude. This is due to the asymmetric position of the QD in the QW layer. The dominant contribution of the peaks at ≈ 0.03 eV in the *x*/*y*-polarized spectrum corresponds to transitions between the ground and first excited states in the dot. The wavefunctions of these states have different symmetries in the *x*/*y*-plane (*s*- and *p*-symmetries), resulting in large matrix elements for *x*/*y*-polarized transitions. Similarly, the dominating peak at ≈ 0.15 eV in the *z*-polarized spectrum is related to transitions to excited states which have *p*-symmetry in the *z*-direction. (It can be approximately described as the first excited state due to confinement in the growth direction.) The features of these peaks are in quantitative agreement with earlier modelling results for similar structures. [118]

5.3.4 Sensitivity to QD Parameters

As shown in Figure 31, the interband spectra are dramatically affected by the QD composition, primarily due to the band gap of the InGaAs alloy. The influence of the band gap change may not be so evident for the intraband transitions. Note however that the overall energy range for the mid-infrared intraband absorption is much smaller than that for the interband transitions. Because of that, the intraband spectra may be even more sensitive to details of the electronic structure of the DWELL system.

In this section, the effects of the dot parameters, such as their composition and shape, on the intraband spectra were investigated. The normal-incidence photocurrent experiments, which are used for comparison, correspond to in-plane (*x*/*y*) polarized light. In view of that, only the in-plane polarized absorption is considered, within the interested wavelength range of 3-10 µm (0.41-0.12 eV).

Figure 34 shows the simulated in-plane polarized spectra for TC $In_{1-x}Ga_xAs$ QDs with varying concentration in a range close to the value estimated from the PL spectra. Note that the spectra in Figure 34 is scaled linearly (not logarithmically as in Figure 33). One can see that the spectra are generally red-shifted with increasing Ga content, i.e. the effect is opposite to that for the interband spectra. The shift is as large as 1.5 meV for every 1% of Ga, which is substantial on the mid-infrared energy scale. Indeed, this red shift can be expected because the increasing band gap in the dot reduces the band offset in the conduction band. Therefore, while the dot energy levels move up, the intraband transition energies become smaller. For the same reason, the diminishing band offset between the dot and the QW reduces the overall number of excited electron levels in the dot. Hence, the shoulder in the QD → QD peak at 0.20 eV, present in the *x*=0.20 spectra, disappears with increasing *x*. Such a qualitative change in the spectra, on top of the peak shift, suggests a possibility to obtain an independent estimate of the dot composition from the photocurrent spectra.

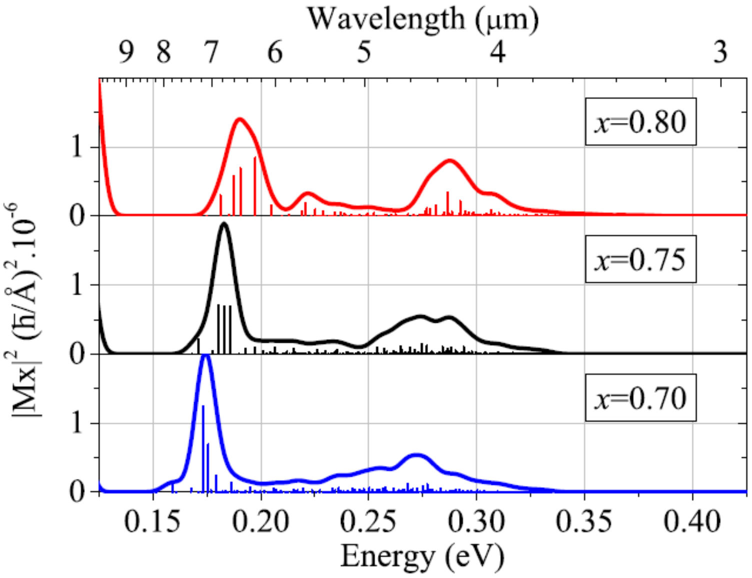

Figure 34. *Simulated spectra of zero-bias x/y-polarized transitions at 77 K for TC* $In_{1-x}Ga_xAs$ *dots with different Ga concentrations. Superimposed broadening of 10 meV was applied. The drop lines show individual transition energies and corresponding matrix elements.*

Next, we demonstrate that the QD shape can also have a significant effect on the absorption spectra. Figure 35 shows the simulated intraband spectra for truncated conical and truncated pyramidal dots of the same composition x=0.25. For the same base length and height, a truncated pyramid has a bigger volume than a truncated cone due to the wider diagonal size. Because of that, the electron states are better confined in the dot, which has two major effects on the QD → QD transitions. First, the better confinement leads to smaller size-quantisation energies and reduced separation between the dot electron levels. This results in a slight, 5-6 meV, red shift of the main QD → QD peak (the one at ≈ 0.18 eV for a conical dot). Second, a larger number of localised excited states in the dot become possible. As a result, additional absorption peaks appear in the spectra at energies just below 0.2 eV.

The intraband transition matrix elements can be also affected by the QD shape. This in turn can lead to somewhat misleading changes in the absorption spectra. Indeed, one can see that in the spectrum for the TC shape in Figure 35, there is a broad peak at ≈ 0.28 eV. For the TP shape, the peak shifts to lower energy (to ≈ 0.26 eV). However, careful examination of the transition energies shows that the subband-related transitions are in fact *blue-shifted*. This is as expected because the transitions are QD → QW2 range and the localised QD ground state is at a lower energy for pyramidal dots with larger volume.

At the same time, the effect of the dot shape on the quantum-well states is very small. Therefore, the apparent red shift of the absorption peak (between 0.25 eV and 0.3 eV) originates purely from the relative increase in the matrix elements for the lower-energy individual transitions contributing to the peak.

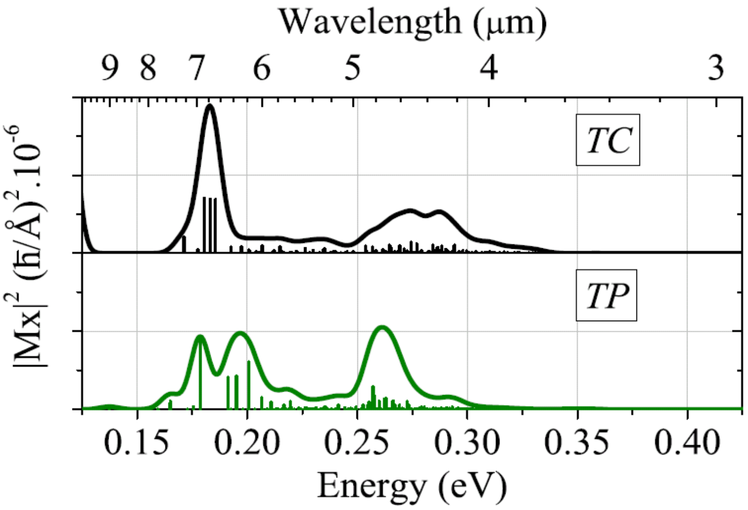

Figure 35. *Simulated spectra of zero-bias x/y-polarized transitions at 77 K for TC and TP* $In_{0.75}Ga_{0.25}As$ *dots, with superimposed Gaussian broadening of 10 meV.*

5.3.5 Comparison with the Experimental Spectra

Here we compared our modelling results with photocurrent spectra, both for analysis of the experimental data and to test the accuracy of the model. Figure 36 shows the experimental photocurrent spectra at various bias voltages. Note that distortions (fine substructure) around 4.3 μm and 5-7 μm are due to atmospheric absorption (CO_2 and H_2O, respectively). At a bias of V=-6 V (Figure 36a), a dominating peak at 0.275 eV is observed. Under a positive bias V=+6 V, the peak shifts to 0.30 eV. Two shoulders at around 0.24 eV and 0.35 eV are also observed. At a bias V=-12 V (Figure 36b), the peak is observed at ≈ 0.26 eV. For V=+12 V, the peak shifts to higher energy (≈ 0.31 eV). In addition, a strong peak emerges at around 0.185 eV under negative bias; under positive bias, it is observed at 0.19-0.20 eV.

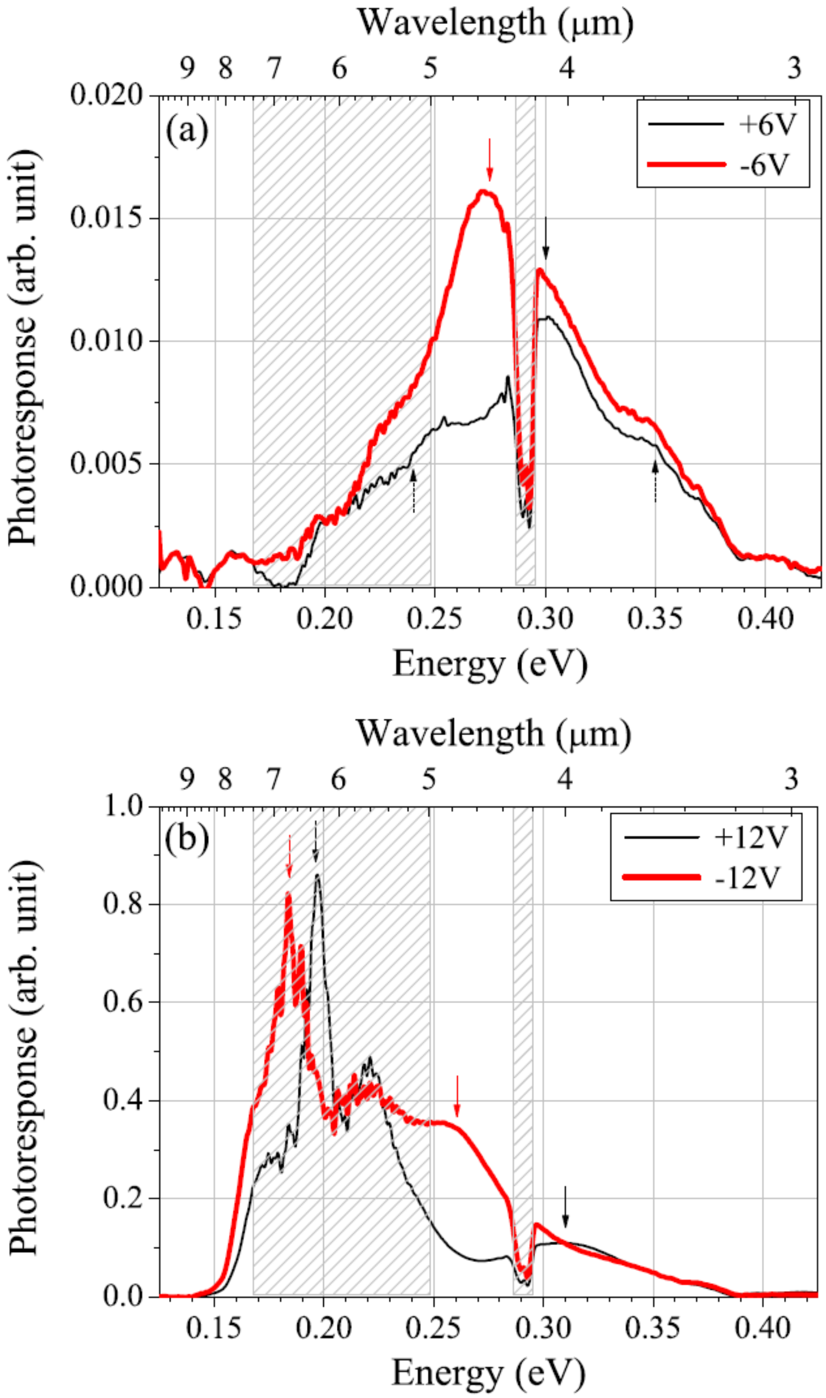

Figure 36. *Photocurrent spectra obtained at 77 K under (a) low bias and (b) high bias. Shaded bands at 4.3 μm and 5-7 μm correspond to atmospheric absorption band.*

Our modelling results suggest that the dominating peaks in the low bias spectra correspond to QD → QW2 transitions. The QD → QD transition is not observed at low bias because the carrier is deep in the potential well and not easily escape over the barrier. The lower- and higher-energy shoulders are attributed to QD → QW1 and QD → C transitions, respectively. In the high-bias spectra, the dominating peaks are associated with the QD → QD transition. Moreover, the much smaller shift for the lower-energy peak is consistent with its association with the QD → QD transition. As a result of applied bias, the barrier becomes triangular shape (as illustrated in Figure 27) and the effective barrier is lower and thinner. In this case, it is easier for the electrons from bound-to-bound transitions to escape and contributes to the current. Therefore, the QD → QD transition is observed only at high bias. The modelling allows the identification of the peaks in the spectra even in the case of strong distortion due to atmospheric absorption.

Figure 37 shows the energy positions of the main peaks (dark symbols) for different bias voltages. The blue shift of the peaks with voltage (from negative to positive) can be clearly seen. This is due to the quantum-confined Stark shift; the slower blue shift for positive bias is consistent with the asymmetric position of the QD in the QW. Moreover, the much smaller shift for the lower-energy peak is consistent with its association with the QD → QD transition. [119]

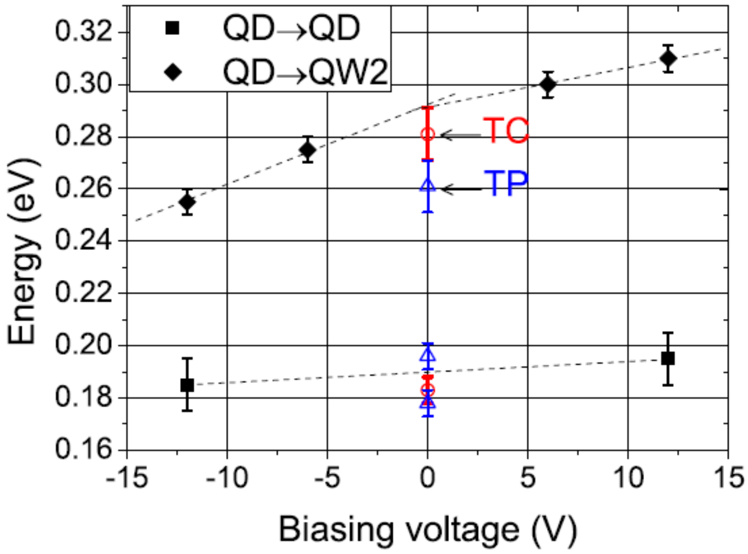

Figure 37. *Positions of the main peaks in the photocurrent spectra as a function of voltage. For non-zero voltages, experimental data are shown; for zero bias, modeling results are presented for* $In_{0.75}Ga_{0.25}As$ *dots for both TC and TP shapes. The dashed lines are guides for the eye.*

Figure 37 also shows comparison of the modelling results with the experimental data. The peak energies shown at non-zero voltages are the experimental data, while the values at zero bias were obtained from modelling. The experimental and modelling results agree within the experimental and modelling errors, supporting the trustworthiness of the model. Moreover, the energy of the experimental QD → QW2 peak strongly indicates the likelihood of the truncated conical shape of the dots. The latter is also supported by the observation of a single QD → QD peak in the experimental spectra, though this evidence is not definite because of the distortions in the spectra due to the atmospheric absorption. Nevertheless, it is in fact one of the most common shapes observed of InGaAs/GaAs QDs. [25,26]

5.4 Summary

The intraband absorption spectra in a quantum-dot-in-well heterostructure was investigated using photocurrent spectroscopy and computer modelling. A model with low computational cost based on continuum-elasticity and effective-mass approximations was employed. At the same time, a simplified approach to the continuum energy spectra in the quantum well was used. Despite its simplicity, good agreement with the experimental data confirms the trustworthiness of the model. The model has been successfully applied for analysis and interpretation of the experimental photocurrent spectra. Effects of shape and composition on the intraband absorption spectra in the DWELL structure were also predicted. The model provides a flexible and efficient tool for design of advanced DWELL systems.

Chapter 6

Structural Parameters of Quantum Dots Grown by In-flush Technique

6.1 Introduction

In general, the determination of optical spectra from a given set of structural parameters of a quantum dot is more or less an accomplished task. These structural parameters typically rely on time-consuming, destructive structural characterisation method such as transmission electron microscopy (TEM). On the other hand, it is of great challenge to work the other way round – to extract QD structural parameters from experimental optical spectra. This is because there are plenty of parameters for self-assembled quantum dots, such as shape, height, lateral size and composition. This leads to cumbersome and time consuming repetitive calculations. In order to make this approach feasible, it is necessary to reduce these independent variables, which in turn reduce the computational efforts required.

In this case, the self-assembled QDs grown by the In-flush technique [19,120,121,122,123,124] fit this purpose. This growth step has proved to be a promising method for the control of the QD height, which has the greatest effect on the size quantisation energy as this is typically the smallest dimension. Being the most explored system, InAs/GaAs and InGaAs/GaAs QDs are good choice for this task. This growth technique has gained popularity especially in the study of spin interaction in quantum dot molecules, where the coupling of vertically aligned QDs is adjusted by their heights. This provides possible applications in the fields of quantum information and spintronics. [125]

The growth procedures for this method are illustrated in Figure 38. After the formation of QDs, these are partially capped with GaAs at low temperature. Then, the sample is annealed in-situ at a higher temperature before being fully capped. During this procedure, the tops of the as-grown QDs are evaporated, producing truncated dots nominally as high as the thickness of the “low temperature” partial capping GaAs layer. At the same time, the annealing step enhances the cations (Ga and In) exchange between the QDs and the GaAs. This results in alloying of the QD even though binary InAs was nominally grown.

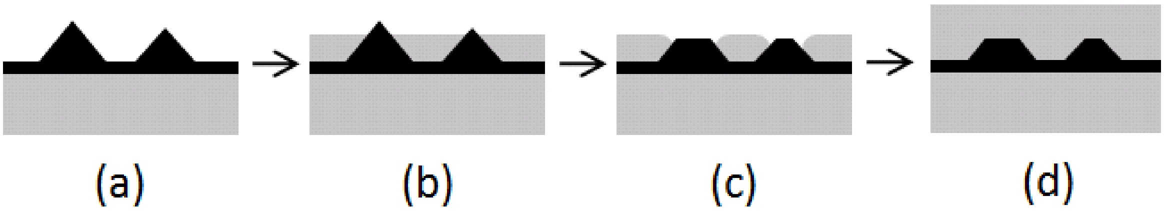

Figure 38. *Schematic of the In-flush growth procedure: (a) dot formation, (b) partial GaAs capping at low temperature, (c) annealing at higher temperature (In-flush), and (d) full GaAs capping of QDs.*

In this work, we attempt to extract the structural parameters of the In-flush grown QDs by combining photoluminescence (PL) results and modelling.

6.2 Methods

The major advantage of the In-flush QDs is that their height is known. Assuming a truncated conical dot, the remaining two main parameters are the base diameter and composition. Our approach is to calculate the optical transitions for a range of dot sizes and compositions, based on the multi-band model. The calculation results are then compared to information obtained from experimental optical spectra, such as the peak energies, splitting between ground- and excited-state transitions, and the energy shift of the ground state transition at different temperatures. This determines the empirical relationships for both composition and dot size, which are required to satisfy the experimentally observed optical spectra. In order to examine these empirical relationships clearer, they are presented in a so called “phase diagram” – a plot of QD composition against the QD lateral size. From these, the QD structural parameters can be extracted from the overlapping region.

In this work, a 3D model with a single quantum dot of truncated conical shape is employed. For simplicity, the dot is assumed to have homogeneous composition and abrupt interface. The schematic of the model is outlined in Figure 39. The height (H) of the QD is assumed to be a known parameter. The main variables are the base diameter (WB) and composition (i.e. In fraction). The facet angle (θ) is a relatively less important factor as compared to the base diameter (WB) and it can be accounted for by including an error bar in the phase diagram. Based on the general trend observed from experiments, the facet angle is set in the range of 25-35° depending on the height of the QD. Nevertheless, the effect is insignificant. The wetting layer (WL) is assumed to have a fixed thickness of 6Å (approximately 2 MLs) with the same composition as the QD.

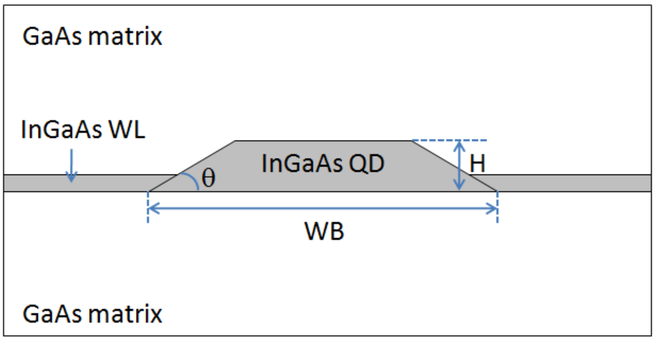

Figure 39. *Schematic of the geometry used for the QD. The height, base width and facet angle of the quantum dot are denoted by H, WB, and θ, respectively.*

For this work, several self-assembled InAs QDs samples were grown on undoped [001] GaAs substrate by an Oxford Instruments V90 Molecular Beam Epitaxy (MBE). After oxide desorption, 300 nm thick GaAs buffer layer followed by 100 nm of AlGaAs (30% Al) and 65 nm GaAs were grown at 580°C. Then, the temperature was reduced to 510°C for the deposition of 2.0 MLs of InAs forming self-assembled QDs. First, the QDs were partially capped with "low-temperature" GaAs (i.e. same temperature as for the QDs: 510°C), and then annealed in-situ at 620°C for 60 seconds. During this procedure, the tops of the as-grown QDs were re-evaporated, producing truncated dots nominally as high as the thickness of the low temperature GaAs layer. Finally, the growth was resumed with the deposition of 65 nm thick GaAs at 580°C. Figure 40 shows a schematic diagram of the QD structure.

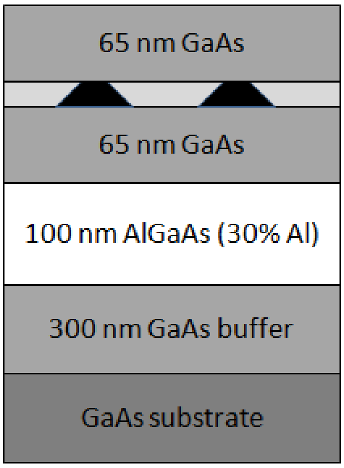

Figure 40. *Schematic diagram of the InAs/GaAs QD structure.*

For this study, three samples with “low temperature” GaAs layer thickness (i.e. QD height) of 3.5 nm, 4.3 nm and 5.2 nm were studied. These samples were grown by Dr Maxime Hugues (from University of Sheffield, now at CRHEA-CNRS, France), who also responsible for providing all sample characterisations (TEM) and optical experimental studies.

Standard PL measurements were performed at low temperature (LT) (i.e. 10 K) and at room temperature (RT) (i.e. 300 K) using the 514.5 nm line of an Ar+-ion laser and a liquid-nitrogen cooled Ge detector.

6.3 Results and Discussions

6.3.1 Low Temperature PL Spectra

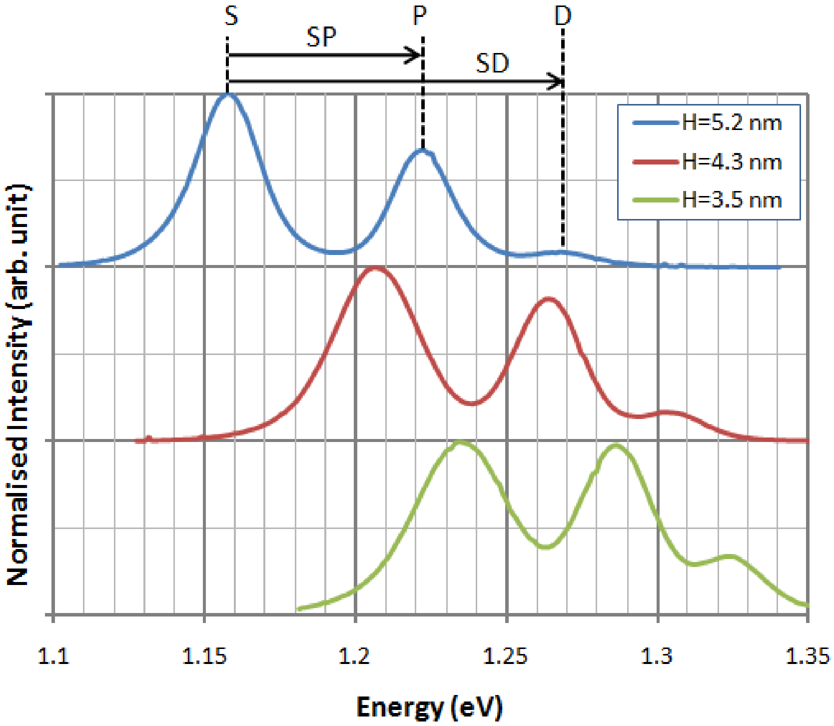

Figure 41. *Normalised PL spectra for QDs of different heights measured at 10 K.*

At first, the PL spectra are inspected to define useful information for comparison with calculations. Figure 41 shows normalised PL spectra for QDs with different height measured at 10 K. The peaks of these spectra correspond to emissions from dot ensembles. Each spectrum shows three distinct peaks, attributed to the ground- (S), first excited- (P) and second excited-state (D) transitions. Apart from absolute peak positions, the separation energy between the ground- and excited-state transitions, denoted as SP and SD, respectively, can also be used as parameters for comparison with calculations. The uncertainty for determining the peak positions from the spectra is roughly ±1-2 meV. In this case, an error bar of ±1 meV is assumed for the absolute peak position (i.e. S), and ±2.5 meV for the splitting energies (i.e. SP and SD).

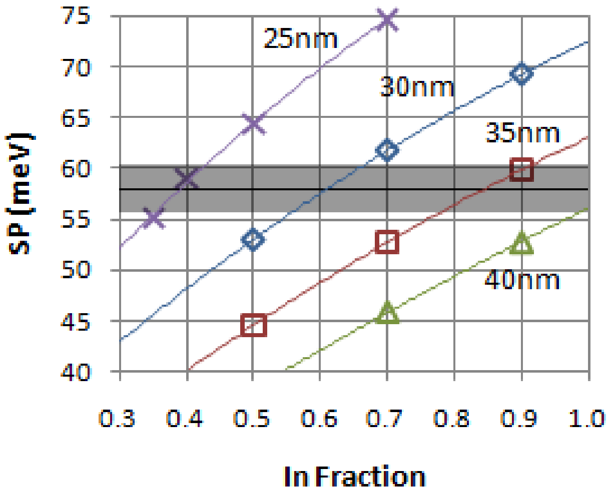

Figure 42. *SP energy as a function of the In fraction for QDs with height of 4.3 nm. Symbols are the calculated energies for QD base diameters of 25-40 nm. The curves represent interpolations of the calculated data. The horizontal black bold lines mark the measured data, whereas the shaded region corresponds to an error bar of ±2.5 meV.*

In order to demonstrate how a "phase diagram" is constructed, the QD with height of 4.3 nm is used as an example. Figure 42 shows the calculated SP splitting energies as a function of composition for several QD base diameters. Here, the symbols represent the results of calculations and curves are their interpolations. The bold horizontal line shows the measured SP splitting. The shaded region provides a guideline for an uncertainty of ±2.5 meV in the value of SP. From this diagram, using the crossing points between the modelling curves and the horizontal experimental line, the combinations of the two parameters, which are required to satisfy the observed PL data, can be determined for each dot size. These crossing points are inputs to the "phase diagram" as shown by the symbols in Figure 43. In this figure, the line is used to interpolate the data points. In the phase diagram, the error bars for composition (i.e. In fraction) are determined by the uncertainty of ±2.5 meV used in the plot of Figure 42, whereas ±2 nm is used to account for the uncertainty in the facet angle.

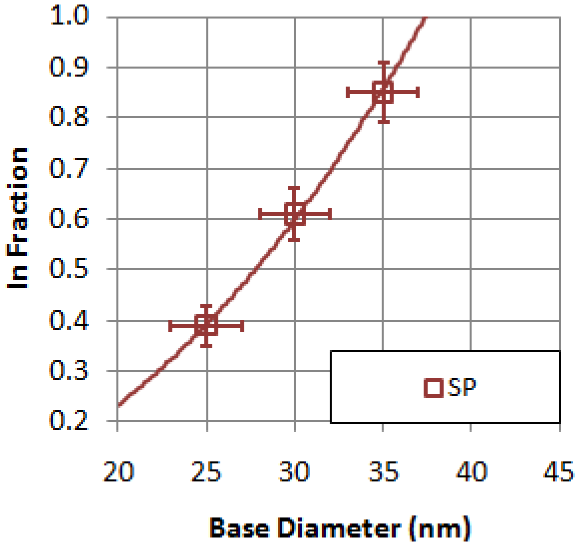

Figure 43. *"Phase diagram" derived from the analysis of SP for QDs of H=4.3 nm.*

Using the same procedures, more lines can be added on the "phase diagram" using other information obtained from the low temperature spectra, i.e. the S transition and the SD splitting energies. The comparisons between the calculations and the experimental data are shown in Figure 44.

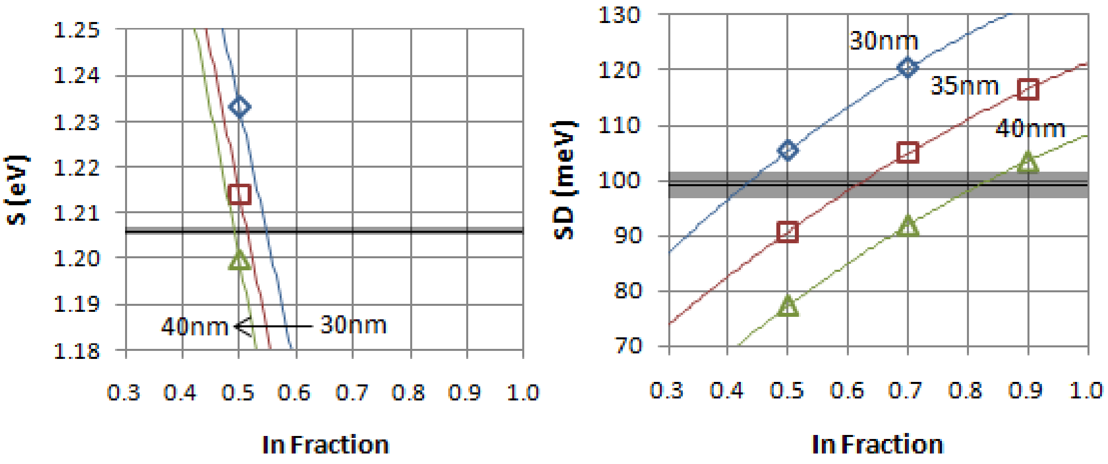

Figure 44. *S (left) and SD (right) as a function of the In fraction for QDs with height H=4.3 nm and different base diameters (30-40 nm). The symbols represent results of the calculations and the curves are their corresponding interpolations. The horizontal lines mark the measured PL data. The shaded regions correspond to error bars: ±1 meV for the S peak position and ±2.5 meV for the SD splitting.*

6.3.2 Energy Shift of Ground-state Transition (10 K – 300 K)

In addition to the three empirical relationships obtained from the low temperature PL spectra, there is another useful parameter – the energy shift of ground-state transition between low and room temperature, denoted as S (ΔT). It is worth noting that apart from using different band parameters (such as lattice constants and band gaps) to account for the temperature dependence of the band structure, there is another effect that has to be considered. Self-assembled QDs are bound to have size variations. This inhomogeneous broadening in the QD ensemble can be represented by a Gaussian distribution of density of states (DOS). At high temperature, carrier redistribution occurs in order to establish thermal equilibrium. By means of thermal excitation, charge carriers in smaller dots are excited above the inter-dot barriers and redistribute into larger dots at thermal equilibrium. Although the carrier thermalisation may occur partially, and depend on the QD density and size, it is still a good first approximation to account this in the calculation. Assuming Boltzmann distribution for the electrons and holes, this effect can be approximated by superimposing an exponential curve $\exp(-\hbar\omega/kT)$ on the Gaussian-broaden DOS, where k is the Boltzmann constant and T is the temperature. Effectively, this shifts the peak to lower energy as illustrated in Figure 45. The correction to S (ΔT) depends on the FWHM of the PL peak. At the same time, the barrier height is much greater at low temperature in which this effect is suppressed. Hence, the spectra reflect the DOS only.

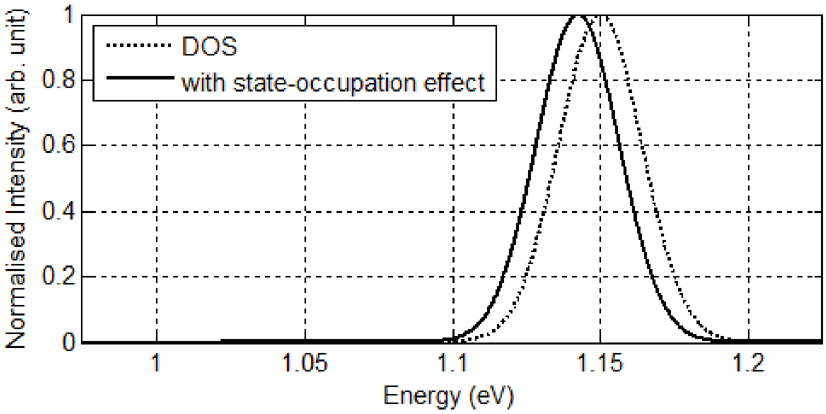

Figure 45. *DOS with (solid line) and without (dashed line) partial state-occupation effect due to carrier redistribution at high temperature.*

Figure 46 shows the calculated S (ΔT) with (open symbols) and without (closed symbols) the state-occupation effect for two different dot heights. The solid and dashed lines are the corresponding interpolations. Horizontal lines are the measured PL data, while shaded regions represent their uncertainties of ±2.5 meV.

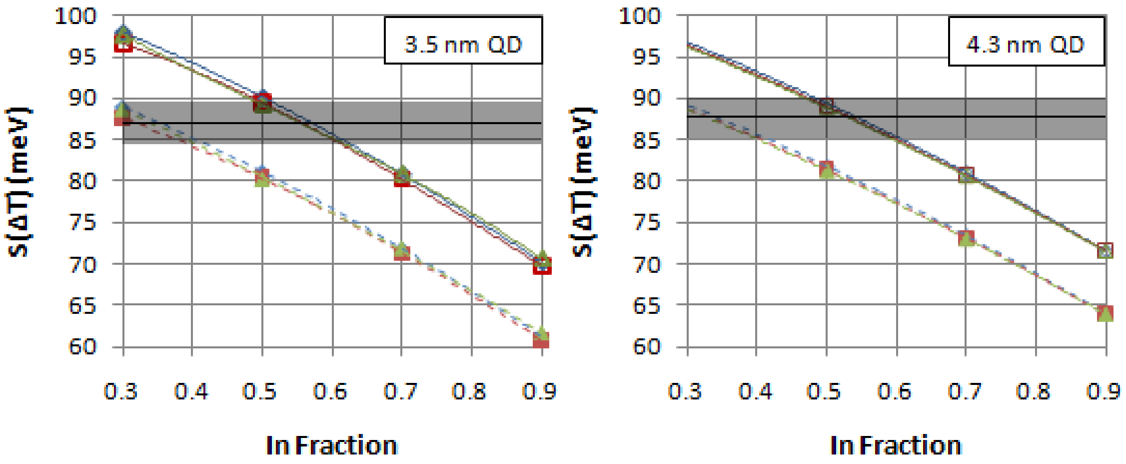

Figure 46. *S (ΔT) for QDs with heights of 3.5 nm (left) and 4.3 nm (right), for several base diameters (30-40 nm). Open symbols are calculations taking into account the effect of partial state-occupation due to carrier redistribution at high temperature, whereas closed symbols ignore this effect. Lines are for interpolation purposes.*

In general, S (ΔT) is found to be almost independent from the size of the QD. In contrast, it is very sensitive to the dot composition, with approximately 4-5 meV shift for every 10% of In content. If the effect of partial state-occupation due to carrier redistribution at high temperature is ignored, the S (ΔT) will be underestimated by as much as 10 meV (or 20% of In content) for these samples. This shift of the ground-state transition with temperature originates mainly from the band gap change of the quantum dot. The bulk band gap is both temperature- and composition- dependent. Since composition remains the same, its shift with temperature can then be used to determine the composition. Indeed, the QD size variation could also change the size quantisation energy, thus altering the effective band gap. However, in this case, the height of the QD being the smallest dimension (which has the greatest effect on size quantisation energy) is fixed. At the same time, the effect of the much larger lateral dimension (hence less sensitive to size quantisation energy) is relatively small for the change considered in this study. Hence, the shift due to the size variation is negligible, as shown in Figure 46.

6.3.3 Phase Diagram and Structural Parameters of QDs

By combining these empirical relationships, i.e. S, SP, SD, and S (ΔT), the final form of the phase diagram is then obtained. Using the same procedures, three phase diagrams are constructed for different dot heights, as shown in Figure 47. The overlapped regions give an estimate of the structural parameters of the QD.

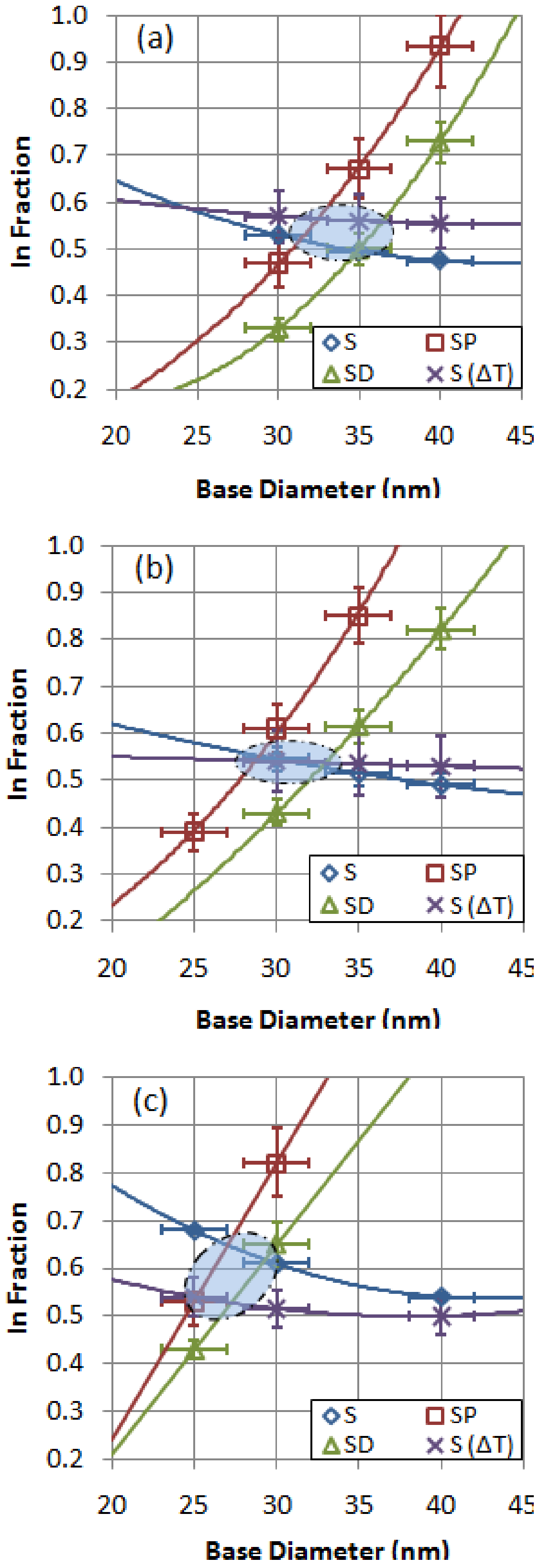

Figure 47. *Phase diagram of InGaAs QDs with height of (a) 3.5 nm, (b) 4.3 nm and (c) 5.2 nm. The blue shaded regions identify the QD structural parameters.*

Ideally, we expect all four curves to intersect at one point, giving exact structural parameters of the QDs. However, this is usually not the case. As shown in the figures, some curves never cross each other. This is due to some uncertainties including the experimental errors, the size variation of the QDs and assumptions made in the model. Nevertheless, a reasonable estimate can still be obtained.

Figure 48 shows a summary of the estimate of base diameters and compositions (represented by symbols) as a function of the QD height. Dashed lines indicate general trends of the studied samples. In general, both parameters have approximately 10 % of experimental error. The QD base diameter is found to reduce with increasing the QD height. On the other hand, the In concentration is found to be greater for taller QDs. Possible explanations for these trends are due to the effect of the annealling process in the In-flush growth step and the assumptions of homogeneous composition and abrupt interface used in the model. However, the underlying mechanism is unclear and requires further investigation.

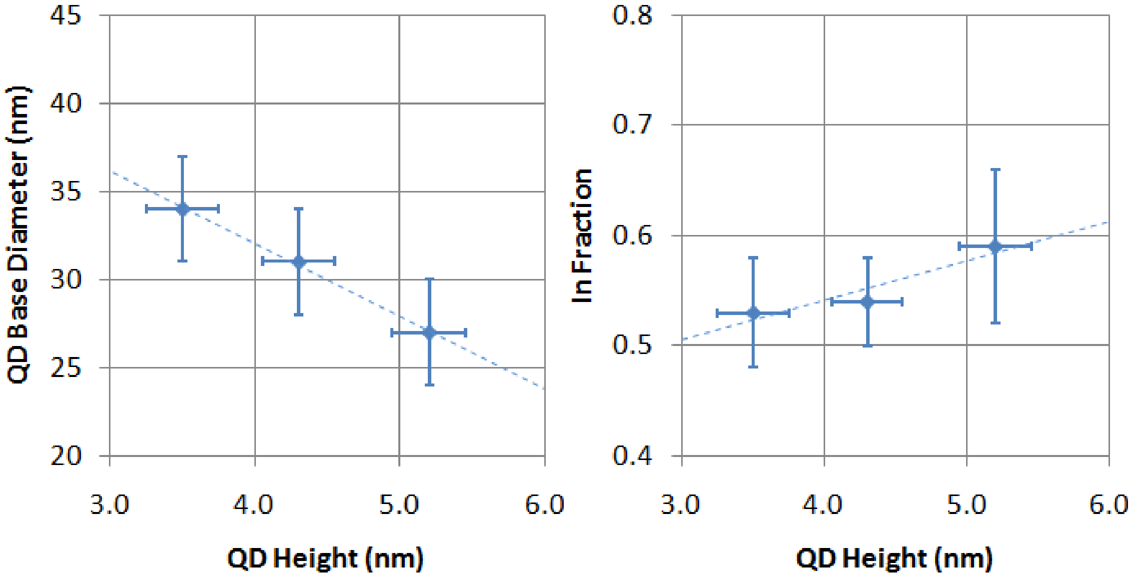

Figure 48. *Estimate of the base diameter and In-composition obtained from the phase diagrams of Figure 47.*

6.3.4 Comparison to TEM

In order to validate our approach, TEM was performed on two samples based on QDs with height of 3.5 nm and 4.3 nm. To get the average parameters, a number of quantum dot images from the same sample were overlapped and averaged, from which the physical parameters were measured. (This is a common approach that has been widely used to provide structural parameters of quantum dots.) The averaged TEM images are shown in Figure 49, and their measured parameters are tabulated in Table 6. The contrast change within the dot is due to the effect of strain. The facet angles are found to be in agreement with the assumption used in the calculations. In general, the facet is steeper for taller dots.

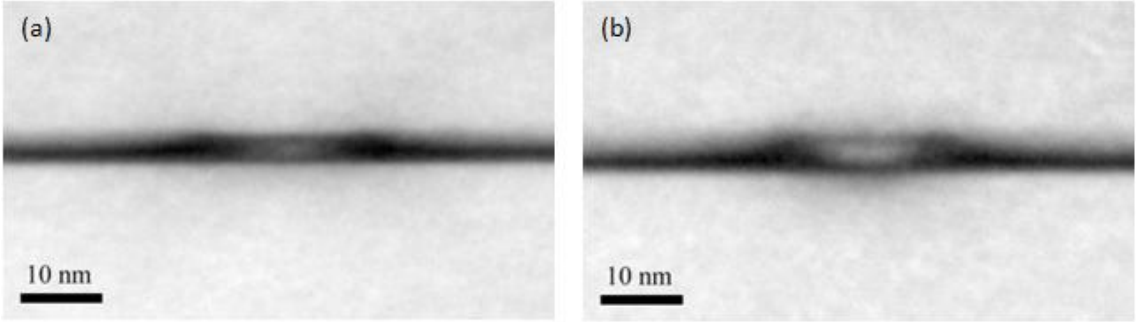

Figure 49. *Averaged TEM images for QDs with heights of (a) 3.5 nm and (b) 4.3 nm.*

H (nm)	WB (nm)	θ (degrees)
3.5	36.3	25.1
4.3	33.4	31.6

Table 6. *QD base diameters and facet angles measured from averaged TEM images.*

The TEM-measured base diameters are plotted with the estimated values obtained from the phase diagrams, as shown in Figure 50. The diamond symbols show the estimates from the phase diagram, while the square symbols represent the data from TEM. The results show good agreement between the approach used in this work (combination of modelling and PL) and the TEM data. Most importantly, the tendency of smaller base diameters with increasing dot heights has been successfully captured in our model. Due to the fact that quantum dots of a real sample are unavoidably to have size variations, there is also an uncertainty in the data obtained from TEM. A possible explanation for the apparent consistent underestimate may again due to uncertainties in the parameters and model assumptions. This will be further investigated by using a more realistic inhomogeneous composition profile based on a diffusion model.

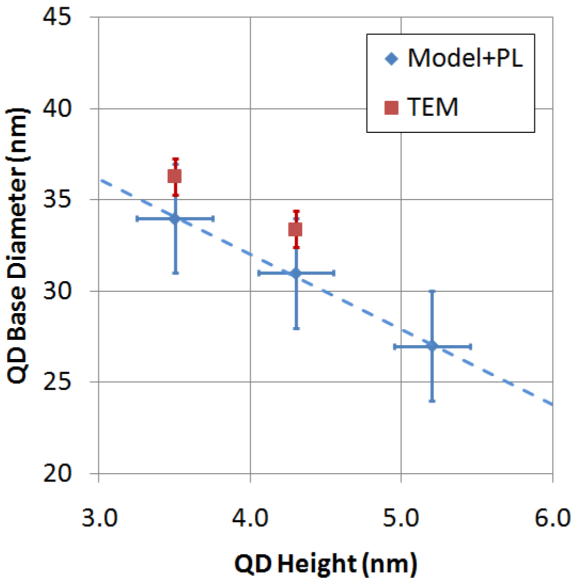

Figure 50. *Comparison of the base diameters obtained from the "phase diagrams" (diamond symbols) with those measured from averaged TEM images (square symbols). The dashed line is a guide for the eye.*

6.4 Summary

The results of the proposed approach indicate that a decrease in the dot height is followed by an increase in both the average base size and the Ga content. Most importantly, the results match well the data obtained from the TEM studies. This approach provides valuable information about the composition of QDs. In addition, it can be used to provide prediction of structural parameters for QDs grown under similar conditions. Therefore, the structural parameters of QDs grown by the In-flush method, can be obtained by a combination of optical spectroscopy and modelling, without resorting to time consuming structural characterizations methods.

Chapter 7

Concluding Remarks

7.1 Conclusions

The employment of the Finite Element Method in the modelling of semiconductor heterostructures has been proved to be feasible. The ease of use and powerful solvers of COMSOL Multiphysics have substantially improved the work efficiency. In addition, it provides a good platform for further development of the model due to its capability to couple multiple physics problems in the same model. Throughout the study, multi-band $\boldsymbol{k}\cdot\boldsymbol{p}$ method has proved to be computationally efficient with great accuracy for calculating the band structure of different semiconductor heterostructures including superlattices, quantum dots and hybrid systems.

The modelling of type II InAs/GaSb short-period superlattices has been revisited, to investigate the physical origin of the apparent failure of the $\boldsymbol{k}\cdot\boldsymbol{p}$ method with this structure. Based on experimental studies, the interface of these structures was found to be asymmetric and with graded composition. With a simple but more realistic interface profile based on experimental observations, band structure calculations were performed within the $\boldsymbol{k}\cdot\boldsymbol{p}$ method. The calculations have shown that the *asymmetric* interfacial segregation results in a significant reduction in the size-quantization energy for the electron miniband, leading to a reduction in the fundamental energy gap. A good agreement was achieved in the comparison with the experimental data, both from our own measurements and from the published literature. It has been demonstrated that the $\boldsymbol{k}\cdot\boldsymbol{p}$ method can be used for InAs/GaSb SPSLs with a good predictive ability, as long as the real physical structure of the interface is taken into account.

The electronic properties of a DWELL sample for a wide range of QD parameters were also explored. By calculating the transition matrix element, intraband spectra have been simulated. In particular, the effects of composition and shape of the QD on the intraband absorption spectra were investigated. The results show good agreement with the experimental data and allowed interpretation of complex photocurrent spectra. The model provides a flexible and expandable tool for design of the advanced DWELL systems.

The structural parameters of InAs/GaAs quantum dots grown by the In-flush technique were investigated with a combination of optical spectroscopy and modelling. Assuming the height of the QD is a known parameter, systematic band structure calculations were performed using the strain-dependent $\boldsymbol{k} \cdot \boldsymbol{p}$ method for a range of dot parameters. The modelled energy shift due to temperature change was found to be insensitive to the size variation. On the other hand, it changes significantly with the composition of QD, by as much as 4 meV for a 10% variation. This provides valuable information concerning the QD structure.

By using the PL peak energies, the splitting between the ground- and excited-states transitions and the energy shift between low and room temperature, a phase diagram can be constructed which is a plot of the QD composition against the QD base diameter. Both parameters can then be obtained from the overlapped region in the phase diagram. The results show excellent agreement with the TEM measured values. This proved to be a feasible approach for fast extraction of QD information without resorting to time-consuming structural characterisation methods.

7.2 Further Development

Currently, the band structure model is based on an eight-band $\boldsymbol{k} \cdot \boldsymbol{p}$ Hamiltonian with the effects of strain and linear piezoelectricity included. The use of FEM in a 3D model allows modelling of various heterostructures including quantum dots of arbitrary shape and hybrid systems of different dimensionality. There is still a lot of room for improvement to achieve better approximation to the real structure. Some of the natural expansions of the existing continuum model (particularly in the 3D model) are already outlined here, although they are yet to be applied in practical studies.

Effect of Inhomogeneous Composition

Due to interdiffusion, semiconductor heterostructures of the III-V group are often found to be ternary, or sometimes even quaternary, compounds whereas a binary compound was nominally grown. The effect of inhomogeneous composition on the electronic band structure is sometimes tremendous, especially for quantum dots due to their small size. To account for that, a diffusion model is required. For a continuum model, Fick's law tends to be a direct approach. [112]

In particular, the approach used in the study of structural parameters of In-flush QDs can be extended by using a diffusion model to account for more realistic effects of the annealing step. This will then remove the assumptions of homogeneous composition and abrupt interface. Therefore, the composition profile for the model can be better approximated to match the real samples.

Second Order Piezoelectric

In this work, the piezoelectric polarisation discussed is of linear type and the tensor is measurable experimentally. Recently, Bester et al. [126] found from first principles calculation that the piezoelectric tensors of GaAs and InAs have large nonlinear components. After investigating several cases for different heterostructures, they concluded that its effect is significant and should be included. Although the inclusion of nonlinear piezoelectric is not yet widely implemented in the modelling of semiconductor heterostructures, its concept and consequence are generally accepted.

Appendix A

Matlab Programs

This section presents Matlab codes written and used to calculate for exciton binding energy for interband transitions and to simulate optical spectra (which involves computing the transition matrix element) for intraband transitions.

A.1 Exciton Binding Energy

This is an example of Matlab code used in calculating the exciton binding energy of a quantum dot. The details of the formulation are described in Section 2.6.

```
disp('############################################################');
disp('Calculation: Exciton binding energy');
text=sprintf('Started at %s.',datestr(now));disp(text);
tic;
disp('~~~~~~~~~~~~~~~~~~~~~~~~~~~~~~~~~~~~~~~~~~~~~~~~~~~~~~~~~~~~');
disp('1.  PREPROCESSING');
disp('~~~~~~~~~~~~~~~~~~~~~~~~~~~~~~~~~~~~~~~~~~~~~~~~~~~~~~~~~~~~');
disp('Set parameters ...                                  (1 of 6)');
resx=1.5;         % resolution along X/Y, points per nm
resz=1.5;         % resolution along Z
EGS=13;         % solution no. of electron ground state
V=1:6;          % QD-QD transitions: (1)E0-H0 (2)E2-H1
(3)E1-H2(4)E3-H3(5)E3-H4(6)E4-H5(7)E5-H3
solh=(EGS-1)-2*(V-1);
sole=EGS+2*(V-1);
xmin=-20e-9;    % min point in xy-axis (nm)
xmax=20e-9;     % max point in xy-axis (nm)
zmin=-3e-9;     % min point in z-axis (nm)
zmax=8e-9;      % max point in z-axis (nm)
nx=((xmax-xmin)/1e-9)*resx+1;      % no. of points in x-axis
ny=((xmax-xmin)/1e-9)*resx+1;      % no. of points in y-axis
nz=((zmax-zmin)/1e-9)*resz+1;      % no. of points in z-axis
dx=(xmax-xmin)/(nx-1);dy=(xmax-xmin)/(ny-1);dz=(zmax-zmin)/(nz-1);
disp('                                                       done!');
text=sprintf('Electron states = %s',int2str(sole));disp(text);
text=sprintf('Hole states     = %s',int2str(solh));disp(text);
text=sprintf('Grid region     = (%0.1f to %0.1f)nm in X/Y; (%0.1f
to %0.1f)nm in Z',xmin/1e-9,xmax/1e-9,zmin/1e-9,zmax/1e-9);disp(text);
text=sprintf('Grid resolution = %0.2fnm in X/Y; %0.2fnm in
Z',dx/1e-9,dz/1e-9);disp(text);
text=sprintf('Grid size       = %0.0f x %0.0f
x %0.0f',nx,ny,nz);disp(text);
text=sprintf('Matrix size     = %0.0f',nx*ny*nz);disp(text);
text=sprintf('Computing time  ~ %0.0f
mins',round((nx*ny*nz)^2/(52900)^2*8.6));disp(text);
disp('____________________________________________________________');
disp('Construct grid ...                                  (2 of 6)');
[x,y,z]=meshgrid(xmin:dx:xmax,xmin:dy:xmax,zmin:dz:zmax);
```

```
grid=[x(:)';y(:)';z(:)'];
disp('                                                       done!');
clear nx ny nz xmin xmax zmin zmax x y z resx resz;
disp('____________________________________________________________');
disp('Extract solutions ...                               (3 of 6)');
[elambdat]=postinterp(fem,'real(lambda)',[0;0;0],'solnum',sole);
[hlambdat]=postinterp(fem,'real(lambda)',[0;0;0],'solnum',solh);
elambda=[sole'-EGS+1 elambdat(:,1)];
hlambda=[solh'-EGS hlambdat(:,1)];
clear elambdat hlambdat;
disp('                                                       done!');
disp('    Electron (eV)      Hole States (eV)');
disp('    ----------------   -----------------');
disp([elambda hlambda]);
disp('____________________________________________________________');
disp('Prepare for normalisation ...                       (4 of 6)');
% calculated integral from COMSOL file
[intue]=postint(fem,'u1*conj(u1)+u2*conj(u2)+u3*conj(u3)+u4*conj(u4)+u
5*conj(u5)+u6*conj(u6)+u7*conj(u7)+u8*conj(u8)','solnum',sole);
[intuh]=postint(fem,'u1*conj(u1)+u2*conj(u2)+u3*conj(u3)+u4*conj(u4)+u
5*conj(u5)+u6*conj(u6)+u7*conj(u7)+u8*conj(u8)','solnum',solh);
disp('                                                       done!');
disp('____________________________________________________________');
disp('Load and normalise data ...                         (5 of 6)');
[Epd]=postinterp(fem,'u1*conj(u1)+u2*conj(u2)+u3*conj(u3)+u4*conj(u4)+
u5*conj(u5)+u6*conj(u6)+u7*conj(u7)+u8*conj(u8)',grid,'solnum',sole);
[Hpd]=postinterp(fem,'u1*conj(u1)+u2*conj(u2)+u3*conj(u3)+u4*conj(u4)+
u5*conj(u5)+u6*conj(u6)+u7*conj(u7)+u8*conj(u8)',grid,'solnum',solh);
nEpd=zeros(size(Epd));nHpd=zeros(size(Hpd));
for i=1:1:size(Epd,1)
    nEpd(i,:)=(Epd(i,:)./(intue(i)));
    nHpd(i,:)=(Hpd(i,:)./(intuh(i)));
end
clear Epd Hpd;
disp('                                                       done!');
disp('____________________________________________________________');
disp('Check approximation accuracy ...                    (6 of 6)');
checke=sum(nEpd*dx*dy*dz,2)-1;
checkh=sum(nHpd*dx*dy*dz,2)-1;
disp('                                                       done!');
disp('Estimate error for electron density (%) =');disp(checke*100);
disp('Estimate error for hole density (%)     =');disp(checkh*100);
toc;
disp('~~~~~~~~~~~~~~~~~~~~~~~~~~~~~~~~~~~~~~~~~~~~~~~~~~~~~~~~~~~~');
disp('2. PROCESSING');
disp('~~~~~~~~~~~~~~~~~~~~~~~~~~~~~~~~~~~~~~~~~~~~~~~~~~~~~~~~~~~~');
disp('Calculate exciton binding energy ...                (1 of 1)');
es=15;
e0=1e7/(4*pi*3e8*3e8);
%e0=1e7/(4*pi*299792458*299792458);
e=1.60217646e-19;
C=(e*e/(4*pi*e0*es))*dx*dy*dz*dx*dy*dz;
clear es e0;

cs=size(grid,2);
Ex=zeros(7,1);
r=zeros(1,cs);
for i=1:1:cs          % initial electron state

r=sqrt((grid(1,i)-grid(1,:)).^2+(grid(2,i)-grid(2,:)).^2+(grid(3,i)-gr
id(3,:)).^2);
    r(i)=1;
    Ex=Ex+C*[
```

```
        sum((nEpd(1,i)*nHpd(1,:))./r,2); %E0-H0
        sum((nEpd(3,i)*nHpd(2,:))./r,2); %E2-H1
        sum((nEpd(2,i)*nHpd(3,:))./r,2); %E1-H2
        sum((nEpd(4,i)*nHpd(4,:))./r,2); %E3-H3

sum((nEpd(3,i)*nHpd(1,:))./r,2)+sum((nEpd(1,i)*nHpd(2,:))./r,2)-sum((n
Epd(3,i)*nEpd(1,:))./r,2)-sum((nHpd(1,i)*nHpd(2,:))./r,2); %E2-H1

sum((nEpd(2,i)*nHpd(1,:))./r,2)+sum((nEpd(1,i)*nHpd(3,:))./r,2)-sum((n
Epd(2,i)*nEpd(1,:))./r,2)-sum((nHpd(1,i)*nHpd(3,:))./r,2); %E1-H2

sum((nEpd(4,i)*nHpd(1,:))./r,2)+sum((nEpd(4,i)*nHpd(2,:))./r,2)+sum((n
Epd(4,i)*nHpd(3,:))./r,2)+sum((nEpd(1,i)*nHpd(4,:))./r,2)+sum((nEpd(2,
i)*nHpd(4,:))./r,2)+sum((nEpd(3,i)*nHpd(4,:))./r,2)-sum((nEpd(4,i)*nEp
d(3,:))./r,2)-sum((nEpd(4,i)*nEpd(2,:))./r,2)-sum((nEpd(4,i)*nEpd(1,:)
)./r,2)-sum((nHpd(1,i)*nHpd(4,:))./r,2)-sum((nHpd(2,i)*nHpd(4,:))./r,2
)-sum((nHpd(3,i)*nHpd(4,:))./r,2); %E3-H3
                ];
end
Ext=Ex+[0;0;0;0;Ex(2,1)+Ex(5,1);Ex(3,1)+Ex(6,1);Ex(4,1)+Ex(7,1)];
disp('                                                       done!');
toc;
disp('____________________________________________________________');
disp('Exciton binding energy (meV) =');disp(Ext/e*1000);
text=sprintf('Total calculation time = %0.1f mins',toc/60);disp(text);
text=sprintf('Finished at %s.',datestr(now));disp(text);
disp('############################################################');
```

A.2 Spectra Simulation

The following is a simple Matlab program used in the calculation of the transition matrix element and spectra simulation in the study of DWELL structures. The details of the formulation for the transition matrix element is explained in Section 2.7, whereas the simulation of the spectra is done by superimposing broadening on the calculated matrix elements.

```
tic;
disp('Program features:');
disp('  (a)Calculate transition matrix element from ground state to
excited states');
disp('  (b)Simulate spectra by superimposing matrix elements with
broadening');
disp('==============================================');
disp('(a)  TRANSITION MATRIX ELEMENT CALCULATION');
disp('==============================================');
% building grid ------------------------------------
disp('Meshing model ...');
%%%%%%%%%%%%%%%%%%%%%%%%%%%%%%%%%%%%%%%%%%%%%%%%%%%%%%%%%%%%%%%%%%%%%%
%%%%%%%%%
sol='all';      % solutions used
GS=1;
res=4;          % grid per dot
nx=40*res+1;      % no. of points in x-axis
ny=40*res+1;      % no. of points in y-axis
nz=16*res+1;      % no. of points in z-axis
xmin=-20e-9;      % min point in xy-axis
xmax=20e-9;       % max point in xy-axis
```

```
zmin=-4e-9;       % min point in z-axis
zmax=12e-9;       % max point in z-axis
% Plot settings
q=1;            % Broadening shape: 1=Gaussian, 2=Lorentzian
p=0;            % Plot spectra: 1=Yes
g=0.010;        % FWHM
%%%%%%%%%%%%%%%%%%%%%%%%%%%%%%%%%%%%%%%%%%%%%%%%%%%%%%%%%%%%%%%%%%%%%%
%%%%%%%%
dx=(xmax-xmin)/(nx-1);
dy=(xmax-xmin)/(ny-1);
dz=(zmax-zmin)/(nz-1);
[x,y,z]=meshgrid(xmin:dx:xmax,xmin:dy:xmax,zmin:dz:zmax);
grid=[x(:)';y(:)';z(:)'];
disp('  (1 of 1)');

disp('Mesh resolution x,y,z (nm) =');disp([dx/1e-9 dy/1e-9 dz/1e-9]);
disp('Grid size (x,y,z) ='); disp([nx ny nz]);
clear x y z;

disp('Clustering grid ...');
% break grid into smaller grid clusters
gs=round(size(grid,2)/8+1);
grid1=grid(:,1:gs);
grid2=grid(:,gs+1:2*gs);
grid3=grid(:,2*gs+1:3*gs);
grid4=grid(:,3*gs+1:4*gs);
grid5=grid(:,4*gs+1:5*gs);
grid6=grid(:,5*gs+1:6*gs);
grid7=grid(:,6*gs+1:7*gs);
grid8=grid(:,7*gs+1:end);
if
size(grid,2)==(size(grid1,2)+size(grid2,2)+size(grid3,2)+size(grid4,2)
+size(grid5,2)+size(grid6,2)+size(grid7,2)+size(grid8,2))
    clear grid gs;
else
    disp('>> Error: Mesh clusterisation!');
end
disp('  (1 of 1)');

disp('-------------------------');
disp('Extracting solutions ...');
[elambda]=postinterp(fem,'lambda',[0;0;0],'solnum',sol);
lambda=[(1:1:size(elambda,1))' elambda(:,1)];
clear elambda;
disp('  (1 of 1)');

disp('-------------------------');
disp('Preparing for normalisation ...');
% calculated integral from COMSOL file
%[intu]=postint(fem,'abs(u9^2)','solnum',sol,'dl',[2 3 4 5 6 8 9]);
[intu]=postint(fem,'abs(u9^2)','solnum',sol);
disp('  (1 of 1)');
t1=toc;
disp('-------------------------');
disp('Normalisation and calculations  ... ');
J=zeros(size(lambda,1),1);
I=zeros(size(lambda,1),1);
Overlap=zeros(size(lambda,1),1);
Mx=zeros(size(lambda,1),1);
My=zeros(size(lambda,1),1);
Mz=zeros(size(lambda,1),1);
Mji=zeros(size(lambda,1),1);
Eji=zeros(size(lambda,1),1);
```

```
[ux1,uy1,uz1]=postinterp(fem,'u9x','u9y','u9z',grid1,'solnum',GS);
[u1]=postinterp(fem,'u9',grid1,'solnum',sol);
nu1=zeros(size(u1));nux1=zeros(size(ux1));nuy1=zeros(size(uy1));nuz1=z
eros(size(uz1));
nux1(1,:)=ux1(1,:)./sqrt(intu(1));
nuy1(1,:)=uy1(1,:)./sqrt(intu(1));
nuz1(1,:)=uz1(1,:)./sqrt(intu(1));
for i=1:1:size(u1,1)
    nu1(i,:)=u1(i,:)./sqrt(intu(i));
end
clear u1 ux1 uy1 uz1 grid1;
i=1;     % initial state
%for i=1:1:1
    for j=1:1:size(lambda,1)     % final state
        Overlap(j,i)=sum(conj(nu1(j,:)').*(nu1(GS,:)')*dx*dy*dz);
        Mx(j,i)=sum(1e-10*(conj(nu1(j,:)').*(nux1(i,:)')*dx*dy*dz));
        My(j,i)=sum(1e-10*(conj(nu1(j,:)').*(nuy1(i,:)')*dx*dy*dz));
        Mz(j,i)=sum(1e-10*(conj(nu1(j,:)').*(nuz1(i,:)')*dx*dy*dz));
        Eji(j,i)=(lambda(j,2)-lambda(GS,2));
        J(j,i)=j;I(j,i)=i;
        Mji(j,i)=Mx(j,i)+My(j,i)+Mz(j,i);
    end
%end
checkn1=(sum(conj(nu1').*(nu1')*dx*dy*dz))';
clear nu1 nux1 nuy1 nuz1 ;
disp('  (1 of 8)');

[ux2,uy2,uz2]=postinterp(fem,'u9x','u9y','u9z',grid2,'solnum',GS);
[u2]=postinterp(fem,'u9',grid2,'solnum',sol);
nu2=zeros(size(u2));nux2=zeros(size(ux2));nuy2=zeros(size(uy2));nuz2=z
eros(size(uz2));
nux2(1,:)=ux2(1,:)./sqrt(intu(1));
nuy2(1,:)=uy2(1,:)./sqrt(intu(1));
nuz2(1,:)=uz2(1,:)./sqrt(intu(1));
for i=1:1:size(u2,1)
    nu2(i,:)=u2(i,:)./sqrt(intu(i));
end
clear u2 ux2 uy2 uz2 grid2;
i=1;     % initial state
%for i=1:1:1
    for j=1:1:size(lambda,1)     % final state

Overlap(j,i)=Overlap(j,i)+sum(conj(nu2(j,:)').*(nu2(GS,:)')*dx*dy*dz);

Mx(j,i)=Mx(j,i)+sum(1e-10*(conj(nu2(j,:)').*(nux2(i,:)')*dx*dy*dz));

My(j,i)=My(j,i)+sum(1e-10*(conj(nu2(j,:)').*(nuy2(i,:)')*dx*dy*dz));

Mz(j,i)=Mz(j,i)+sum(1e-10*(conj(nu2(j,:)').*(nuz2(i,:)')*dx*dy*dz));
        Eji(j,i)=(lambda(j,2)-lambda(GS,2));
        J(j,i)=j;I(j,i)=i;
        Mji(j,i)=Mji(j,i)+Mx(j,i)+My(j,i)+Mz(j,i);
    end
%end
checkn2=(sum(conj(nu2').*(nu2')*dx*dy*dz))';
clear nu2 nux2 nuy2 nuz2 ;
disp('  (2 of 8)');

[ux3,uy3,uz3]=postinterp(fem,'u9x','u9y','u9z',grid3,'solnum',GS);
[u3]=postinterp(fem,'u9',grid3,'solnum',sol);
nu3=zeros(size(u3));nux3=zeros(size(ux3));nuy3=zeros(size(uy3));nuz3=z
eros(size(uz3));
```

```
nux3(1,:)=ux3(1,:)./sqrt(intu(1));
nuy3(1,:)=uy3(1,:)./sqrt(intu(1));
nuz3(1,:)=uz3(1,:)./sqrt(intu(1));
for i=1:1:size(u3,1)
    nu3(i,:)=u3(i,:)./sqrt(intu(i));
end
clear u3 ux3 uy3 uz3 grid3;
i=1;     % initial state
%for i=1:1:1
    for j=1:1:size(lambda,1)     % final state

Overlap(j,i)=Overlap(j,i)+sum(conj(nu3(j,:)').*(nu3(GS,:)')*dx*dy*dz);

Mx(j,i)=Mx(j,i)+sum(1e-10*(conj(nu3(j,:)').*(nux3(i,:)')*dx*dy*dz));

My(j,i)=My(j,i)+sum(1e-10*(conj(nu3(j,:)').*(nuy3(i,:)')*dx*dy*dz));

Mz(j,i)=Mz(j,i)+sum(1e-10*(conj(nu3(j,:)').*(nuz3(i,:)')*dx*dy*dz));
        Eji(j,i)=(lambda(j,2)-lambda(GS,2));
        J(j,i)=j;I(j,i)=i;
        Mji(j,i)=Mji(j,i)+Mx(j,i)+My(j,i)+Mz(j,i);
    end
%end
checkn3=(sum(conj(nu3').*(nu3')*dx*dy*dz))';
clear nu3 nux3 nuy3 nuz3 ;
disp('  (3 of 8)');

[ux4,uy4,uz4]=postinterp(fem,'u9x','u9y','u9z',grid4,'solnum',GS);
[u4]=postinterp(fem,'u9',grid4,'solnum',sol);
nu4=zeros(size(u4));nux4=zeros(size(ux4));nuy4=zeros(size(uy4));nuz4=z
eros(size(uz4));
nux4(1,:)=ux4(1,:)./sqrt(intu(1));
nuy4(1,:)=uy4(1,:)./sqrt(intu(1));
nuz4(1,:)=uz4(1,:)./sqrt(intu(1));
for i=1:1:size(u4,1)
    nu4(i,:)=u4(i,:)./sqrt(intu(i));
end
clear u4 ux4 uy4 uz4 grid4;
i=1;     % initial state
%for i=1:1:1
    for j=1:1:size(lambda,1)     % final state

Overlap(j,i)=Overlap(j,i)+sum(conj(nu4(j,:)').*(nu4(GS,:)')*dx*dy*dz);

Mx(j,i)=Mx(j,i)+sum(1e-10*(conj(nu4(j,:)').*(nux4(i,:)')*dx*dy*dz));

My(j,i)=My(j,i)+sum(1e-10*(conj(nu4(j,:)').*(nuy4(i,:)')*dx*dy*dz));

Mz(j,i)=Mz(j,i)+sum(1e-10*(conj(nu4(j,:)').*(nuz4(i,:)')*dx*dy*dz));
        Eji(j,i)=(lambda(j,2)-lambda(GS,2));
        J(j,i)=j;I(j,i)=i;
        Mji(j,i)=Mji(j,i)+Mx(j,i)+My(j,i)+Mz(j,i);
    end
%end
checkn4=(sum(conj(nu4').*(nu4')*dx*dy*dz))';
clear nu4 nux4 nuy4 nuz4 ;
disp('  (4 of 8)');

[ux5,uy5,uz5]=postinterp(fem,'u9x','u9y','u9z',grid5,'solnum',GS);
[u5]=postinterp(fem,'u9',grid5,'solnum',sol);
nu5=zeros(size(u5));nux5=zeros(size(ux5));nuy5=zeros(size(uy5));nuz5=z
eros(size(uz5));
nux5(1,:)=ux5(1,:)./sqrt(intu(1));
```

```
nuy5(1,:)=uy5(1,:)./sqrt(intu(1));
nuz5(1,:)=uz5(1,:)./sqrt(intu(1));
for i=1:1:size(u5,1)
    nu5(i,:)=u5(i,:)./sqrt(intu(i));
end
clear u5 ux5 uy5 uz5 grid5;
i=1;    % initial state
%for i=1:1:1
    for j=1:1:size(lambda,1)    % final state

Overlap(j,i)=Overlap(j,i)+sum(conj(nu5(j,:)').*(nu5(GS,:)')*dx*dy*dz);

Mx(j,i)=Mx(j,i)+sum(1e-10*(conj(nu5(j,:)').*(nux5(i,:)')*dx*dy*dz));

My(j,i)=My(j,i)+sum(1e-10*(conj(nu5(j,:)').*(nuy5(i,:)')*dx*dy*dz));

Mz(j,i)=Mz(j,i)+sum(1e-10*(conj(nu5(j,:)').*(nuz5(i,:)')*dx*dy*dz));
        Eji(j,i)=(lambda(j,2)-lambda(GS,2));
        J(j,i)=j;I(j,i)=i;
        Mji(j,i)=Mji(j,i)+Mx(j,i)+My(j,i)+Mz(j,i);
    end
%end
checkn5=(sum(conj(nu5').*(nu5')*dx*dy*dz))';
clear nu5 nux5 nuy5 nuz5 ;
disp('  (5 of 8)');

[ux6,uy6,uz6]=postinterp(fem,'u9x','u9y','u9z',grid6,'solnum',GS);
[u6]=postinterp(fem,'u9',grid6,'solnum',sol);
nu6=zeros(size(u6));nux6=zeros(size(ux6));nuy6=zeros(size(uy6));nuz6=z
eros(size(uz6));
nux6(1,:)=ux6(1,:)./sqrt(intu(1));
nuy6(1,:)=uy6(1,:)./sqrt(intu(1));
nuz6(1,:)=uz6(1,:)./sqrt(intu(1));
for i=1:1:size(u6,1)
    nu6(i,:)=u6(i,:)./sqrt(intu(i));
end
clear u6 ux6 uy6 uz6 grid6;
i=1;    % initial state
%for i=1:1:1
    for j=1:1:size(lambda,1)    % final state

Overlap(j,i)=Overlap(j,i)+sum(conj(nu6(j,:)').*(nu6(GS,:)')*dx*dy*dz);

Mx(j,i)=Mx(j,i)+sum(1e-10*(conj(nu6(j,:)').*(nux6(i,:)')*dx*dy*dz));

My(j,i)=My(j,i)+sum(1e-10*(conj(nu6(j,:)').*(nuy6(i,:)')*dx*dy*dz));

Mz(j,i)=Mz(j,i)+sum(1e-10*(conj(nu6(j,:)').*(nuz6(i,:)')*dx*dy*dz));
        Eji(j,i)=(lambda(j,2)-lambda(GS,2));
        J(j,i)=j;I(j,i)=i;
        Mji(j,i)=Mji(j,i)+Mx(j,i)+My(j,i)+Mz(j,i);
    end
%end
checkn6=(sum(conj(nu6').*(nu6')*dx*dy*dz))';
clear nu6 nux6 nuy6 nuz6 ;
disp('  (6 of 8)');

[ux7,uy7,uz7]=postinterp(fem,'u9x','u9y','u9z',grid7,'solnum',GS);
[u7]=postinterp(fem,'u9',grid7,'solnum',sol);
nu7=zeros(size(u7));nux7=zeros(size(ux7));nuy7=zeros(size(uy7));nuz7=z
eros(size(uz7));
nux7(1,:)=ux7(1,:)./sqrt(intu(1));
nuy7(1,:)=uy7(1,:)./sqrt(intu(1));
```

```
nuz7(1,:)=uz7(1,:)./sqrt(intu(1));
for i=1:1:size(u7,1)
    nu7(i,:)=u7(i,:)./sqrt(intu(i));
end
clear u7 ux7 uy7 uz7 grid7;
i=1;    % initial state
%for i=1:1:1
    for j=1:1:size(lambda,1)    % final state

Overlap(j,i)=Overlap(j,i)+sum(conj(nu7(j,:)').*(nu7(GS,:)')*dx*dy*dz);

Mx(j,i)=Mx(j,i)+sum(1e-10*(conj(nu7(j,:)').*(nux7(i,:)')*dx*dy*dz));

My(j,i)=My(j,i)+sum(1e-10*(conj(nu7(j,:)').*(nuy7(i,:)')*dx*dy*dz));

Mz(j,i)=Mz(j,i)+sum(1e-10*(conj(nu7(j,:)').*(nuz7(i,:)')*dx*dy*dz));
        Eji(j,i)=(lambda(j,2)-lambda(GS,2));
        J(j,i)=j;I(j,i)=i;
        Mji(j,i)=Mji(j,i)+Mx(j,i)+My(j,i)+Mz(j,i);
    end
%end
checkn7=(sum(conj(nu7').*(nu7')*dx*dy*dz))';
clear nu7 nux7 nuy7 nuz7 ;
disp('  (7 of 8)');

[ux8,uy8,uz8]=postinterp(fem,'u9x','u9y','u9z',grid8,'solnum',GS);
[u8]=postinterp(fem,'u9',grid8,'solnum',sol);
nu8=zeros(size(u8));nux8=zeros(size(ux8));nuy8=zeros(size(uy8));nuz8=z
eros(size(uz8));
nux8(1,:)=ux8(1,:)./sqrt(intu(1));
nuy8(1,:)=uy8(1,:)./sqrt(intu(1));
nuz8(1,:)=uz8(1,:)./sqrt(intu(1));
for i=1:1:size(u8,1)
    nu8(i,:)=u8(i,:)./sqrt(intu(i));
end
clear u8 ux8 uy8 uz8 grid8 intu;
i=1;    % initial state
%for i=1:1:1
    for j=1:1:size(lambda,1)    % final state

Overlap(j,i)=Overlap(j,i)+sum(conj(nu8(j,:)').*(nu8(GS,:)')*dx*dy*dz);

Mx(j,i)=Mx(j,i)+sum(1e-10*(conj(nu8(j,:)').*(nux8(i,:)')*dx*dy*dz));

My(j,i)=My(j,i)+sum(1e-10*(conj(nu8(j,:)').*(nuy8(i,:)')*dx*dy*dz));

Mz(j,i)=Mz(j,i)+sum(1e-10*(conj(nu8(j,:)').*(nuz8(i,:)')*dx*dy*dz));
        Eji(j,i)=(lambda(j,2)-lambda(GS,2));
        J(j,i)=j;I(j,i)=i;
        Mji(j,i)=Mji(j,i)+Mx(j,i)+My(j,i)+Mz(j,i);
    end
%end
checkn8=(sum(conj(nu8').*(nu8')*dx*dy*dz))';
clear nu8 nux8 nuy8 nuz8 ;
disp('  (8 of 8)');

disp('--------------------------');
disp('Checking approximation accuracy ...');
checkn=checkn1+checkn2+checkn3+checkn4+checkn5+checkn6+checkn7+checkn8
-1;
disp('Error for GS =');disp(checkn(GS));
if abs(checkn(1))>0.001
    disp('>> Warning: Possible high error in calculation!');
```

```
end
disp('  (1 of 1)');
clear checkn1 checkn2 checkn3 checkn4 checkn5 checkn6 checkn7 checkn8;

%disp('Number of solutions =');disp(size(lambda,1));
%disp('Max array size =');disp(size(nu1,1)*size(nu1,2));
%disp('Total data extracted
=');disp(size(nu1,1)*size(nu1,2)*7*4+size(nu8,1)*size(nu8,2)+size(lamb
da,1));
t2=toc-t1;

disp('==============================================');
disp('(b)  SPECTRA SIMULATION');
disp('==============================================');
% plot absorption spectra
xx=(0.001:0.001:0.5)';
n=size(xx,1);
disp('Broadening width (meV) =');
disp(g/1e-3);
absorpx=zeros(size(xx));absorpy=zeros(size(xx));absorpz=zeros(size(xx)
);
if q==1
    % Gaussian broadening
    disp('Applying Gaussian broadening ...');
    for i=2:1:size(Eji,1)-1
        for j=1:1:n
            si=(g/2)./(sqrt(2*log(2)));

absorpx(j)=absorpx(j)+abs((Mx(i,1))^2)*exp(-((xx(j)-Eji(i,1))^2)/(2*(s
i^2)));%/(sqrt(2*pi)*si);

absorpy(j)=absorpy(j)+abs((My(i,1))^2)*exp(-((xx(j)-Eji(i,1))^2)/(2*(s
i^2)));%/(sqrt(2*pi)*si);

absorpz(j)=absorpz(j)+abs((Mz(i,1))^2)*exp(-((xx(j)-Eji(i,1))^2)/(2*(s
i^2)));%/(sqrt(2*pi)*si);
        end
    end
elseif q==2
    %Lorenzian broadening
    disp('Applying Gaussian broadening ...');
    for i=1:1:size(Eji,1)
        for j=1:1:n

absorpx(j)=absorpx(j)+abs((Mx(i,1))^2)*((g/2)^2/((xx(j)-Eji(i,1))^2+(g
/2)^2))/pi;

absorpy(j)=absorpy(j)+abs((My(i,1))^2)*((g/2)^2/((xx(j)-Eji(i,1))^2+(g
/2)^2))/pi;

absorpz(j)=absorpz(j)+abs((Mz(i,1))^2)*((g/2)^2/((xx(j)-Eji(i,1))^2+(g
/2)^2))/pi;
        end
    end
end

yy=zeros(n,1);
wavex=zeros(n,1);
wavey=zeros(n,1);
wavez=zeros(n,1);
for i=1:1:n
    yy(i)=1.241/xx(n+1-i);
    wavex(i)=absorpx(n+1-i);
```

```
    wavey(i)=absorpy(n+1-i);
    wavez(i)=absorpz(n+1-i);
end

if p==1
    figure;
    subplot(1,3,1);
    plot(yy,wavex);
    grid;xlabel('Wavelength (um)');
    subplot(1,3,2);
    plot(yy,wavey);
    grid;xlabel('Wavelength (um)');
    subplot(1,3,3);
    plot(yy,wavez);
    grid;xlabel('Wavelength (um)');
end

disp('
--------------------------------------------------------------------');
%-------------------------------------------------------');
disp('    Energy    Overlap     Eji        Mx ');%Mjix      Mjiy
Mjiz');%      Fjix      Fjiy      Fjiz      Fji');
disp('
--------------------------------------------------------------------');
%-------------------------------------------------------');
disp(real([lambda(:,2) Overlap Eji Mx]));
% Fx Fy Fz Fji]);
%disp('Sum of Oscillator Strength (x y z Fj1)='); disp([sum(Fx(:,1))
sum(Fy(:,1)) sum(Fz(:,1)) sum(Fji(:,1))]);
clear hb sol;

toc;t3=toc-t2;
```

References

1 A. Y. Cho, *J. Vac. Sci. Technol.* **8**, 31 (1971)

2 A. Y. Cho, *Appl. Phys. Lett.* **19**, 467 (1971)

3 H. M. Manasevit, *Appl. Phys. Lett.* **12**, 156 (1968)

4 R. D. Dupuis and P. D. Dapkus, *Appl. Phys. Lett.* **31**, 466 (1977)

5 C. Kittel, Introduction to Solid State Physics 8th Edition (John Wiley & Sons, 2005)

6 D. Bimberg, M. Grundmann, and N. N. Ledentsov, *Quantum Dot Heterostructures* (John Wiley & Sons, 2001)

7 Z. I. Alferov, *Rev. Mod. Phys.* **73**, 767 (2001)

8 W. Lei and C. Jagadish, *J. Appl. Phys.* **104**, 091101 (2008)

9 Z. Y. Yin and X. H. Tang, *Solid-state Electronics* **51**, 6 (2007)

10 M. C. Payne, M. P. Teter, D. C. Allan, T. A. Arias and J. D. Joannopoulos, *Rev. Mod. Phys*. **64**, 1045 (1992)

11 C. Jacoboni, The Monte Carlo Method for Semiconductor Device Simulation (Wien: Springer-Verlag, 1989)

12 M. J. Kelly, *Low-Dimensional Semiconductors* (Oxford University Press, 1995)

13 P. Y. Yu and M. Cardona, *Fundamentals of Semiconductors 3rd Edition* (Springer Berlin Heidelberg New York, 2005)

14 R. Enderlein and N. J. M. Horing, *Fundamentals of Semiconductor Physics and Devices* (World Scientific Publishing, 1997)

15 L. -W. Wang, S. –H. Wei, T. Mattila, A. Zunger, I. Vurgaftman, and J. R. Meyer, *Phys. Rev. B* **60**, 5590 (1999)

16 M. A. Naser, M. J. Deen and D. A. Thompson, *J. Appl. Phys.* **102** 083108 (2007)

17 V. Putz, C. Ede and A. Scrinzi, *Phys. Rev. B* **76** 035318 (2007)

18 G. H. Yeap, S. I. Rybchenko, I. E. Itskevich and S. K. Haywood, *Phys. Rev. B* **79** 075305 (2009)

19 S. Fafard, Z. R. Wasilewski, C. Ni' Allen, D. Picard, P. G. Piva, and J. P. McCaffrey, *Superlattices Microstruct*. **25**, 87 (1999)

20 Data in Science and Technology: Semiconductors Group IV Elements and III-V Compounds, edited by O. Madelung (Springer-Verlag, 1991)

21 E. L. Ivchenko and G. E. Pikus, Superlattices and Other Heterostructures: Symmetry and Optical Phenomena 2nd Edition (Springer-Verlag Berlin Heidelberg, 1997)

22 L. Esaki, *IEEE J. Quantum Electron*. **22**, 1611 (1986)

23 S. Schulz and G. Czycholl, *Phys. Rev. B* **72**, 165317 (2005)

24 O. Stier, M. Grundmann, and D. Bimberg, *Phys. Rev. B* **59**, 5688 (1999)

25 M. Grundmann, O. Stier, and D. Bimberg, *Phys. Rev. B* **52**, 11969 (1995)M. Moreno, A. Trampert, B. Jenichen, L. Daweritz, and K. H. Ploog, *J. Appl. Phys*. **92**, 4672 (2002)

26 A. Lenz, R. Timm, H. Eisele, Ch. Hennig, S. K. Becker, R. L. Sellin, U. W. Pohl, D. Bimberg, and M. Dahne, *Appl. Phys. Lett*. **81**, 5150 (2002)

27 Y. Arakawa, H. Sakaki, *Appl. Phys. Lett.* **40** 939 (1982)

28 M. Asada, Y. Miyamoto, Y. Suematsu, *IEEE J. Quantum Electron.* **QE-22** 1915 (1986)

29 D. Leonard, M. Krishnamurthy, C. M. Reaves, S. P. DenBaars, and P. M. Petroff, *Appl. Phys. Lett*. **63**, 3203 (1993)

30 A. Madhukar, Q. Xie, P. Chen, and A. Konkar, *Appl. Phys. Lett*. **64**, 2727 (1994)

31 J. M. Moison, F. Houzay, F. Barthe, L. Leprince, E. Andre, and O. Vatel, *Appl. Phys. Lett.* **64**, 196 (1994)

32 D. Bimberg, M. Grundmann, F. Heinrichsdorff, N. N. Ledentsov, V. M. Ustinov, A. E. Zhukov, A. R. Kovsh, M. V. Maximov, Y. M. Shernyakov, B. V. Volovik, A. F. Tsatsul’nikov, P. S. Kop’ev, Zh. I. Alferov, *Thin Solid Films* **367**, 235 (2000)

33 M. Henini and M. Bugajski, *Microelectronics Journal* **36**, 950 (2005)

34 X. Huang, et al., *Electron. Lett.* **36**, 41 (2001)

35 N. N. Ledentsov, V. M. Ustinov, A. Y. Egorov, et al., *Semiconductors* **28**, 832 (1994)

36 V. Ryzhii, *Semicond. Sci. Technol*. **11** 759 (1996)

37 E. Finkman, S. Maimon, V. Immer, G. Bahir, S. E. Schacham, F. Fossard, F. H. Julien, J. Brault and M. Gendry, *Phys. Rev. B* **63**, 045323 (2001)

38 L. Jiang, S. S. Li, N. T. Yeh, J. I. Chyi, C. E. Ross, and S. K. Jones, *Appl. Phys. Lett*. **85**, 1986 (2003)

39 E. Varley, M. Lenz. S. J. Lee, J. S. Brown, D. A. Ramirez, A. Stintz, and S. Krishna, *Appl. Phys. Lett*. **91**, 081120 (2007)

40 A. Imamog¯lu, D. D. Awschalom, G. Burkard, D. P. Divincenzo, D. Loss, M. Sherwin, and A. Small, *Phys. Rev. Lett*. 83, 4204 (1999)

41 R. Nötzel, *Semicond. Sci. Technol*. **11**, 1365 (1996)

42 L. H. Pfeiffer, L. Störmer, K. W. Baldwin, K. W. West, A. R. Goñi, A. Pinczuk, et al., *J. Cryst. Growth* **127**, 839 (1993)

43 R. Nötzel and K. H. Ploog, *Adv. Mater*. **5**, 22 (1993)

44 X. Q. Shen, M. Tanaka, and T. Nishinaga, *J. Cryst. Growth* **127**, 932 (1993)

45 T. Fukui, H. Saito, M. Kasu, and S. Ando, *J. Cryst. Growth* **124**, 493 (1992)

46 C. Weisbuch and B. Vinter, *Quantum Semiconductor Structures* (San Diego: Academic Press, 1991)

47 Z. Yin and X. Tang, *Solid-state Electronics* **51**, 6 (2007)

48 S. I. Rybchenko et al., *Appl. Phys. Lett.* **87**, 033104 (2005)

49 G. C. Dente and M. L. Tilton, *Phys. Rev. B* **66**, 165307 (2002)

50 A. J. Williamson and A. Zunger, *Phys. Rev. B* **64**, 1978 (2000)

51 R. Magri and A. Zunger, *Phys. Rev. B* **68**, 155329 (2003)

52 J. C. Slater and G. F. Koster, *Phys. Rev*. **94**, 1498 (1954)

53 D. L. Smith and C. Mailhiot, *Rev. Mod. Phys*. **62**, 173 (1990)

54 E. O. Kane, *J. Phys. Chem. Solids* **1**, 249 (1957)

55 T. B. Bahder, *Phys. Rev. B* **41**, 11992 (1990)

56 T. B. Bahder, *Phys. Rev. B* **45**, 1629 (1992)

57 C. M. Goringe, D. R. Bowler, and E. Hernández, *Rep. Prog. Phys*. **60**, 1447 (1997)

58 T. B. Boykin, G. Klimeck, R. C. Bowen, F. Oyafuso, *Phys. Rev. B* **66**, 125207 (2002)

59 C. Pryor, *Phys. Rev. B* **57**, 7190 (1998)

60 G. Bastard, Wave mechanics applied to semiconductor heterostructures (John-Wiley & Sons, 1991)

61 K. F. Brennan, The Physics of Semiconductors with applications to optoelectronic devices (Cambridge University Press, 1999)

62 A. J. Williamson, L. W. Wang, and A. Zunger, *Phys. Rev. B* **62**, 12963 (2000)

63 O. L. Lazarenkova, P. von Allmen, F. Oyafuso, S. Lee, and G. Klimeck, *Appl. Phys. Lett*. **85**, 4193 (2004)

64 M. A. Migliorato, A. G. Cullis, M. Fearn, and J. H. Jefferson, *Phys. Rev. B* **65**, 115316 (2002)

65 J. Tersoff, *Phys. Rev. B* **39**, 5566 (1989)

66 A. d. Andreev, J. R. Downes, D. A. Faux, E. P. O'Reilly, *J. Appl. Phys*. **86**, 297 (1997)

67 A. E. Romanow, G. E. Beltz, W. T. Fischer, P. M. Petroff, and J. S. Speck, *J. Appl. Phys*. **89**, 4523 (2001)

68 A. Schliwa, M. Winkelnkemper, and D. Bimberg, *Phys. Rev. B* **76**, 205324 (2007)

69 C. Pryor, J. Kim, L. W. Wang, A. J. Williamson, and A. Zunger, *J. Appl. Phys.* **83**, 2548 (1998)

70 F. Boxberg and J. Tulkki, *Rep. Prog. Phys*. **70**, 1425 (2007)

71 J. Doyle, Modern Experimental Stress Analysis: Completing the Solution of Partially Specified Problems (John Wiley & Sons, 2004)

72 I. Vurgaftman, J. R. Meyer, and L. R. Ram-Mohan, *J. Appl. Phys.* **89**, 5815 (2001)

73 Semiconductors: Intrinsic Properties of Group IV Elements and III-V, II-VI and I-VII Compounds, edited by O. Madelung, Landolt-Bornstein, New Series, Group III, Vol. 22 (Springer, Berlin, 1987)

74 C. G. Van de Walle, *Phys. Rev. B* **39**, 1871 (1989)

75 S. -H. Wei and A. Zunger, *Phys. Rev. B* **49**, 14337 (1994)

76 G. Bester and A. Zunger, *Phys. Rev. B* **71**, 045318 (2005)

77 L. A. Coldren and S. W. Corzine, *Diode Lasers and Photonic Integrated Circuits* (John Wiley & Sons, 1995)

78 J. M. Luttinger and W. Kohn, *Phys. Rev*. **97**, 869 (1955)

79 J. M. Luttinger, *Phys. Rev*. **102**, 1030 (1956)

80 M. J. Fagan, Finite Element Analysis: Theory and Practice (Longman, 1992)

81 R. J. Astley, Finite Element in Solids and Structures: An Introduction (Chapman & Hall, 1992)

82 R. D. Cook, Finite Element Modeling for Stress Analysis (John Wiley & Sons, 1995)

83 H. T. Johnson, L. B. Freund, C. D. Akyüz, and A. Zaslavsky, *J. Appl. Phys*. **84**, 3714 (1998)

84 Y. Wang, J. Wang, and H. Guo, *Phys. Rev. B* **49**, 1928 (1994)

85 T. Inoshita and H Sakaki, *J. Appl. Phys*. **79**, 269 (1996)

86 W. Lee, J. M. Myoung, Y. H. Yoo, and H. Shin, *Solid State Comm*. **132**, 135 (2004)

87 Q. X. Pei, S. S. Quek, J. Y. Guo, and C. Lu, *Engineering Analysis with Boundary Elements* **32**, 309 (2008)

88 B. C. Smith, Fundamentals of Fourier Transform Infrared Spectroscopy (Bota Raton, Fla. : CRC Press, 1996)

89 C. H. Grein, P. M. Young, M. E. Flatté, and H. Ehrenreich, *J. Appl. Phys*. **78**, 7143 (1995)

90 H. J. Haugan, G. J. Brown, F. Szmulowicz, L. Grazulis, W. C. Mitchel, S. Elhamri, and W. D. Mitchell, *J. Cryst. Growth* **278**, 198 (2005)

91 J. B. Rodriguez, P. Christol, F. Chevrier, and A. Joullié, *Physica E* **28**, 128 (2005)

92 N. Deguffroy, V. Tasco, A. Gassenq, L. Cerutti, A. Trampert, A. N. Baranov, and E. Tournié, *Electron. Lett*. **43**, 1285 (2007)

93 D. M. Wood and A. Zunger, *Phys. Rev. B* **53**, 7949 (1996)

94 R. Magri and A. Zunger, *Physica E* **13**, 325 (2002); *Phys. Rev. B* **64**, 081305(R) (2001); ibid. **65**, 165302 (2002)

95 F. Szmulowicz, H. Haugan, and G. J. Brown, *Phys. Rev. B* **69**, 155321 (2004); B. A. Foreman, *Phys. Rev. Lett.* **81**, 425 (1998)

96 M. E. Twigg, B. R. Bennett, P. M. Thibado, B. V. Shanabrook, and L. J. Whitman, *Philos. Mag. A* **7**, 7 (1998)

97 K. Mahalingam, K. G. Eyink, G. J. Brown, D. L. Dorsey, C. F. Kisielowski, and A. Thust, *Appl. Phys. Lett.* **88**, 091904 (2006)

98 J. Steinshnider, J. Harper, M. Weimer, C. –H. Lin, S. S. Pei, and D. H. Chow, *Phys. Rev. Lett.* **85**, 4562 (2000)

99 S. I. Rybchenko, G. H. Yeap, R. Gupta, I. E. Itskevich, and S. K. Haywood, *J. Appl. Phys.* **102** 013706 (2007)

100 G. Bastard, E. E. Mendez, L. L. Chang, and L. Esaki, *Phys. Rev. B* **26**, 1974 (1982)

101 H. J. Haugan, F. Szmulowicz, G. J. Brown, B. Ullrich, S. R. Munshi, L. Grazulis, K. Mahalingam, and S. T. Fenstermaker, *Physica E* **32**, 289 (2006)

102 P. Ongstad, R. Kaspi, C. E. Moeller, M. L. Tilton, D. M. Gianardi, J. R. Chavez, and G. C. Dente, *J. Appl. Phys.* **89**, 2185 (2001)

103 M. Fox, Optical Properties of Solid 2nd Edition (Oxford University Press, 2010)

104 N. Vukmirović, Z. Ikonić, I. Savić, D. Indjin and P. Harrison, *J. Appl. Phys.* **100**, 074502 (2006)

105 H. Lim, W. Zhang, S. Tsao, T. Sills, J. Szafraniec, K. Mi, B. Movaghar and M. Razeghi, *Phys. Rev. B* **72** 085332 (2005)

106 S. Krishna, *J. Phys. D: Appl. Phys.* **38** 2142 (2005)

107 S. Kret, T. Benabbas, C. Delamarre, Y. Androussi, A. Dubon, J. Y. Laval, and A. Lefebvre, J. Appl. Phys. **86**, 1988 (1999)

108 A. Rosenauer, W. Oberst, D. Litvinov, and D. Gerthsen, Phys. Rev. B **61**, 8276 (2000)

109 P. B. Joyce, T. J. Krzyzewski, G. R. Bell, B. A. Joyce, and T. S. Jones, Phys. Rev. B **58**, R15981 (1998)

110 D. M. Bruls, J. W. A. M. Vugs, P. M. Koenraad, H. W. M. Salemink, J. H. Wolter, M. Hopkinson, M. S. Skolnick, Fei Long, and S. P. A. Gill, Appl. Phys. Lett. **81**, 1708 (2002)

111 A. V. Barve, T. Rotter, Y. Sharma, S. J. Lee, S. K. Noh, and S. Krishna, Appl. Phys. Lett. **97**, 061105 (2010)

112 M. Y, Petrov, I. V. Ignatiev, S. V. Poltavtsev, A. Greilich, A. Bauschulte, D. R. Yakovlev, and M. Bayer, *Phys. Rev. B* **78** 045315 (2008)

113 C. H. Tan, P. Vines, M. Hobbs, B. Anderson, M. Hugues, and J. David, Infrared Phys. and Tech. **54**, 228 (2011)

114 P. Offermans, P. M. Koenraad, R. Nötzel, J. H. Wolter, and K. Pierz, Appl. Phys. Lett. **87**, 111903 (2005)

115 M. Hugues, M. Teisseire, J. –M. Chauveau, B. Vinter, B. Damilano, J. –Y. Duboz, and J. Massies, Phys. Rev. B **76**, 075335 (2007)

116 S. Gaan, G. He, R. M. Feenstra, J. Walker, and E. Towe, J. Appl. Phys. **108**, 114315 (2010)

117 D. Zhi, H. Davock, R. Murray, C. Roberts, T. S. Jones, D. W. Pashley, P. J. Goodhew, and B. A. Joyce, J. Appl. Phys. **89**, 2079 (2001)

118 R. V. Shenoi, R. S. Attaluri, A. Siroya, J. Shao, Y. D. Sharma, A. Stintz, T. E. Vandervelde and S. Krishna, *J. Vac. Sci. Technol. B* **26** 1136 (2008)

119 W. Sheng and J. P. Leburton, *Phys. Rev. B* **64**, 153302 (2001)

120 Z. R. Wasilewski, S. Fafard, and J. P. McCaffrey, *J. Cryst. Growth* **201/202** 1131 (1999)

121 X. Z. Liao, J. Zou, X. F. Duan, D. J. H. Cockayne, R. Leon, and C. Lobo, *Phys. Rev. B* **58**, R4235 (1998)

122 S. Fafard, Z. R. Wasilewski, C. Ni' Allen, D. Picard, M. Spanner, J. P. McCaffrey, and P. G. Piva, *Phys. Rev. B* **59**, 15368 (1999)

123 S. Fafard, Z. R. Wasilewski, C. Ni' Allen, K. Hinzer, J. P. McCaffrey, and Y. Feng, *Appl. Phys. Lett*. **75**, 986 (1999)

124 J. P. McCaffrey, M. D. Robertson, S. Fafard, Z. R. Wasilewski, E. M. Griswold, and L. D. Madson, *J. Appl. Phys.* **88**, 2272 (2000)

125 A. S. Bracker, M. Scheibner, M. F. Doty, E. A. Stinaff, I. V. Ponomarev. J. C. Kim, L. J. Whitman, T. L. Reinecke, and D. Gammon, *Appl. Phys. Lett.* **89**, 233110 (2006)

126 G. Bester, X. Wu, D. Vanderbilt, and A. Zunger, *Phys. Rev. Lett* **96**, 187602 (2006)

List of Publications

B. H. Hong, S. I. Rybchenko, I. E. Itskevich, S. K. Haywood, R. Intartaglia, V. Tasco, G. Rainò, and M. De Giorgi, *Applicability of the* $k \cdot p$ *method to modelling of InAs/GaSb short-period superlattices*, Physical Review B **79**, 165323 (2009)

B. H. Hong, S. I. Rybchenko, I. E. Itskevich, S. K. Haywood, C. H. Tan, P. Vines, and M. Hugues, *Modelling of intraband absorption for quantum dot-in-well structures with low computational cost*, Journal of Physics: Conference Series **242**, 012013 (2010)

B. H. Hong, S. I. Rybchenko, I. E. Itskevich, S. K. Haywood, C. H. Tan, P. Vines, and M. Hugues, *Intraband absorption in quantum dot-in-well mid-infrared photodetectors: modeling with low computational cost*, submitted to Journal of Applied Physics.

B. H. Hong, L. Tinkler, S. I. Rybchenko, I. E. Itskevich, S. K. Haywood, and M. Hugues, *Structural parameters of quantum dots grown by In-flush techniques determined by optical spectroscopy and modelling*, to be submitted to peer-review journal.